A method for evaluating the role of gold nanoparticles in monochromatic x-ray studies

Dissertation
zur
Erlangung des Doktorgrades (Dr. rer. nat.)
der
Mathematisch-Naturwissenschaftlichen Fakultät
der
Rheinischen Friedrich-Wilhelms-Universität Bonn

vorgelegt von
Martin Franz Niestroj
aus
Oppeln

Bonn, 2016

Angefertigt mit Genehmigung der Mathematisch-Naturwissenschaftlichen Fakultät der Rheinischen Friedrich-Wilhelms-Universität Bonn.

Dieser Forschungsbericht wurde als Dissertation von der Mathematisch-Naturwissenschaftlichen Fakultät der Universität Bonn angenommen und ist auf dem Hochschulschriftenserver der ULB Bonn http://hss.ulb.uni-bonn.de/diss_online/ elektronisch publiziert.

1. Gutachter:	Prof. Dr. Josef Hormes
2. Gutachter:	Prof. Dr. Stefan Linden
Tag der Promotion:	09.05.2017
Erscheinungsjahr:	2017

Abstract

To promote the use of gold nanoparticles as an enhancement agent from a principle concept into therapeutic applications, it is imperative to obtain detailed knowledge of the nanoparticle-induced radiobiological mechanisms. Synchrotrons are the preferred x-ray source when conducting systematic investigations regarding the role of gold nanoparticles in radiation therapy. The primary objective motivating this dissertation was to circumvent existing limitations at the interface between synchrotron science and cell biology. The phenomenon that inspired this goal is the observation that gold nanoparticles mediate the behavior of cells maintained under deviated environmental culture conditions. To accomplish this cross-disciplinary achievement, each part of the experiment process is critically reviewed and reassessed. The viability assessment based on the conversion of the tetrazolium salt MTT (3-(4,5-dimethylthiazol-2)-2,5-diphenyltetrazolium bromide) is modified to quantify the number of viable cells in the irradiation vessel. The established concept for horizontal irradiations enables the treatment of the living cells maintained under optimal cell line-specific culture conditions at synchrotron beamlines. The introduced sample transportation strategy completes the procedure, which is finally characterized by a minimized number of experimental parameters. By allowing living cells to proliferate uninterrupted and undisturbed throughout the experiment, the established method generates reliable and meaningful results that reflect the true cellular response to monochromatic keV x-rays. The presented gold nanoparticle study illustrates that the otherwise mediating nanoparticles do not enhance the radiotherapeutic effectiveness of monochromatic 20.0 keV x-rays. The implication is that the presented method is capable of elevating the acceptance and credibility of all subsequent synchrotron-based studies on living cells. Ideas for future research include the development of live-cell imaging applications at synchrotron beamlines.

Summary

Gold nanoparticles are promising adjuvants for improving the effectiveness of ionizing radiation on living tissue. Synchrotron light facilities – with their unique capacity to generate intense, monochromatic and tunable x-ray beams – fulfil the experimental qualifications to investigate the role of the nanosized protagonists in radiation therapy. However, research projects at the interface of synchrotron science and cell biology are confronted with compromising irradiation conditions and questionable experimental procedures. Before this work introduces a new framework for the treatment of living cells with monochromatic keV x-rays at synchrotron beamlines, the synchrotron-based *in vitro* irradiation experiment is divided into consecutive experimental parts. For each part, the most common approaches as well as their strengths and weaknesses are evaluated in relation to the experimental conditions for cell cultures. If identified as problematic, the questionable part is either modified or completely redesigned to meet to the upmost standards.

This work proposes a novel approach for synchrotron-based cell culture irradiation based on the use of a bent silicon wafer in Laue geometry as a monochromatizing device. Implemented at the bending magnet beamline BMIT-BM, the constructed irradiation system enables horizontal irradiations of standard culture dishes with purely monochromatic x-rays from about 10 keV to 30 keV. In addition, the high intensity of the monochromatic x-ray beam allows to deliver large dose levels of up to 10 Gy within tolerated exposure times. Living cells maintained in common culture vessels can be taken from the laboratory incubator, exposed to x-rays through a horizontal scanning process, and returned to the incubator without disturbing and interrupting the cellular growth. In allowing the cells to continuously proliferate under optimal conditions, the genuine approach circumvents the limitations of previous *in vitro* irradiations at synchrotron beamlines. The horizontal set-up even opens up a pathway for promising bright-field, phase-contrast, or even fluorescence imaging applications at synchrotron beamlines. Combined live-cell imaging and rapid functional assessments could create novel opportunities to study radiation-induced events at synchrotron beamlines.

Deviating culture conditions before and after the irradiation process can be the origin of cellular stress factors which then significantly alternate the cellular behavior. A portable incubator provides the required cell type-specific culture conditions for the sample transportation and storage outside the cell laboratory. By generating a culture environment identical to the environment available in the laboratory incubator, the portable device closes an important gap which is generally neglected in the literature. The universal transportation strategy is not limited to the use of culture dishes but embraces the use of flasks and tubes as culture vessel as well.

To validate the applied experimental procedure and to assess the cellular response to therapeutic radiation, the conversion of the yellow MTT salt into formazan crystals by viable cells is preferred to the time-consuming and work-intensive colony formation as analytical method. The standard MTT protocol is modified to quantify the amount of formazan solubilized in the irradiation vessel. The direct dish read-out produced data sets with an accuracy and precision that is hardly achieved by the standard method. The linear relationship between the initial cell number and the measured absorbance over a broad cell number range offers many options for key parameters such as the initial number of seeded cells or the duration of the post-irradiation proliferation. The developed measurement process makes otherwise necessary cell transfers obsolete and is not restricted to the use of culture dishes. As shown, toxicological assessments generally benefit from an increased level of quality for the collected data sets. In contrast to clonogenic assessments, the rapid analytical method generates meaningful irradiation results after

only three MCF-7 doubling times. The measured 11.9 keV dose-response curve can be phenomenologically described by a first order exponential decay indicating that the cellular damage induced by 11.9 keV x-rays is comparable to the lethal effects caused by high linear energy transfer (LET) particles. Despite the appearance of critical experimental inconveniences, the 20.0 keV dose-response curve reconfirms the general observations made at 11.9 keV.

The established experimental protocol – characterized by horizontal sample irradiations, a sample transportation strategy, and a direct sample read-out process – guarantees the uninterrupted and undisturbed proliferation of cells under their cell type-specific culture conditions throughout the entire experiment from the sample preparation to the final assessment. Putting all pieces together, the presented irradiation procedure is defined by a minimized set of highly controllable experimental parameters with the ionizing radiation being the only cellular stressor. By successfully circumventing the limitations at the interface of synchrotron science and cell biology, the irradiation procedure avoids the production of misleading irradiation results and the successive generation of false conclusions.

In the final chapter of this dissertation, the role of gold nanoparticles is evaluated at the peak photon attenuation coefficient ratio of gold and soft tissue (20.0 keV). The prepared gold nanoparticles with an average diameter of about 11.6 nm were functionalized with thio-glucose. According to mass spectroscopy measurements, the concentration of nanoparticles in the available colloid solution was comparable to the concentrations applied in previously conducted enhancement studies. Transmission electron microscopy provided valuable information about the intracellular distribution of the nanoparticles at the time of the treatment. As successfully illustrated, MCF-7 cells internalize glucose-capped nanoparticles via an endocytic pathway. The nanoparticles are mainly internalized within cytoplasmic vesicles where they frequently assemble in form of clusters. The toxicological study confirmed the predicted nanoparticle biocompatibility for the MCF-7 cell line. Despite their biological inert character, internalized gold nanoparticles affect the cellular behavior tremendously. The cellular response to deviating cell culture conditions (i.e. standard laboratory conditions) is significantly mediated. The final *in vitro* study reveals that the internalized gold nanoparticles do not enhance the radiotherapeutic effectiveness of 20.0 keV x-rays. The observed lack of enhancement at the anchor point for the x-ray energy is in direct conflict with the encouraging results documented in the existing scientific literature. These circumstances raise questions about the appropriateness of the methods applied in the recently conducted studies. The new perspective on the role of gold nanoparticles, including the nanoparticle-mediated cellular response to deviating culture environments, hopefully helps tp strengthen the awareness of cellular integrity as a key parameter in irradiation studies. Studies that do not sufficiently care for the biological cells have a high chance of suffering from misleading results and false conclusions about the role of gold nanoparticles *in vitro*.

Table of Contents

1. Introduction

The discovery of x-rays by W.C. Röntgen in 1895 marks the beginning of a cancer treatment modality taking advantage of ionizing radiation to create damaging effects in soft tissue. In the last decade, the rise of nanotechnology has opened up new pathways to improve the effectiveness of radiation therapy. Because of their versatility and highly biocompatible character, gold nanoparticles are one of the most promising adjuvants in this growing research area. In the last years, several reviews have been published discussing the role of gold nanoparticles as radiotherapeutic enhancement agents *in vivo* and *in vitro* (Jain et al. 2012; Dorsey et al. 2013; Jeremic et al. 2013; Ngwa et al. 2014). The increased attenuation of keV x-rays in gold compared to soft tissue is accompanied by the emission of secondary radiation leading to the deposition of additional energy in the direct vicinity of the internalized agents. However, increasing the local dose as a fundamental principle has been questioned by several publications that reported positive outcomes for therapeutic modalities using MeV photons, protons, or electrons as the primary ionizing element. The underlying mechanisms responsible for the increased radiotherapeutic effectives by gold nanoparticles remain vague at best, thus a comprehensive and systematic approach seems imperative to develop the necessary knowledge for promoting this technology into clinical applications.

The principles of radiobiology are based on the concept that the living cell is the fundamental biological unit for all living organisms. Living cells can be used as primary irradiation targets to investigate early radiation-induced physical effects and the following avalanche of chemical, bio-chemical, and biological events. While radiobiological studies on human cells have been conducted since the establishment of the HeLa cell line, profoundly systematic *in vitro* irradiation studies could not be initiated before the appearance of third generation synchrotron facilities and the development of sophisticated instrumentation technology. Today, synchrotron beamlines are capable of generating intense photon beams with monochromatic energies that cover the innermost electron shells of heavy elements (e.g. gold K-shell: 80.7 keV, gold L_3-shell: 11.9 keV) and physical features such as the peak attenuation coefficient ratio of gold and soft tissue (at 20.0 keV). For this reason, synchrotron facilities are the most valuable x-ray sources to evaluate any potential nanoparticle-induced effects in radiation therapy.

Despite their unique capacity to generate intense and tunable x-ray beams, cell biologists are hampered from undertaking meaningful radiobiological research at synchrotron beamlines. To avoid unwanted or artefactual consequences ranging from aberrant cell phenotypes to a complete failure of the cell culture, it is of paramount importance to strictly obey the guiding principles for cell culturing throughout irradiation experiments. The most frequently applied strategy for the treatment of living cells with monochromatic keV x-rays is constructed on the experimental conditions that synchrotron beams traverses along the horizontal direction. For the irradiation process, adherent cells are maintained in dishes or flasks filled to capacity with culture medium, even though it is generally known that deviated culture conditions such as different culture media volumes can influence cellular behavior. The vessels are aligned perpendicular to the incident x-ray beam with the targeted cells attached to the bottom of the irradiation vessel. During exposure, the tilted cells are then moved vertically while facing the monochromatic x-ray beam. The same scanning procedure is applied for cell suspensions in tubes or capillaries. These x-ray treatments are consequently accompanied not only by compromising culture conditions during the irradiation processes, but also by potentially perturbing experimental procedures consisting of numerous protocol steps. From the sample preparation until the final analysis, each step inevitably adds more parameters to an already large number of variables that must be controlled throughout the

course of the experiment. Depending on the experience and care of the researcher, some of these parameters can be easily overlooked or even falsely disregarded with consequences on the reliability of the conducted study. Every undefined or neglected parameter may be directly related to a cellular stress factor that can induce alternative cellular behaviors. To avoid any unreliability, methodically accurate synchrotron-based irradiation procedures must provide cell culture conditions as close as possible to the conditions present in the laboratory incubator and aim to reduce the number of experimental parameters to an absolute minimum. Minimizing the number of experimental parameters increases the chance that all variables are well identified and properly controlled throughout the study. Results obtained under these sample-oriented conditions reflect the true cellular response to the treatment with monochromatic x-rays. Once established, thoroughly-conducted synchrotron-based *in vitro* studies can be awarded with an overly high acceptance because misinterpretations of the recorded irradiation data sets and false conclusions about studies' outcomes are omitted to the greatest extent.

Every irradiation procedure can be broadly divided into three parts. The first part includes the maintenance of the cell stock, the preparation of the cell populations, and the internalization of the potential enhancement agents. The middle part discusses the exposure of the targeted tissue to the therapeutic radiation. The last part covers the post-irradiation treatment, which consists of a pre-defined post-irradiation proliferation phase and the final assessment. Colony forming assays have yielded novel insights into the radiobiological effectiveness of different treatment modalities on a variety of cancerous and non-cancerous cells. The so-called "gold standard" in radiation therapy has been applied to obtain information about variances in radiation sensitivity and lethal or sub-lethal damage repair processes; however, this method can only be applied to cell samples capable of forming countable colonies. Analytical methods based on the cellular reduction of tetrazolium salt MTT (3-(4,5-dimethylthiazol-2)-2,5-diphenyltetrazolium bromide) into soluble formazan produce highly objective results comparable to the results gained by clonogenic assays (Chapter 3). Once the specific parameter ranges for a given cell line are established, meaningful irradiation data sets can be obtained in less time and with less effort. In this dissertation, a modified protocol for the quantification of formazan directly solubilized in the irradiation vessel is described. The direct read-out not only produces highly accurate and precise assessment results, but also eases the sample handling at the end of the irradiation procedure considerably.

The irradiation of living cells maintained in standard culture dishes is the most important step to circumvent the existing limitations at the interface between synchrotron science and cell biology. However, a different approach for the irradiation of living cells is required to overcome the obstacles of vertical scans. By using a single bent silicon wafer in Laue geometry as a monochromatizing element, it is possible to design a set-up for horizontal sample irradiations under optimal cell line-specific conditions. The design, calibration and operation of the irradiation system, implemented at the BioMedical Imaging and Therapy bending magnet beamline BMIT-BM, is described in full detail in Chapter 4. At the end of the chapter, the suitability of the irradiation system is demonstrated by the first dose-response curve for the breast cancer cell line MCF-7 at a photon energy of 11.9 keV. This accomplishment allows beamline users to develop non-perturbing irradiation procedures with minimal experimental parameters.

A sophisticated experimental procedure is then applied to evaluate the role of gold nanoparticles on the cell line MCF-7 at 20.0 keV (Chapter 5). Transmission electron microscopy visualizes the intracellular distribution of the functionalized gold nanoparticles at the point of irradiation. Toxicological assessments and further preliminary tests yield important information about the influence of gold nanoparticles on cellular behavior under selected environmental culture conditions. As demonstrated, the otherwise biocompatible nanoparticles mediate the cellular response to deviating culture conditions with devastating consequences to the meaningfulness of

the established irradiation results. To avoid these pitfalls, an elaborate sample transportation and storage strategy must be implemented. After joining all experimental parts together, the final assessments reveal that gold nanoparticles do not enhance the radiotherapeutic effectiveness of monochromatic 20.0 keV x-rays for the breast cancer cell line MCF-7. The implications of these apparently conflicting results on the currently active research field are briefly discussed.

2. Motivation

Cancer is a class of diseases characterized by an uncontrolled growth of genetically modified cells within a patient's body. The deregulated spread of cancerous cells harms the otherwise healthy body when tumors perturb normal physiological functions such as in the digestive, nervous, or circulatory systems. In developed countries, heart disease has been the leading cause of death, with cancer the second-most leading cause. In 2012, about 220,000 patients died due to cancer-related causes in Germany and about 480,000 new cancer cases were expected to be diagnosed (Kaatsch et al. 2015). Besides the personal burden for the individual patients (about 51% of men and 43% of woman in Germany develop cancer at one point over their lifespan), the disease is one of the largest burdens in the healthcare system due to costs for prevention, diagnosis, treatment, recovery, and palliative medical care. Because the risk of being diagnosed with cancer rises with age, aging populations are expected to face increasing social, medical, and financial stress levels. In Germany, the number of new annual cancer cases is expected to increase by a factor of 20% from 2010 to 2030 (Kaatsch et al. 2015).

Cancer is a complex disease associated with a high level of heterogeneity on the molecular and cellular levels. The development and progression of cancer is a multi-step process during which cells undergo substantial metabolic and behavioral changes. The origin of cancer is directly related to mutations in the deoxyribonucleic acid (DNA) sequence. To develop into cancerous tissue, normal cells must acquire genetic changes that lead to the promotion of abnormal cell proliferation (activation of "oncogenes") or the suppression of proliferation when needed, though it is possible that both options to be present. Genetically modified cells start to form clones capable of escaping the surveillance of the body's own immune system. The tolerated clones continue to proliferate and, during this process, may accumulate more dysfunctional genes and altered cellular modifications. Because of these continuously ongoing changes, cancer is best described as a progressive disease. When undetected at an early stage, progressing cancer cells are likely to interfere with neighboring healthy tissue and may even create supporting blood vessels ("angiogenesis"). Cancer can spread ("metastasize") and disseminate even to remote organs.

Successful therapies inhibit tumor growth or even eradicate cancerous tissue from a patient who might benefit from increased quality of life, prolonged survival, and potentially a complete cure. Disseminated cancers are difficult to treat and generally require a systematic drug-based approach, such as chemotherapy. Chemotherapy involves a single cytotoxic drug or a mixture of cytotoxic substances being given to the patient to promote cancerous cell death and inhibit cancer proliferation and spread. Most patients receive combined treatments such as chemotherapy and surgery, surgery and hormone therapy, or chemotherapy and radiation therapy. Surgery can be useful for the treatment of precancerous lesions, while more radical strategies remove entire organs affected by cancerous cells or tissue that has an elevated risk of developing cancer. Surgery is often the first step to properly diagnose the type of cancer and which stage it has reached. Another essential modality of cancer treatment that cannot be effectively replaced by chemotherapy or surgery is radiation therapy. Since the detection of x-rays, radiation therapy has been developing as an essential clinical modality against local tumors. In the last decades, radiotherapeutic applications have seen tremendous technological advances (e.g. imaging-guided radiotherapy, radiosurgery). Nowadays, more than 50% of all patients who develop cancer are treated with radiation at some time during their illness (Delaney et al. 2005). Although it is one of the least expensive cancer treatments per patient, radiation therapy is highly effective in terms of a patient's cure and overall survival (Van De Werf et al. 2012). Radical high-dose radiation is a sole

treatment, whereas moderate radiation can be used as an adjunct to surgery for early-stage tumors. Palliative radiation therapy, which is offered to patients suffering from advanced-stage cancer, is intended to reduce symptoms and to improve the patients' quality of life. The optimal radiation therapy utilization rate depends on the type of cancer and varies from a low rate of 0% for liver cancer, 60% for prostate cancer, 83% for breast cancer, and the highest rate of 92% for patients with central nervous system tumors (Delaney et al. 2005).

2.1. Radiation Therapy

At the juncture of physics and biology, radiation therapy is the clinical modality that takes advantage of ionizing radiation to generate electrically charged particles in soft tissue. The primary aim of radiotherapeutic applications is to deposit large amounts of radiation energy into the targeted tumor volume. The transferred energy initiates inundations of chemical, bio-chemical, and biological events which lead to sub-lethal or lethal effects within the irradiated tissue. The most common form of radiation therapy is external beam radiation, in which external sources generate the therapeutic radiation that is directed from outside the patient's body into the cancerous tissue.

External radiation can be categorized into photon, electron, and hadron radiation. Hadron therapy includes radiotherapeutic applications with particles consisting of quarks such as protons, neutron, or heavy ions. Charged heavy particle beams continuously transfer energy while traversing the targeted tissue. The deposited dose slightly increases as penetration depth increases up to the "Bragg peak," which occurs close to the end of the particle's range (Tanner et al. 1967). Because of the favorable dose profile, charged particle beams deposit most of their energy over a narrow range while the surrounding tissue receives very little of the radiation dose. The higher dose conformity results in less irradiation of normal tissue.

Electrons, with their short range in soft tissue, are often applied in intraoperative radiation therapy (Gieschen et al. 2001) or to treat skin cancer. However, the most common form of external radiation therapy uses photon radiation in form of x-rays and γ-rays. High-energy photon beams are commonly generated by x-ray tubes, at linear accelerators, or by radioactive isotopes such as cesium-137 or cobalt-60. The interaction processes of photons with matter via photoelectric absorption, Rayleigh scattering, Compton scattering, and pair production is extensively described in the existing literature (see for example Krane 1988). For photon energies in the keV region, the dose profile of a traversing photon beam is similar to the exponentially decaying intensity with penetration length. At higher energies, the deposited dose starts to increase with the penetration thickness until it peaks ("skin effect"), followed by a decaying pattern similar to the pattern for lower energies.

The response of living cells to ionizing radiation depends strongly on the cellular physiology and is generally described in the form of radiosensitivity for a given therapeutic modality. While radiosensitive cancer cells are completely eradicated by modest dose levels, some types of cancers notably exhibit a behavior which can be described as radioresistant. Additionally, the localization of the targeted tumor plays a significant role in the success of radiation treatments; glioma – one of the most frequent brain tumors – is still incurable because the radiation-induced damage to the surrounding healthy brain tissue limits the amount of radiation dose that can be delivered to the targeted volume (Biston et al. 2004). Although the majority of cancer cells are moderately radiosensitive, a deposition of large amounts of radiation energy is generally required to achieve clinically acceptable therapeutic outcomes.

The treatment of cancerous tissue with ionizing radiation is accompanied by strong side effects. Early side effects (e.g. skin effects, mucositis, nausea, etc.) become manifest within a few days or weeks after the initial treatment and are often transient. On the other hand, late effects (e.g. fibrosis, atrophy, vascular and neural damage, etc.) are expressed after latent periods of months to years, tend to be irreversible, and, in the worst case, may even progress. For example, long-term survivors of radiation-based treatments exhibit an increased risk for the development of second malignant tumors (Friedman et al. 2010). The radiosensitivity of the surrounding healthy tissue limits the use of ionizing radiation in cancer treatment. The key to improve the therapeutic effectiveness is to increase the relative susceptibility of cancerous tissue to ionizing radiation.

2.2. Radiotherapeutic Enhancement by Gold Nanoparticles

Because of their versatility and biocompatibility, gold nanoparticles represent one of the most promising adjuvant for radiotherapeutic applications. As slight deviations in size, shape, and surface properties can alternate the interactions at the nano-bio interface, the possibilities to tailor any nanoparticle-induced effects seem endless, as demonstrated by the growing number of gold nanoparticle studies in existing scientific literature. Gold nanoparticles in particular appear to be highly compatible in biological systems ranging from a patient's body to a single cell. Due to the existing strong ligand-gold bonding, gold nanoparticles can be functionalized by conjugation to various biological substances (e.g. anti-bodies, peptides, glucose, etc.). The functionalized hybrid materials feature a metallic core surrounded by electrically neutral or charged molecules with the outer layer as fundamentally important to the interaction with the direct environment (Arvizo et al. 2010). The delivery of gold nanoparticles to cancerous tissue can be achieved by the direct targeting of tumor-specific biomarkers or by passive accumulation. The distribution of gold nanoparticles in living systems depends on characteristic nanoparticle properties including the particle's diameter and surface properties (De Jong et al. 2008).

The physical rationale claims that gold nanoparticles internalized into the cancerous tissue increase the local dose, leading to an elevated number of lethal effects during radiation therapy. Therapeutic photons deposit their energy into soft tissue via photoelectric absorption and Compton scattering. Compton scattering is the process whereby a photon interacts with a weakly bound electron in the irradiated material. Part of the photon energy is transferred to the electron which is released from the atom carrying a kinetic energy equal to the difference of the energy lost by the photon and the electron binding energy. The probability for the occurrence of Compton processes depends on the electron density in the irradiated target, which is almost constant for all materials. In contrast, the cross section of the competing photoelectric absorption scales with the atomic number (Z) as roughly Z^{3-4}. Although the cross section decreases steeply with increasing photon energy (approximately as E^{-3} with E being the photon energy), photoelectric absorption remains the most dominant interaction process in gold for photons with energies below 520 keV, according to the NIST Photon Cross Section Database (Hubbell & Seltzer 2009). On the other hand, Compton scattering becomes the most dominant photon interaction process in living tissue at around 30 keV. Figure 2.1 illustrates the difference between the total mass attenuation coefficients of gold and soft tissue. The attenuation coefficient of a given element peaks when the photon energy is equal to the electron binding energy, as shown for the innermost electron shells of gold (Au K-shell at 80.7 keV, Au L-shells between 11.9 and 14.4 keV). The attenuation coefficient ratio of gold and soft tissue peaks at around 20 keV, which is therefore an anchor point in energy-systematic enhancement studies. With Compton scattering as the dominant interaction at much higher photon energies, there is hardly any difference between the absorption coefficient

of heavy elements and soft tissue above 1 MeV. From a physical perspective, therapeutic photons with energies in the MeV region mostly interact via Compton scattering, leaving the internalized gold nanoparticles mostly indistinguishable from the surrounding cancerous tissue in terms of the early photon interaction process.

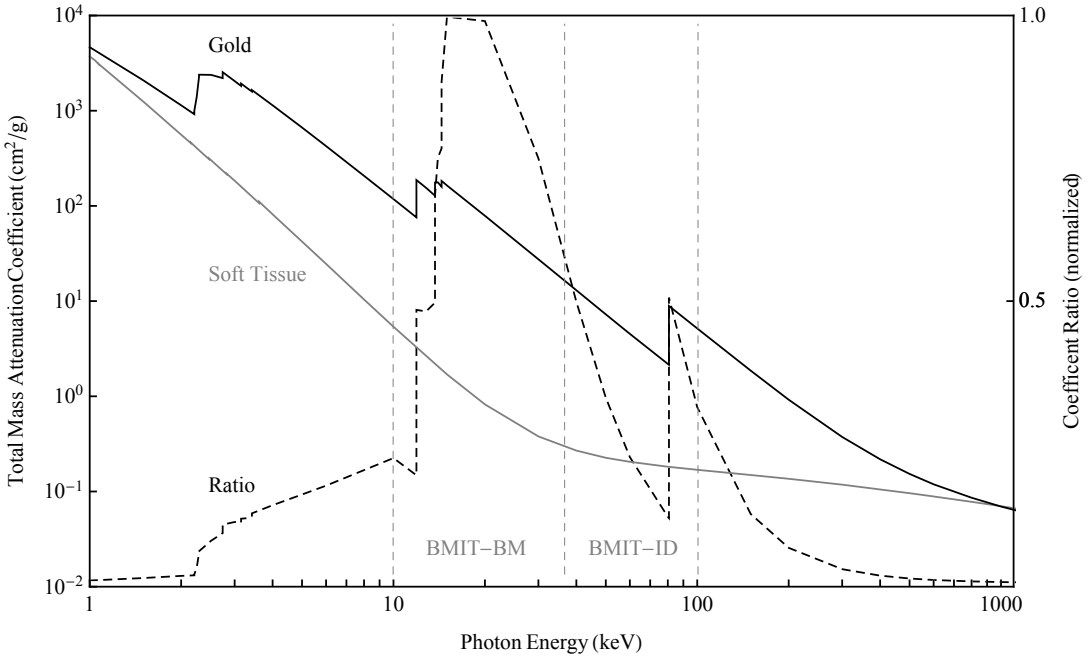

Figure 2.1 Total mass attenuation coefficient of gold (black line) and soft tissue (grey line) for photon energies from 1 keV to 1 MeV. The gold K-edge is seen as a broad peak at 80.7 keV. The gold L-edges appear between 11.9 and 14.4 keV. The coefficient ratio of gold and soft tissue (dashed line) peaks around 20 keV. The photon energy region covered by the sibling beamlines BMIT-BM and BMIT-ID ranges from about 10 to 100 keV (depicted by the dashed vertical lines).

While only part of the photon energy is transferred to the targeted tissue in Compton scattering processes, photons interacting via the photoelectric effect are completely absorbed. The instantaneously liberated photoelectric electron carries a kinetic energy equal to the initial photon energy minus the electron binding energy. Accordingly, the photoelectron range in soft tissue depends on these two variables and can exceed several cell diameters for energies around 100 keV. The following atomic relaxation occurs rapidly through radiative and non-radiative processes. While radiative processes are associated with the emission of keV fluorescence photons, non-radiative processes result in the emission of low keV Auger electrons. Fluorescence photons are capable of travelling long distances in soft tissue (up to a few centimeters) and, as a consequence, may not essentially contribute to additional radiation-induced damage in the targeted volume (Hainfeld et al. 2008). Conversely, low-energy Auger electrons have shorter ranges of typically a few nanometers in soft tissue and thus deposit their entire energy in the direct vicinity of the interacting gold nanoparticle (Howell 2008). According to the physical rationale, the generation of Auger cascades as a direct consequence of the additional photoelectric interaction within the targeted tissue is the underlying mechanism responsible for the enhanced effectiveness of photon therapy by gold nanoparticles.
For the K-shell and L_3-subshell, Auger (and Coster-Kronig) processes are the only non-radiative processes competing with the emission of characteristic x-rays. The probability of a vacancy in

the electron shell being filled by a radiative process is represented by the fluorescence yield. Figure 2.2 illustrates the fluorescence yield for the K-shell and L-shells of the chemical elements for $3 \leq Z \leq 110$. The curve for the L-shells represents the average yield of the L_1-, L_2-, and L_3-subshells (Thompson et al. 2009). The fluorescence yield generally increases as the atomic number increases. Radiative processes are more likely to be generated at electron vacancies in the K-shell while non-radiative processes are more probably for L-shell vacancies. For gold, the fluorescence yield of the K-shell is about 96%, meaning that gold atoms with vacancies in this shell almost exclusively relax via radiative processes. On the other hand, the average fluorescence yield for the Au L-shells is less than 30%, resulting in a high probability for Auger electrons being emitted from the gold atom (Krause 1979). According to these fluorescence yields, therapeutic photons with energies above the gold K-shell are more likely to initiate radiative processes, while photons with energies below the gold K-shell initiate mainly Auger processes.

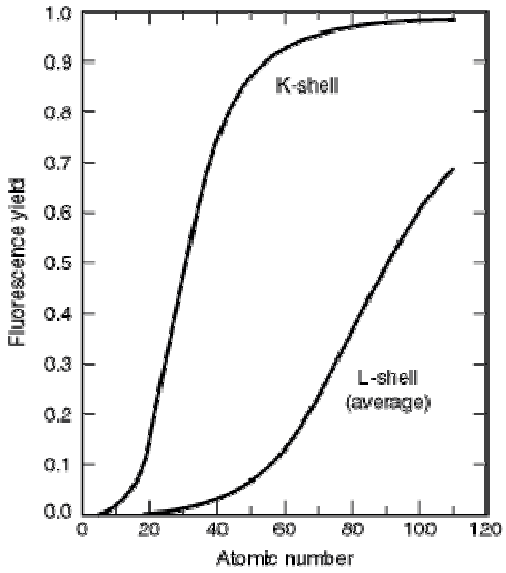

Figure 2.2 Fluorescence yields for K and L shells for $3 \leq Z \leq 110$. The plotted curve for the L shells represents the average effective yields. Reprinted from (Thompson et al. 2009).

Heavy elements such as iodine (Z = 53) or platinum (Z = 78) have been evaluated as potential enhancement agents in monochromatic photon activation therapy. Substances such as 5-Iodo-2′-deoxyuridine ("IUdR") or cis-diamminedichloridoplatinum(II) ("cisplatin") are considered effective Auger electron emitters *in vivo* and *in vitro* (Adam et al. 2003; Biston et al. 2004). In these photon activation studies, the applied photon energy was set just below and above the element-specific K-shell. However, the composition of the emitted secondary radiation and their contribution to the radiation damage in cell cultures appears to be understudied. Radiobiological research was developed around the concept that the living cell is the fundamental biological unit. For this reason, human cell lines – well-characterized representatives of the biological tissue – have been successfully employed as instrumentational tools in radiation studies since G. Gey established the HeLa cell line in the early 1950s (Gey et al. 1952). To maintain the integrity of the cells and to prevent the expression of phenotypes, adherent cells are sub-cultured before they reach a confluence level of 100% (Fig. 2.3). In most irradiation studies, adherent cells are usually arranged in a single monolayer with confluence levels much lower than 100% which means that the cell-to-cell distance exceeds the typical cell diameter. Due to their long range in soft tissue, fluorescence photons emitted from internalized gold nanoparticles are likely to escape from this

cell arrangement without interacting with either the nanoparticle-hosting or any neighboring cells. If the proposed emission of Auger electrons is the primary enhancement mechanism, cell culture studies using photon energies above 80.7 keV might not be able to observe any additional effects induced by gold nanoparticles. In these experiments, low-energy photoelectrons would be the only dominant type of secondary radiation contributing to an increased local dose. Due to the significantly smaller average fluorescence yield of the Au L-shell (less than 30%), any nanoparticle-induced effects based on the generation of Auger electrons are presumably detectable *in vitro* using photon energies below the Au K-shell.

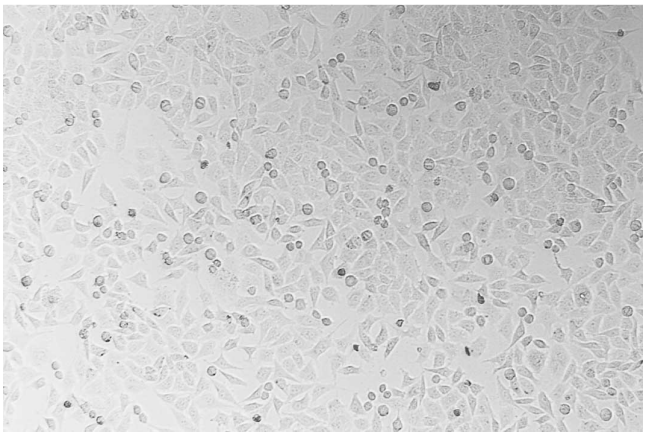

Figure 2.3 Photomicrograph of MCF-7 cells grown to almost 100% confluency.

The proposed physical concept for the enhancement by gold nanoparticles is questioned by several papers reporting improved therapeutic outputs both *in vivo* and *in vitro* for alternated treatment modalities (e.g. MeV photons, electrons, protons). The authors claim that the enhancement mechanisms are dominated by a strong bio-chemical or even biological component, such as sensitization to the redox active compound bleomycin (Jain et al. 2011), the generation of reactive oxygen species by the sole presence of gold nanoparticles (Butterworth et al. 2010; Geng et al. 2011), or cell cycle arrests in the radiosensitive G2/M phase (Roa et al. 2009). It is conceivable that any radiotherapeutic enhancement by gold nanoparticles is a combination of physically-induced and biologically-driven mechanisms.

Photon beams with energies below the Au K-shell are unusable for clinical treatments because of their short penetration length in soft tissue, but fundamental *in vitro* studies on living cells could gain the necessary understanding to tailor the nanoparticle properties for the utmost therapeutic improvements. The capacity to generate monochromatic and tunable x-ray beams with high intensity makes synchrotron light facilities the ideal x-ray source for systematic radiobiological studies. For example, the sibling beamlines BMIT-BM and BMIT-ID (see Chapter 4) generate intense photon beams that can be further monochromatized for systematic studies. The available energy region from less than 10 keV to about 100 keV covers crucial features such as the Au K-edge and the Au L-edges as well as the peak photon attenuation coefficient ratio of gold and soft tissue (Fig. 2.1).

3. Interaction of Ionizing Radiation with Soft Tissue

Direct interactions of radiation with living tissue ionize DNA molecules resulting in base modifications or single and double strand breaks (SSBs and DSBs). Unpaired or misrepaired DSBs, characterized by radiation-induced breaks in the two strands opposite each other or separated by only a few base pairs, are evidently the most severe threat to the cellular survival after irradiation (Willers et al. 2004). In contrast to the ionization of DNA molecules, therapeutic radiation can also interact with molecular constituents in the exposed tissue. Indirect interactions of radiation are associated with the liberation of ionizing particles or molecules which contribute essentially to the generation of lethal effects. Free oxygen-based radicals, such as chemically highly reactive oxygen species (ROS), are defined by their unpaired valence electron. Free radicals are able to diffuse long distances within soft tissue and to interact with sensitive cellular components of vital importance or even cellular DNA (Riley 1994). With water being the main element in biological cells, most of the deposited radiation energy presumably causes excessive production of free radicals. Studies have shown that adding high concentrations of scavengers for the hydroxyl radical (·OH) to the culture medium can reduce the yield of radiation-induced damaging effects *in vitro* (Chapman et al. 1973). Figure 3.1 schematically illustrates the direct and indirect radiation pathways to generate DNA lesions.

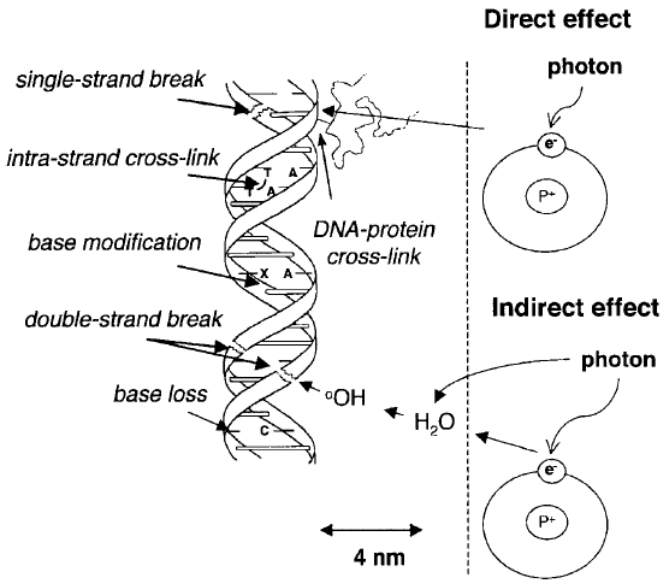

Figure 3.1 Schematic representation of direct and indirect radiation-induced DNA lesions. Reprinted from (Pouget & Mather 2001).

A growing body of evidence indicates that important effects of ionizing radiation may be related to extranuclear events. It has been observed that cytoplasm or membrane irradiation produce genomic instability leading to major genetic alterations (Manti et al. 1997). Cytoplasmic irradiation and the subsequent production of ROS, in particular hydroxyl radicals, seem to play an important role in the generation of genomic mutations (Wu et al. 1999). Because of these effects, cytoplasmic irradiations may be more harmful to cells than nuclear irradiation (Iyer & Lehnert 2000). Membrane degradation after irradiation is presumably the direct result of hydroxyl attacks on polyunsaturated fatty acid residues of phospholipids (Pouget & Mather 2001).

Effects of ionizing radiation may even occur in cells which have not been exposed to irradiation at all. These so-called bystander effects may be communicated by transmissible factors or even by direct cell-to-cell communications (Prise 1998). The response of non-irradiated cells apparently covers a broad spectrum precluding predictive extrapolations from the benign or even detrimental effects.

The exposure to ionizing radiation activates cascades of cellular signaling pathways to promote the genomic integrity and to initiate cellular survival mechanisms. Triggered genes manipulate basic cellular functions such as cell cycle regulation and sometimes even coordinate apoptotic actions. A comprehensive review of the cellular pathways in response to ionizing radiation has been recently published (Maier et al. 2016).

3.1. Assessment of Cellular Response to Ionizing Radiation

Irradiated cells are considered dead once they have lost their ability to divide and produce a large number of progeny. A treated cell which did not undergo reproductive death has retained the capacity to proliferate indefinitely and can produce large groups of cells (colonies). These cells are referred to "clonogenic." Colony forming assessments (also called "clonogenic assays") investigate the ability of singly planted cells to grow into colonies which can be counted after a certain post-irradiation growth phase (Puck & Marcus 1956). Colony formation has yielded information about variances in radiation sensitivity and lethal or sub-lethal damage repair among different cell lines and are considered the method of choice to quantify the survival of cells (Franken et al. 2006). Besides, colony formation can provide novel insights into the effectiveness of different radiotherapeutic treatment modalities (e.g. dose fractionation).

Dose-response curves visualize the loss of reproductive integrity as a function of the delivered radiation dose for a specific treatment modality. These survival curves can be grouped into two types, "linear" or "curved," and are quantitatively described by the linear-quadratic (LQ) model (Barendsen 1982). The LQ-formalism has a mechanistic basis and implies that reproductive death occurs as a consequence of lethal lesions produced by either a single or several independent radiation events. According to the LQ-formalism, the probability of the cells to remain their capacity to proliferate as a function of the absorbed dose D can be described by the survival fraction:

$$SF = S_1(D) \times S_n(D^2) = \exp(-\alpha D) \times \exp(-\beta D^2)$$

The linear component S_1 describes single-event killing (i.e. lethal lesions from a single radiation track) and the quadratic component S_n pronounces multi-event killing (i.e. lethal lesions from two or more radiation tracks). The coefficients α and β depend on several factors (e.g. cell line, treatment modalities, etc.). High linear energy transfer (LET) particles create dense tracks of ionizations and excitations in the targeted volume. Such a single track can effortlessly be responsible for several lethal lesions which are described by the linear component. Logarithmic cell survival curves after irradiation with high-LET particles expectedly follow a straight line (Barendsen 1982). On the other hand, low-LET particles are expected to create lethal DSBs from several individual events rather than one single event. Survival curves for low-LET particle irradiation have a dominant quadratic component.

The LQ-formalism is both experimentally and theoretically validated for single-fractionated dose levels up to 10 Gy (Brenner 2008), so colony formation is respected as the "gold standard" among all *in vitro* techniques for quantifying the cellular response to ionizing radiation. However, several biological factors may influence the described dose-response relationship. For example, variations

in the *in vitro* radiosensitivity by varying cell cycle stages may affect cellular survival. The impact of Bystander effects on the growth of cell colonies remains unclear and requires further investigation.

Despite the obvious advantages of clonogenic assessments, the formation of countable colonies usually takes several weeks, depending on the doubling time of the tested cell line. Manual cell counting requires extensive amounts of experimental time and work, while computer-aided counting by digital image processing algorithms often fail to distinguish between single and merged colonies. For these reasons, time-consuming and work-intensive clonogenic assessments might not be the preferred method for establishing new *in vitro* procedures. Preliminary tests must confirm that the phenotypic integrity remains consistent throughout all experimental steps. None of the applied protocol steps are allowed to alternate cellular functions that might interfere with the cellular response to ionizing irradiation. As the number of required preliminary tests directly relates to the total number of protocols steps, rapid analytical methods that can generate results within days rather than weeks are the preferred choice to verify a proposed procedure.

Today, viability assessments are commonly used in toxicological *in vitro* studies. Although the term “cellular viability” lacks a strict definition, viability assays seek either to quantify the ratio of living cells in a given cell population or to measure the number of living cells in a sample. Viable cells can convert dyes (e.g. Alamar Blue) or salts (e.g. MTS, WST-1, XTT) into products whose total amount can be immediately quantified. Most viability assessments rely on the conversion of the yellow MTT salt 3-(4,5-dimethylthiazol-2-yl)-2,5-diphenyltetrazolium bromide) into a formazan-based purple dye (Fig. 3.2). At room temperature, solubilized formazan is stable for a few hours and can be quantified spectrophotometrically. The workload on the sample, especially at the final stage of the assay, is moderate and does not require extensive amounts of time. In contrast to clonogenic assessments, MTT studies generate results within a few days.

Assessments based on the reduction of MTT have been successfully utilized in radiation studies. The colorimetric method generates reproducible and comparable results to clonogenic assays once optimal conditions for the cell line (i.e. optimal seeding cell number, assessment period) are adapted (Carmichael et al. 1987). The non-clonogenic assay offers a rapid and simple method for the assessment of radiation sensitivity in selected (adherent) cell lines, with the potential for use in the screening of compounds for radiosensitization and protection. Other authors state that surviving fractions obtained by MTT after 250 kVp x-rays irradiations with dose levels of 2 and 4 Gy were in agreement when compared with clonogenic assays (Wasserman & Twentyman 1988). Other studies directly compared colony formation with MTT conversion and confirmed that MTT assays are able to provide reproducible measures of cell survival (Price & McMillan 1990). Both assays yield very similar curve progression and, over the short term, were linear (Buch et al. 2012). The authors finally stated that data generated by the MTT assay presents an opportunity to obtain precise survival data for high sample throughput in less time and with less effort than with the conventional colony assay.

The rapid MTT assessment is therefore the preferred method for the verification of numerous experimental steps in order to establish a proposed irradiation procedure. The employment of the same analytical technique in all preliminary tests and actual irradiation studies generates consistent and comparable data sets. Differences in the cellular viability can be directly related either to potentially perturbing culture conditions, stress-provoking protocol steps, or the actual exposure to ionizing radiation.

Based on the motivation to develop a stress-minimized irradiation procedure, the colorimetric MTT assay was selected as an analytical technique in all preliminary tests and in the first gold nanoparticle enhancement study for monochromatic 20.0 keV X-rays.

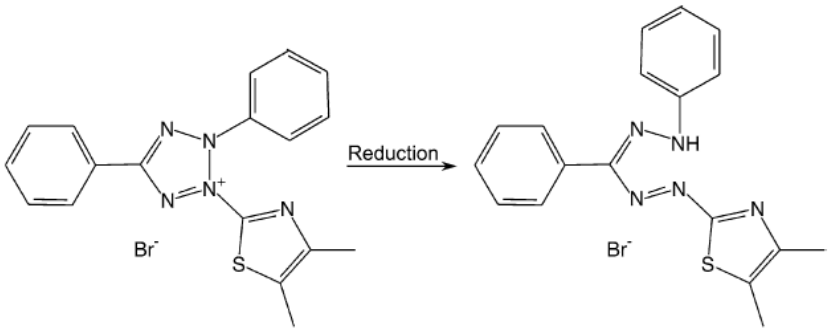

Figure 3.2 Reduction of yellow MTT salt into a purple formazan product. Reprinted from (Kupcsik 2011).

3.2. MTT-based Cellular Viability Assays

In 1983, Mosman described a colorimetric MTT-based assay and its application for cellular growth and survival assessments (Mosmann 1983). Since then, this method has become one of the standard determinants in toxicological assessments due to its capacity to quantify viable cells in growing cell populations.

It has been widely assumed that MTT ($C_{18}H_{16}BrN_5S$) is reduced by mitochondrial succinate dehydrogenase (Slater et al. 1963). However, recent studies revealed that the conversion mechanism primarily takes place in the cytoplasm and, to a lesser extent, in the mitochondria or cell membrane (Berridge & Tan 1993). MTT is taken up by living cells through endocytosis, reduced to needle-like formazan crystals in endosomal or lysosomal compartments, and transported to the cell surface through exocytosis (Liu et al. 2002).

Formazan crystals radiating from the cell membrane can be solubilized in alcohols (e.g. ethanol, isopropanol) or other organic solvents (e.g. isopropanol) to produce a homogeneous purple solution. Dimethyl sulfoxide (DMSO) was found to dissolve formazan very effectively (Jabbar et al. 1989). The total amount of solubilized formazan is subsequently quantified by absorbance measurements. The general UV-Vis spectrum of formazan contains a broad main peak around a photon wavelength of 580 nm (Denizot & Lang 1986). With the spectrophotometrically measured absorbance being proportional to the number of viable cells in the tested population, MTT assessments provide highly accurate and precise results over a wide cell number range. The relationship between the absorbance value and the cell number is linear until effects at the study's end-point such as confluency, nutrient deficiency, increase of waste products, non-sufficient MTT concentrations, or over-extensive MTT exposure times inhibit the reduction of MTT salt into formazan.

Standard MTT assays are performed on cell cultures maintained in 96-well plates with a recommended initial cell concentration of 5,000-10,000 cell/well maintained in 200 µL medium. The homogenously seeded cells are incubated overnight to attach firmly to the bottom substrate. After the treatment that introduces factors or varies culture conditions, the cells proliferate for a pre-defined incubation phase. At the study's end-point, the present culture medium is removed from each well and replaced by 180 µL fresh medium. Then, 20 µL MTT solution is added to each well. The plate is incubated for a period of usually 2-5h during which time the MTT salt is reduced to formazan crystals. The exhausted MTT solution is carefully aspirated and the remaining crystals are dissolved in 200 µL DMSO. The plate is wrapped in aluminum foil, post-incubated for 10 min, and gently swirled for another 10 min using a plate shaker. The absorbance signal A_s (a.u.) can be spectrophotometrically measured at a wavelength of 540-600 nm with the background signal A_c (a.u.) often collected at 690 nm. The background signal is subtracted from

the absorbance signal to obtain the sample's absorbance value. For a tested population, the cellular viability CV rate in percentage can be calculated in accordance with the following equation:

$$CV = A_{Sample} / A_{Control} \times 100$$

Here, A_{Sample} is the absorbance of the tested cell population and $A_{Control}$ is the absorbance of the control group.

The following section presents a modified MTT protocol with optimized assay parameters for viability assessments of cell populations maintained in commonly used culture dishes rather than well plates. After irradiation, cells are usually allowed to proliferate undisturbed for a pre-defined incubation phase. In this growth period, cells actively respond through repair or self-degradation processes that influence the final number of viable cells in the irradiated population. To detect any radiation-induced effects, a sufficiently long post-treatment incubation phase is required during which the cells must not suffer from growth-inhibiting factors such as confluency or nutrient deficiency. To avoid the presence of disturbing conditions, the suitable cell number range and the number of initially seeded cells are important factors that must be defined before applying any modified assessment.

3.2.1. Modified MTT-Assay Protocol

MTT assessments are versatile and remain intact under deliberately modified experimental conditions as long as the assay parameters (e.g. initial cell number, post-treatment incubation phase, MTT concentration) are properly adapted. This section presents a modified MTT protocol with optimized assay parameters for viability assessments of MCF-7 cell populations maintained in commonly used culture dishes. All biology-related parts were conducted at the University of Saskatchewan (UofS) Cell Signalling Laboratory (CSL).

All assessments performed in this study relied on MTT purchased from Calbiochem (#475989). According to the manufacture's instruction, the yellow salt was dissolved in sterile phosphate buffered saline (PBS) at 5 mg/mL, filtered through a 0.22 µm filter, and stored at −20°C. Before its use, the MTT solution was removed from the freezer and pre-warmed to 37°C.

To assess the viability of cell populations growing in 35 mm culture dishes (e.g. Falcon 353001), the present culture medium was replaced by a mixture consisting of 1.8 mL culture medium and 200 µL MTT stock solution. Akin to the standard protocol, the dish was immediately incubated for 3h to allow viable cells to convert the yellow MTT salt into purple formazan crystals. The exhausted mixture was carefully aspirated and the remaining formazan crystals were dissolved using 2 mL DMSO. The dishes were wrapped in aluminum foil, post-incubated for 10 min, and gently swirled for another 10 min. The spectrophotometer (SPECTRAmax® Plus) drawer is designed to hold well plates but not dishes or flasks. As each well marks a distinct reading position, a sample holder made of a 96-well plate not only fit into the drawer, but also provides the necessary information about the scan positions. For this reason, two holes with a diameter of 35 mm had been reamed into the plate so that an inserted dish uniformly covered a matrix of 3×3 wells. A 1 mm thick ledge at the plate bottom was left out to hold the culture dishes in horizontally levelled positions (Fig. 3.3A). For the actual readout procedure, the sample holder was mounted onto the reader's microplate drawer and slid into the reading chamber (Fig. 3.3B). The spectrophotometer measured the absorbance (540 nm) and background (690 nm) signal at each of the nine distinct well positions. The background signals were subtracted from the absorbance signals. The absorbance of the assayed cell population was expressed as the calculated

arithmetic mean of the nine background-subtracted absorbance signals. The resulting cellular viability of the tested sample was calculated in accordance with the standard protocol.

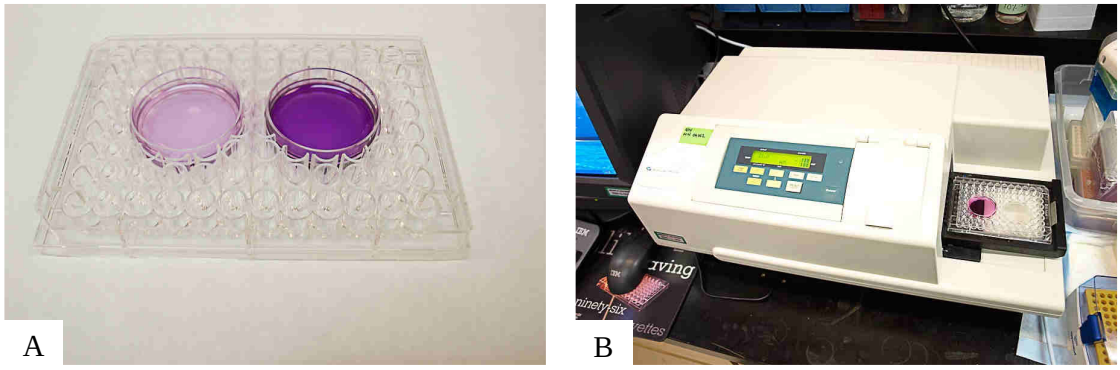

Figure 3.3 Readout procedure for the modified MTT assay protocol: (A) Two culture dishes are positioned in a modified 96-well plate. (B) The sample holder is loaded into the spectrophotometer.

The distribution of the measured absorbance values for culture dishes with an initial MCF-7 cell concentration of either 10,000 or 80,000 cell/dish are shown in Figure 3.4. Both histograms summarize the collected absorbance values of four independently measured culture dishes. The histogram shape has a symmetric and unimodal pattern with a negligible fraction of outliners. In accordance with the Poisson characteristics for the discrete events, the error of each bin was estimated using the square root of the number of counts.

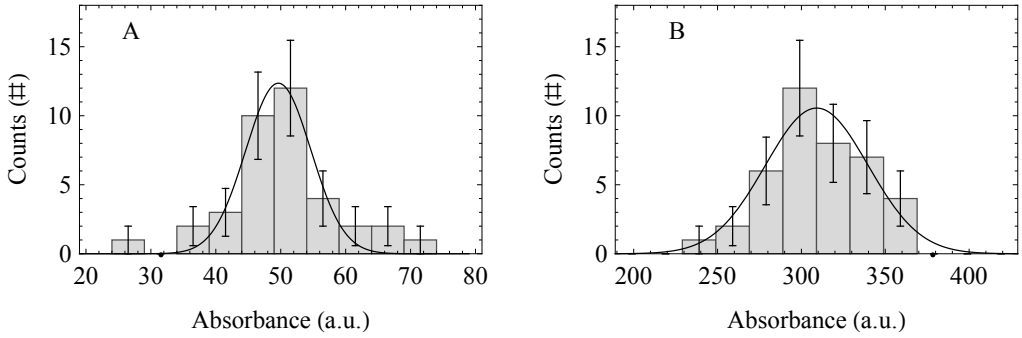

Figure 3.4 Absorbance histograms for an initial cell concentration of either (A) 10,000 or (B) 80,000 cell/dish. The histogram shapes are modelled using Gaussian distributions (solid lines).

The shape of each histogram was approximated by fitting the following probability density function P(x) of the standard Gaussian distribution with mean μ (a.u.), standard deviation σ (a.u.), and amplitude coefficient d (#) to the measured distribution using Mathematica's non-linear fitting algorithm:

$$P(x) = \left(\frac{d}{\sigma\sqrt{2\pi}}\right) \times \exp\left(-\frac{(x-\mu)^2}{(2\sigma)^2}\right)$$

The obtained Gaussian distribution is plotted on top of the associated histogram (Fig. 3.4). Table 3.1 summarizes the fit results including the computed P-values which evaluate the probability that the specific parameter does not contribute to the model that describes the measured distribution. The relative standard error of about 10% for each parameter confirms the appropriateness of the

Gaussian curve to model the related absorbance distribution. Considering the value for the calculated mean absorbance (μ) and the related standard deviation (σ), the relative standard deviation for the modified readout procedure is about 10% for both initial cell numbers. In contrast, the relative standard deviation of standard MTT assessments is seldom smaller than 20% depending upon the number of independent measurements and the quality of the available samples.

Table 3.1 Fit results for the absorbance of four independently measured dishes with initial cell concentrations of either 10,000 cell/dish (index: "10") or 80,000 cell/dish (index: "80").

Parameter	Estimate	Standard Error	P-Value
d_{10}	156	13	6.8×10^{-7}
μ_{10}	49.6	0.5	3.5×10^{-15}
σ_{10}	5.0	0.5	2.4×10^{-6}
d_{80}	811	64	4.7×10^{-7}
μ_{80}	309	3.0	2.0×10^{-15}
σ_{80}	30.7	2.8	1.6×10^{-6}

Once the direct dish readout procedure had been confirmed, the linear relationship between the measured absorbance and the initial number of seeded cells was evaluated. The cellular viability as a function of the cell number was determined for initial MCF-7 cell concentrations from 2,500 cell/dish to 160,000 cell/dish to identify a suitable cell number range. For each concentration, the absorbance is plotted in Figure 3.5A, with each data point representing the mean and standard deviation of the four independent measurements. The relative standard deviation of about 10% over the tested cell number range reconfirms the previous fit results. The conservation of the linear relationship at the upper end of the cell number range supports the hypothesis that the associated cell populations neither reached confluency nor suffered from insufficient nutrients. The applied volume of MTT solution used in the modified protocol was appropriate even for large cell numbers. Otherwise, a shortage of MTT salt inside the culture dish would have created a flattening curve shape with an increasing cell number up to a plateau-like stage.

The measured relationship between the initial cell number and the measured absorbance was subsequently described by a linear progression model with slope a (a.u.) and intercept b (a.u.) using Mathematica's linear fitting algorithm. Table 3.2 summarizes the fit results. The obtained progression line is plotted over the measured curve in Figure 3.5A and can be used as a calibration curve. The fit residuals ($RES = A_{S,observed} - A_{S,expected}$) are plotted together with the standard error of each data point (Fig. 3.5B). The pattern in the residual plot even reflects the applied dilution process at the beginning of the sample preparation. The primary MCF-7 cell stock solution with an initial concentration of 160,000 cell/mL was split in half. In the first dilution step, the first half of the solution was used to prepare a consecutive series of cell solutions with concentrations ranging from 160,000 cell/mL down to 100,000 cell/mL. The second half of the mother solution was used to prepare a consecutive series of MCF-7 samples with cell concentrations from 80,000 cell/mL down to 20,000 cell/mL. The decaying pattern of the residuals displays the dilution steps starting from the upper initial cell number of either 160,000 cells or 80,000 cells down to 100,000 cells and 20,000 cells, respectively. The residuals support

the statement that the dish readout procedure generated highly accurate results with an error significantly smaller than the determined 10%.

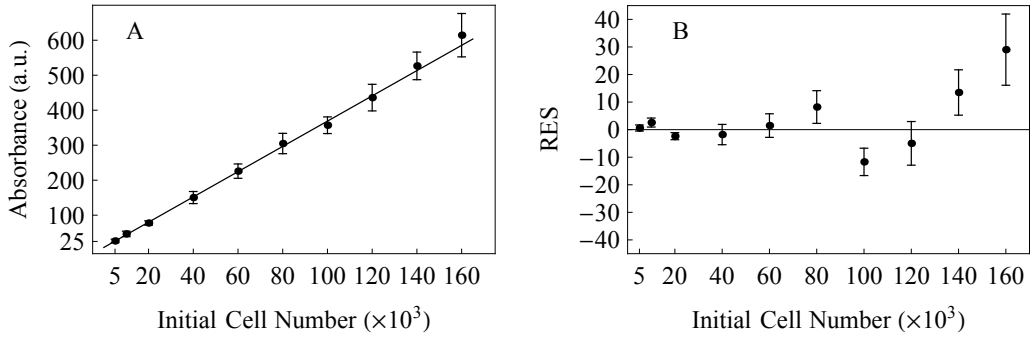

Figure 3.5 Linearity of the modified MTT assay. (A) The calibration curve describes the relationship between the measured absorbance and the initial cell number. (B) Residual plot and standard errors.

Table 3.2 Fit results for the modified MTT assay.

Parameter	Estimate	Standard Error	P-Value
a	3.61	0.05	1.2×10^{-12}
b	7.8	1.4	7.3×10^{-4}

The following second assessment evaluated the conservation of the linear relationship between the absorbance signal and the initial number of seeded cells after a proliferation phase of three MCF-7 doubling times (87h). In contrast to the previous assessment, the prepared MCF-7 cell populations with initial cell numbers ranging from 5,000 cell/dish to 30,000 cell/dish were allowed to proliferate undisturbed for three doubling times. At the study's end-point, the cellular viability was quantified in accordance with the modified MTT protocol.

The measured absorbance values and the obtained regression line are shown in Figure 3.6A, with each data point representing the mean and standard deviation of four independent measurements. Again, the relative standard deviation for each data point is about 10%. The fit results for the linear progression model support the assumption that the relationship between the cellular viability and the initial cell number can be described by a linear curve (Tab. 3.3). This time, the pattern in the residual plot appears random and does not reflect the sample preparation procedure (Fig. 3.6B). However, the homogenous distribution of residuals above and below the regression line confirms the suitability of the linear model to describe the relationship between the absorbance signal and the cell number. The small distances between the residuals and the regression line indicate the high accuracy for the absorbance measurements after a proliferation phase of 87h. The MCF-7 samples with an initial cell concentration of 30,000 cell/dish did not reach confluency within three doubling times. The cells suffered neither from nutrient depletion nor from the accumulation of toxic exhaust products in the culture medium. Overall, the self-reproduction of MCF-7 cells maintained in 35 mm culture dishes was not inhibited for initial cell concentrations up to 30,000 cell/dish over the tested three MCF-7 doubling times.

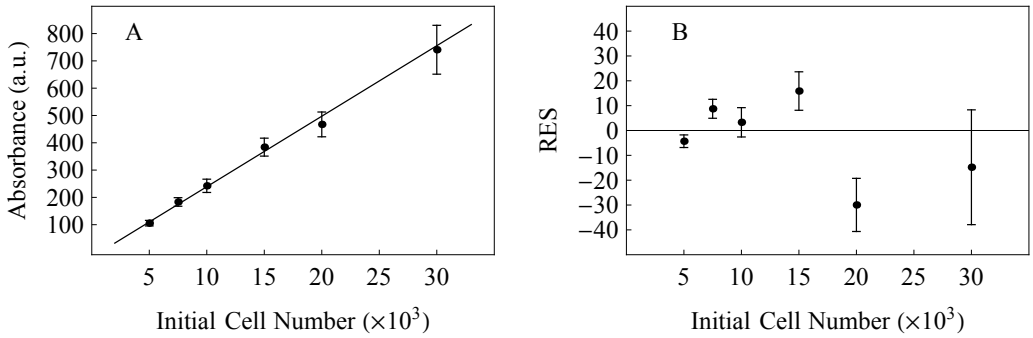

Figure 3.6 Conservation of the assay linearity after three MCF-7 doubling times. (A) The calibration curve describes the relationship between the measured absorbance and the initial cell number. (B) Residual plot and standard errors.

Table 3.3 Fit results for the modified MTT assay after a proliferation phase of 87h (end-point).

Parameter	Estimate	Standard Error	P-Value
a	25.8	1.1	1.9×10^{-5}
b	−19.2	9.1	1.0×10^{-1}

As successfully demonstrated, assessments of cell populations maintained in 35 mm cell culture generates highly accurate and precise viability results. The conservation of linear relationship over three doubling times enables the use of the modified MTT assay as a versatile analytical technique in irradiation experiments. Radiobiological studies using culture dishes as irradiation vessels can benefit from the undisturbed proliferation of MCF-7 samples with initial cell concentrations smaller than or equal to 30,000 cell/dish. Even after a significant post-irradiation period during which the cells may undergo active cell repair or degradation mechanisms, the irradiated cells do not suffer from an inhibited proliferation. In addition, the direct culture dish readout eliminated an otherwise stress-provoking and time-consuming cell transfer from the primary irradiation vessel to a well plate. Possible artefacts in the recorded data are omitted.

From this point, every study presented in this dissertation used the tested 35 mm culture dishes as culture vessels with an initial MCF-7 cell concentration of 10,000 cell/dish. All samples were prepared 24h before the treatment to allow the cells to properly attach to the dish bottom.

4. Treatment of Living Cells with Monochromatic keV X-rays

Synchrotron facilities generate intense photon beams to carry out basic and applied research for a wide range of disciplines. Invented at the National Synchrotron Light Source of Brookhaven National Laboratory, microbeam radiation therapy (MRT) is currently being developed as a form of preclinical radiotherapy (Slatkin et al. 1992). At the European Synchrotron Radiation Facility (ESRF), further steps have been taken towards clinical applications of synchrotron light to treat brain tumors (Smilowitz et al. 2006). In addition to iodinated contrast agents (Corde et al. 2004), the role of potential photonactivation agents containing high-Z elements such as platinum (Biston et al. 2004) or gold (Bobyk et al. 2013) are evaluated in early preclinical studies. However, a parallel approach of technical developments, theoretical and experimental dosimetry, and fundamental biological research on living cells appears imperative to improve current radiotherapeutic modalities and to promote synchrotron-based techniques for established clinical applications.

Compared to photon beams generated by conventional x-ray or γ-ray sources, synchrotrons facilitate the use of monochromators to produce highly monochromatic and tunable photon beams of high intensity over a continuous energy region. At various synchrotron facilities around the world, numerous irradiation methods have been established for the treatment of living cells with monochromatic keV x-ray beams.

In 1987, a monochromatic x-ray irradiation system was constructed at the Photon Factory (a 2.5 GeV synchrotron with a maximum electron beam current of about 350 mA) to deliver monochromatic beams with photon energies from about 3 to 15 keV for radiation biology studies (Kobayashi et al. 1987). The implemented monochromator system consisted of reflecting silicon crystals. The tunable x-ray beams propagated in a direction parallel to the incident synchrotron beam (Fig. 4.1). The intensity of the x-ray beam was monitored using an ionization chamber positioned in between the dispersing element and the sample holder. A scanning sample stage was constructed for homogeneous irradiations of biological samples maintained in common culture vessels. Tilted vessels were attached to the sample holder and moved vertically during the irradiation process. The entire stage was placed into an insulated box which allowed the user to control the environmental conditions.

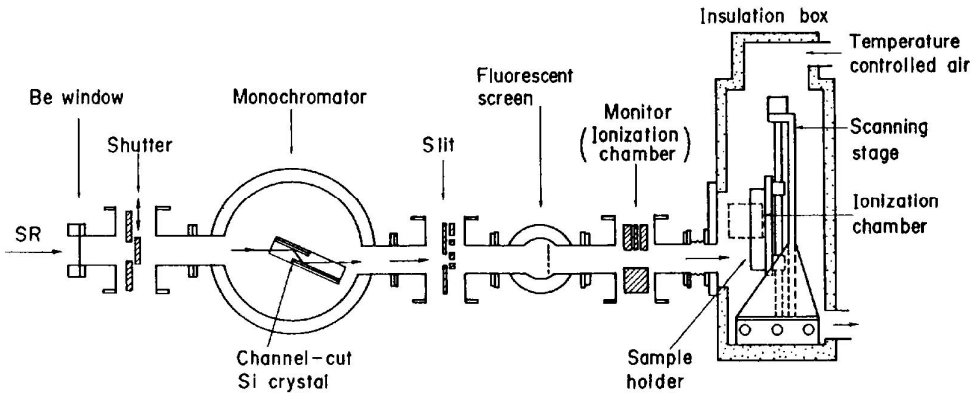

Figure 4.1 Schematic diagram of the monochromatic x-ray irradiation system for radiation biology studies using 3-15 keV x-rays at the Photon Factory in Japan. Reprinted from (Kobayashi et al. 1987).

The implantation of an irradiation system for studies of ionizing radiation damage at Aladdin was first reported in 1991 (Meger Wells et al. 1991). The former 1 GeV electron storage ring, located at the Wisconsin Synchrotron Radiation Center, operated at 0.8 GeV with a maximum electron current of 200 mA. The x-ray lithography beamline ES-0 was equipped with a multilayer filter for energy selection in the ultrasoft x-ray energy region from about 0.2 to 3 keV (Fig. 4.2). The intensity of the reflected x-ray beam was monitored by a fixed ionization chamber positioned in between the monochromator and the sample holder. The implemented scanning system enabled the irradiation of customized culture dishes with bottoms of thin Mylar foil. During irradiations, the dishes were placed onto the sample holder and aligned perpendicular to the monochromatic x-ray beam so that the beam first passed through the bottom of the dish. An experimental chamber isolated the entire scanning apparatus from the environmental conditions at the beamline. Ports at the bottom allowed the chamber to be filled with pre-defined gas compositions.

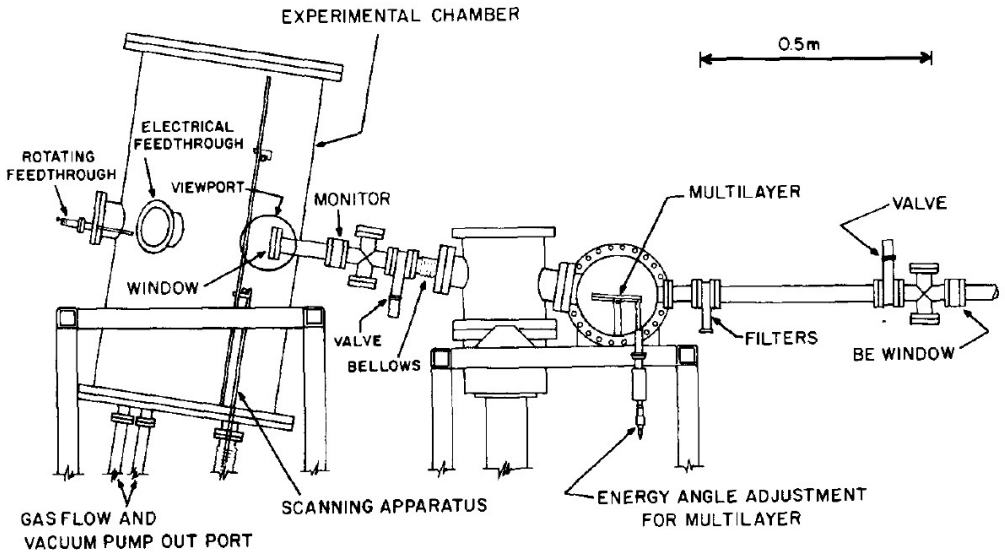

Figure 4.2 Schematic diagram of the monochromatic x-ray irradiation system for cell exposures to 0.2-3 keV x-rays at Aladdin in the USA. Reprinted from (Meger Wells et al. 1991).

More recently, several radiobiological studies have been conducted at the ESRF (electron energy: 6 GeV; maximum electron current: 200 mA). A fixed-exit monochromator, made of a pair of Si(1,1,1) crystals oriented in Laue geometry, provides broad X-ray beams that traversed parallel to the propagating direction of the synchrotron beam (Suortti et al. 2000). The available monochromatic photon energy ranges from about 18 to 80 keV. The inhomogeneity of the approximately 40-mm-wide beam is less than 20%. Beamline users can utilize a vertical translation device for homogeneous biological sample scans (Fig. 4.3). Completed *in vitro* studies include the irradiation of adherent cells in culture flasks placed perpendicular to the x-ray beam (Corde et al. 2002), the irradiation of cell suspensions in permanently rotating cryotubes (Biston et al. 2004), or the irradiation of cell solutions in PTFE capillaries in water-filled cryotubes (Bobyk et al. 2013).

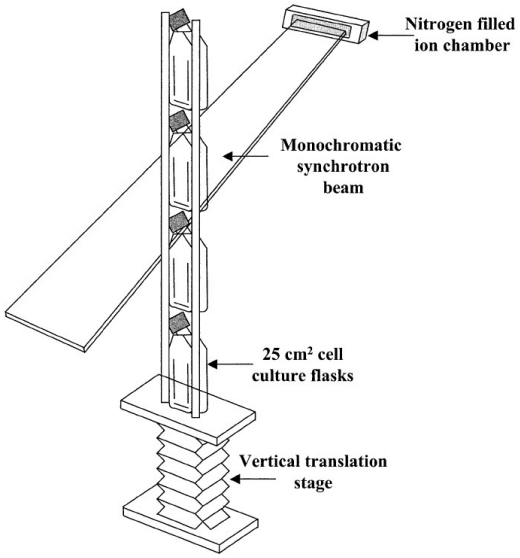

Figure 4.3 Schematic view of the vertical translational set-up enabling homogenous irradiations of biological samples with 18-80 keV x-rays at the ESRF in France. Reprinted from (Corde et al. 2002).

A promising irradiation concept was developed at the Louisiana State University's Center of Advanced Microstructures and Devices (CAMD) (Dugas et al. 2011). At the 1.3 GeV storage ring (operating at a maximum electron current of about 200 mA), a double multilayer monochromator provides monochromatic light in form of a 28-mm-wide beam for the exposure of living cells to keV x-ray beams. As recently applied at their tomography beamline, the cell growing surface of a cell culture tube can be positioned at an angle of 24.6° to the incident monochromatic 35 keV x-ray beam (Fig. 4.4). Before the irradiation process, the tubes must be filled with culture medium and attached to the vertical translational stage. The cells are exposed to x-rays by moving the tube up and down through the monochromatic beam. In contrast to the use of culture tubes or capillaries, this approach allows the irradiated cells to proliferate in a single culture vessel throughout the course of the experiment. Unfortunately, details about the sample handling during the transportation and storage at the radiation facility have not been reported anywhere. No answers have been forthcoming whether the seeded cells properly adapt to the adverse tilted orientation.

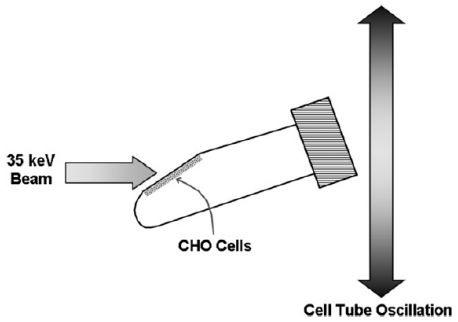

Figure 4.4 Schematic of the cell irradiation arrangement as performed at CAMD in the USA. Biological cells, located dorsally on the tube at an angle of 24.6° to the incident beam, are moved vertically during irradiations. Reprinted from (Dugas et al. 2011).

Another approach for the irradiation of living cells has been recently presented at the Pohang accelerator laboratory (electron energy: 3 GeV, maximum electron current: 400 mA) beamline 1B2 (Choi et al. 2012). By using a special well device filled with culture medium, anchored cells on a Kapton film can be treated with monochromatic 7.1 keV x-rays (Fig. 4.5). As shown in the schematic illustration, the cells are positioned perpendicular to the monochromatic X-ray beam and moved vertically during the irradiation process.

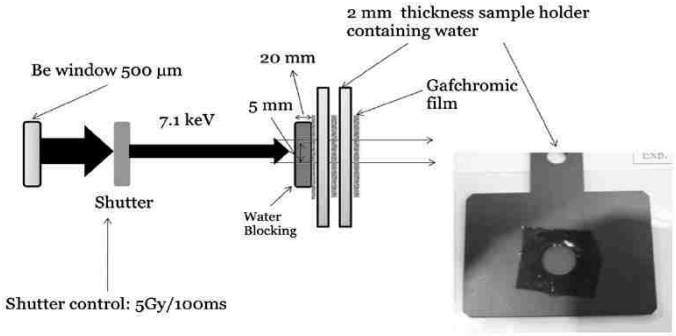

Figure 4.5 Schematic view of the irradiation setup at the Pohang accelerator laboratory in Korea. Reprinted from (Choi et al. 2012).

As observed in the most recent irradiation studies at the BL20XU beamline (Fig. 4.6) (Rahman et al. 2014) and at the B16 and I15 beamlines at the Diamond Light Source Synchrotron (McQuaid et al. 2016), experimental set-ups for the irradiation of living cells with synchrotron light are generally designed around vertical sample translations with compromises on the culture conditions during the irradiation process. Unfortunately, the irradiation geometry and the resulting consequences on the integrity of the targeted cells have never been critically discussed in the existing literature. At the interface between synchrotron science and cell biology, conducting reliable and consistent studies is compromised by the requirements defined by each discipline. In the case of cell culturing, cell type-specific culture conditions must be strictly adhered to in order to avoid unwanted or artefactual consequences ranging from aberrant cell phenotypes to a complete failure of the cell culture. For example, altered culture media volumes can influence cellular metabolic rates and levels of enzyme activities as demonstrated for human kidney cells (Gstraunthaler et al. 1999). In radiation therapy, low ambient temperatures during *in vitro* irradiations have a sparing effect and DNA damage appears to be dependent on the temperature at exposure (Lisowska et al. 2013).

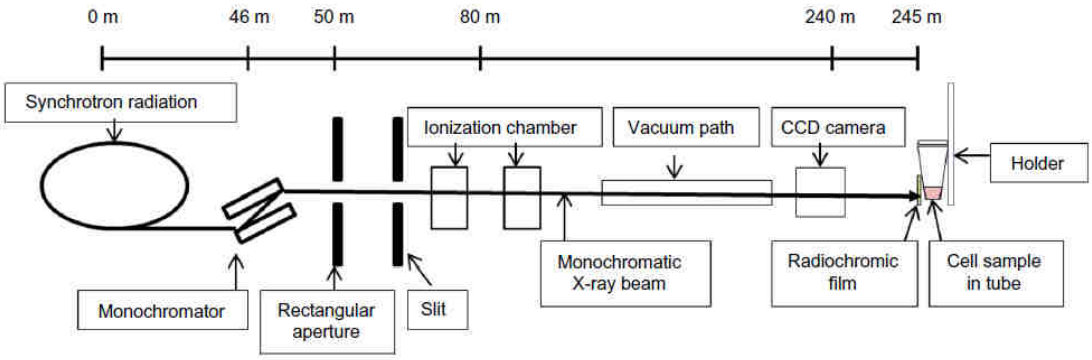

Figure 4.6 Schematic diagram of irradiation set-up at the BLU20XU beamline located at the Spring-8 Biomedical Imaging Center in Japan. Reprinted from (Rahman et al. 2014).

The presence of questionable environmental conditions as a result of the compromising irradiation geometry can directly influence the cellular behavior. In addition, the executed cell culture procedures often consist of numerous labor-intensive, time-consuming, and error-prone steps such as cell transfers from irradiation vessels to dishes or flasks. Every inevitable step adds more experimental parameters to an already large number of variables that must be controlled throughout the course of the experiment. For example, cell transfer among culture vessels requires physical (scraping) or biochemical (trypsinization) detachment of adherent cells, centrifugation, resuspension, and reattachment. Each of these steps must be considered as a potential cellular stress factor. In the worst case, some parameters remain undefined as uncontrolled factors, which may mediate the cellular response to ionizing radiation. Additive, sub-additive, or perhaps even supra-additive effects consequently lead to false interpretations regarding the radiobiological effectiveness of administered enhancement agents or even the radiation itself; hence radiation biologists are hindered from undertaking meaningful research at synchrotron beamlines. Insofar as an intended experimental approach provides deviated culture conditions, a plethora of preliminary studies is required to confirm the suitability of the planned irradiation experiment and to guarantee the correctness of the collected results.

This chapter introduces a novel concept for the irradiation of adherent cells with monochromatic keV x-rays. Motivated by the establishment of an *in vitro* procedure that circumvents the limitation of synchrotron-based irradiation processes, the developed method focuses primarily on the integrity of the primary object of interest: the living cells. Through the implementation of a horizontal scanning procedure rather than a vertical translation, it is possible to conduct sample-oriented and stress-minimized monochromatic keV x-ray studies that allow the treated cells to proliferate undisturbed and uninterrupted under optimal cell type-specific culture conditions not only during irradiations but throughout the entire course of the experiment. The novel irradiation system was established at the Biomedical Imaging and Therapy (BMIT) facility that offer a unique environment particularly for life science research on the basis of x-rays.

4.1. BioMedical Imaging and Therapy Facility at the Canadian Light Source

Canada's national center for synchrotron research, the Canadian Light Source (CLS), is located on the grounds of the University of Saskatchewan. Being one of the largest science projects in Canadian history, the world-class facility's goal is to enhance the expertise in synchrotron science and to promote the utilization of synchrotron light across a range of scientific and industrial areas (Cutler et al. 2007). The CLS is at the edge of the new generation of 3 GeV sources and generates intense synchrotron beams with small divergence resulting in a beam brightness millions of times greater than any laboratory source of x-rays (Bancroft 2004). The facility consists of the following four main components: a linear accelerator, a booster synchrotron, an electron storage ring, and a number of specific synchrotron beamlines (Fig. 4.7).

Electrons emitted from a hot tungsten filament are directly accelerated in a high vacuum by the below-ground linear accelerator. The 250 MeV electrons are then transferred through a transfer line 78 m in length to the ground-level booster ring, where the energy of the electrons is increased to the operation energy of the storage ring. The high-energy electrons are subsequently injected into the storage ring where they circulate for several hours. The maximum electron current of 250 mA after electron injections exponentially decays to about 150 mA over a time frame of about 12h. The very compact storage ring (170 m in circumference) has a 12-fold symmetry with 24 bending magnets in 12 cells to bend the electrons around the entire storage ring. The cells are

connected to each other by twelve straight sections (about 5.2 m long) with nine sections used for insertion devices (i.e. undulators, wigglers).
Bending of the high-energy electrons either by the bending magnets or the insertion devices produces beams of synchrotron light with a continuous energy spectrum. These intense synchrotron beams pass through beamlines optimized for the performance in specific photon energy regions and for specific analytical methods (e.g. x-ray crystallography, x-ray absorption spectroscopy, etc.).

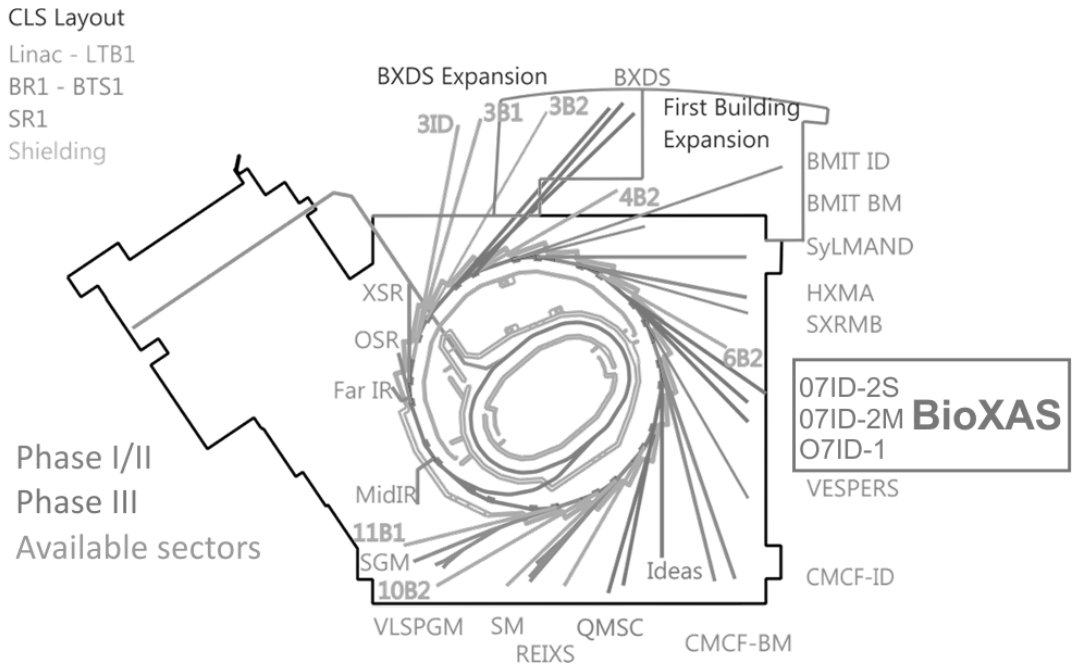

Figure 4.7 Floorplan of the Canadian Light Source. Reprinted from (CLS 2016).

The BioMedical Imaging and Therapy facility is built for multidisciplinary projects and provides unique synchrotron-specific x-ray imaging and therapy capabilities through their sibling beamlines 05ID-2 (also called BMIT-ID) and 05B-1 (BMIT-BM) (Wysokinski et al. 2007; Wysokinski et al. 2013).
While the superconducting wiggler beamline BMIT-ID is primarily designed for biomedical imaging and microbeam radiation therapy research, its complementary bending magnet beamline BMIT-BM mirrors some of the capabilities of its sister and also act as a testing ground for the development and validation of new imaging and therapeutic methods. Successful and promising applications might be translated to BMIT's insertion device beamline. Both beamlines have the capacity to deliver either monochromatized or unfiltered synchrotron beams with a horizontal spot size of several centimeters. Experiments at the BMIT facility can be conducted in two experimental hutches: POE-2 and SOE-1. While BMIT-BM terminates in POE-2, BMIT-ID optionally terminates in POE-2 or SOE-1. The BMIT facility accommodates several amenities for the preparation of living samples and multiple laboratories including a life science laboratory which was recently opened for CLS users.

4.2. The Irradiation System

The bending magnet beamline BMIT-BM is capable of providing unfiltered synchrotron beams with a width of about 230 mm and a height of about 4.6 mm at a distance of approximately 21 m from the source. The delivery of broad synchrotron beams is crucial for the irradiation of cell cultures commonly maintained in culture vessels such as dishes or flasks, while access to an unfiltered synchrotron beam extends the possibility to develop sophisticated and unique set-up arrangements for irradiation studies.

Experimental hutch POE-2 is permanently equipped with several railing and translational arrangements used primarily for medical applications such as K-edge subtraction (KES) imaging (Zhu et al. 2014). The design of the monochromatic x-ray irradiation system adopted these arrangements that offer unique possibilities for the direct positioning and the alignment of key system components. The available railing, however, restricts the physical dimensions of the proposed system. Railing and translational systems optimized for cell culture irradiations rather than imaging applications could broaden the capabilities of the irradiation system as discussed below.

4.2.1. Design and Implementation

For the implementation and operation of the irradiation system, the beamline was set as follows. The permanently installed double-crystal monochromator remained "opened," meaning that unfiltered synchrotron beams can passage through the optics hutch without being monochromatized. All beamline filters were removed from the synchrotron beam except for the 0.11 mm aluminum filter resulting in synchrotron beams with a reduced contribution of low-energy photons. The beamline slit system was set accordingly to narrow the beam spot size to about 1 mm in height and 40 mm in width at the center of the optics table in POE-2.

The irradiation system itself consisted of the following three main components: a dispersing element made of a single bent silicon crystal in Laue geometry, an ionization chamber for monitoring the x-ray beam intensity, and a translational system for horizontal sample scans. The arrangement of the main components is schematically illustrated in Figure 4.8.

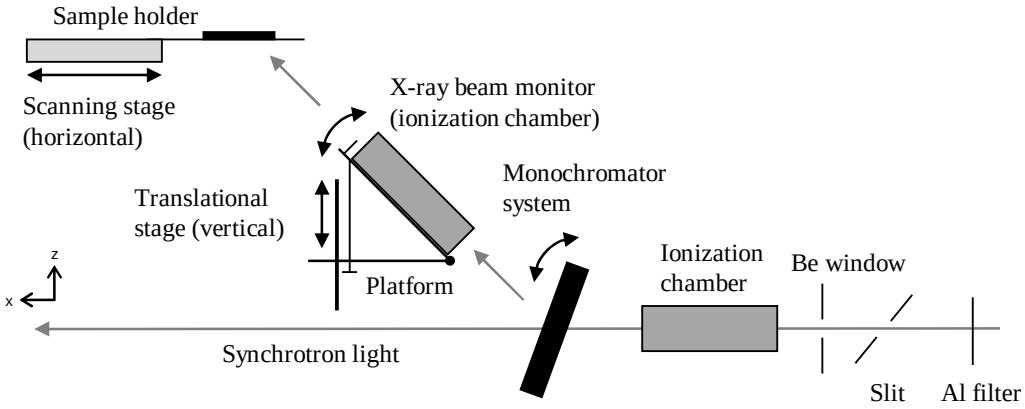

Figure 4.8 Schematic illustration of the monochromatic keV x-ray irradiation system. The direction of the synchrotron beam is depicted by the horizontal arrow. The diffracted monochromatic beam is depicted by the diagonal arrows.

The crucial feature for horizontal cell culture irradiations was a single crystal monochromator oriented in Laue transmission geometry. When synchrotron light impinged on one side of the Laue monochromator, diffracted monochromatic x-ray beams emerged at the other surface in accordance with the Bragg conditions. Initially manufactured for synchrotron-based KES imaging, the physical characteristics of the available silicon wafer was based on the theoretical work by H. Zhang as thoroughly described in her dissertation (Zhang 2009). The key parameters of the silicon wafer are listed in Table 4.1.

Table 4.1 Key parameters of the bent Laue monochromator.

Material	silicon
Wafer width	about 127 mm (5 inch)
Wafer surface plane	(5,1,1)
Crystal thickness	600 µm
Asymmetry angle χ^*	3.3°
Crystal bending radius	3.13 m
Source-to-Crystal distance	about 21 m

*angle between the actual surface plane and the wafer surface plane

The 600 µm thick asymmetric cut silicon (5, 1, 1) wafer with an asymmetry angle of $\chi = 3.3°$ was cylindrically bent to a radius of 3.13 m. The four-bar bender was mounted onto a swivel stage (Kohzu, SA16A-RS) driven by a stepper-motor (Vexta, RK-Series) to adjust the monochromator tilting angle. The entire monochromator set-up was placed onto a translational arrangement for horizontal movements which is permanently installed on the first optics table in POE-2. The translational stage enabled the adjustment of the monochromator horizontal position along the synchrotron beam. By reducing the distance to the source, it was possible to monitor the intensity of beams characterized by narrow diffraction angles. Otherwise, the high-energy beams would have passed right below the ionization chamber whose vertical position was limited by the vertical railing. The overall suitability of the monochromator and its unique capacity to generate monochromatic x-ray beams with energies around the iodine K-edge was recently demonstrated for spectral-KES imaging (Zhu et al. 2014).

A non-pressurized air-filled ionization chamber (FMB Oxford, IC Plus 150), with an electrode length of 150 mm and an electrode separation of 10 mm, monitored the intensity of the monochromatic x-ray beam. The ionization chamber was mounted on a platform consisting of two optical boards that pivoted at the front by two hinges. The ionization chamber tilting angle had to be manually aligned to the direction of the diffracted beam using two bolts at the end of the lower optical board. The platform provided additional space for a photo diode holder installed roughly 50 mm behind the ionization chamber rear window. Retractable fluorescence screens at the ionization chamber front and rear side supported the vertical alignment of an additional photo diode with a laser-based optical level before the installation of the fully-equipped platform in POE-2. The ionization chamber platform was mounted on the computer-controlled motorized linear stage (Parker-Daedel, 404XE Series) which belonged to the permanently installed POE-2 railing arrangement.

A high voltage unit (Ortec, 556H) supplied the chamber operating voltage of 500 V. The ionization chamber output current was pre-amplified (Stanford Research Systems, SR570). The generated voltage signal was collected at the data acquisition device (National Instruments, BNC-2110) and converted into a digital signal (National Instruments, NI PXI-6284). The intensity of

the diffracted x-ray beam energy varied due to the spectral photon distribution in the filtered synchrotron beam. Suitable amplification sensitivity values for a beam with a spot size of 1 mm × 20 mm were 5 nA/V for 11.9 keV x-rays, 10 nA/V for a 12.7 keV x-rays, and 20 nA/V for x-ray energies of 18.0 keV and beyond.
The scanning sample holder was a U-shaped plate made of Plexiglas. The holder was attached to a motorized linear stage (Kohzu, XA30A) for horizontal translation and centered to the x-ray beam. Kapton film (thickness: 13 µm) covered the spared area of the U-shaped plate. A culture vessel placed onto the Kapton was moved along the horizontal direction through the diffracted x-ray beam. Selecting the stage scan velocity defined the exposure time and consequently the irradiation dose. The horizontal and vertical beam dimensions at the sample position were set through the BMIT-BM control software.
Bricks and flat sheets of lead had to be placed beneath the ionization chamber and sample holder to shield the sample from x-ray diffractions emitted by the crystal and scattered radiation. For better visualization of the main components, all lead shielding were removed from the irradiation system as shown in Figure 4.9. At least two video cameras monitored all ongoing events in POE-2 in real time. The live-streams were available at the BMIT control station.

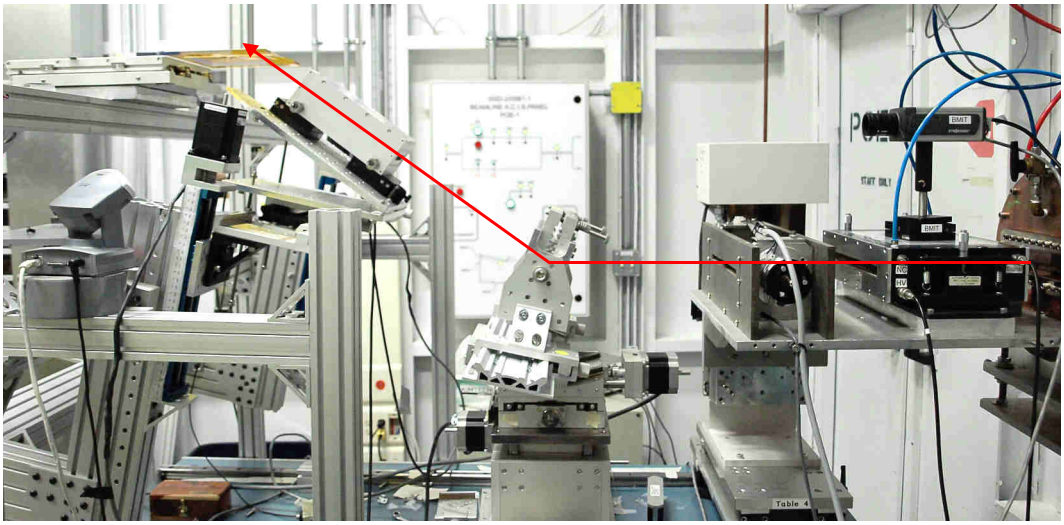

Figure 4.9 The monochromatic keV x-ray irradiation system implemented at the bending magnet beamline BMIT-BM. The synchrotron beam is depicted by the horizontal line. The diffracted monochromatic beam is depicted by the diagonal arrow.

All translational stages were remotely controlled and, in contrast to the tilting angle of the ionization chamber, could be set during online sessions. The most challenging and time-consuming task was the alignment of the ionization chamber towards the direction of the selected diffracted x-ray beam. First, it was necessary to manually align the chamber tilting angle to the Bragg angle of the corresponding photon energy using a digital protractor. After that, the tilted chamber was driven into the vertical position so that the diffracted beam passed through the center of the front and rear window. To confirm the correct vertical position, two video cameras simultaneously monitored the beam spots at both windows, each partly covered with fluorescence paper. Once the correct vertical position was found, several more iterations were required to fine-tune the ionization chamber tilting angle. To accomplish the optimal tilting angle, it was necessary that the beam spots disappeared at both ionization chamber windows at the same time while moving the ionization chamber slowly out of the beam.

The successful alignment of the monochromator tilting angle and the subsequent positioning of the ionization chamber could be achieved within less than one hour. However, a motorized platform entirely controlled from the user station outside POE-2 would tremendously shorten the time-consuming alignment procedure. The remote control of the ionization chamber tilting angle would speed up the required energy calibration process. Also, storage of the complete list of monochromator parameters for pre-defined x-ray energies could simplify the calibration procedures by reusing verified experimental settings.

4.2.2. Diffracted Beam Energy and Energy Calibration

Depending on the beam geometry, x-ray diffraction from a single crystal can be described by Bragg reflection or Laue transmission. If the incident x-ray beam and the diffracted beam both appear on the same side of the crystal, it is called Bragg diffraction. If the incident beam impinges on the crystal surface and the diffracted beam emerges from the opposite surface, the crystal is oriented in Laue geometry (Fig. 4.10A). In both cases, the wavelength λ of the diffracted beam is described by $n\lambda = 2d \times \sin\theta$ with θ being the diffraction angle, d representing the spacing between crystal planes, and n being the order of diffraction (Bragg & Bragg 1913). For the reflection at the selected (3,1,1)-plane, the distance between two planes is $d = 0.1637$ nm. For the first order ($n = 1$), the Bragg equation in terms of the photon energy $E_{ph} = hc/\lambda$ is given as follows:

$$E_{ph}(\theta) = \frac{hc}{2d \times \sin\theta} \qquad (4.1)$$

For the proposed set-up, the angle 2θ measured from the horizontal plane of the synchrotron beam must define the direction of the diffracted beam with energy $E_{ph}(\theta)$ as illustrated in Figure 4.10B. Otherwise, it would not be manageable to identify the (3,1,1)-diffracted X-ray beam among the existing x-ray diffractions and to align the ionization chamber tilting angle appropriately.

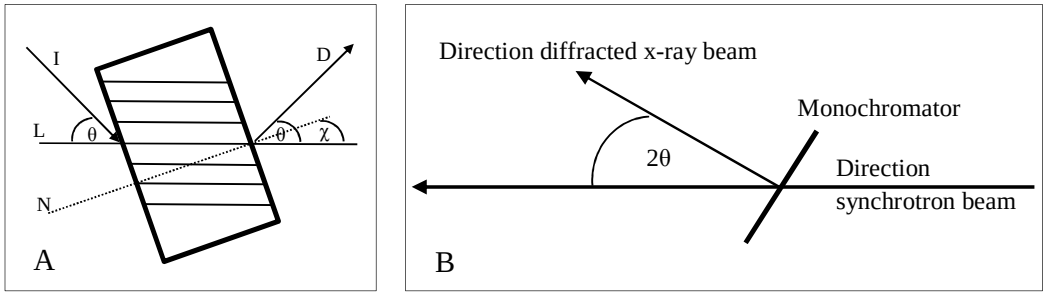

Figure 4.10 Optics and beam geometry for an asymmetric Laue type crystal. (A) The letter I represents the incident ray, D is the diffracted ray, L is the lattice plane, N is the surface normal, θ is the Bragg angle, and χ is the asymmetry angle of the crystal (Zhang et al. 2009). (B) The direction of the diffracted monochromatic x-ray beam is defined by the angle 2θ in the clockwise direction beginning from the direction of the initial synchrotron beam.

Selected reference metal foils are commonly used as calibration standards (e.g. basic foil set by EXAFS Materials). To verify the energy of synchrotron-based keV x-ray beams, the beam intensity across element-specific absorption edges is collected to calibrate the tilting angle of the monochromator to the corresponding ionization energy. For this procedure, a single metal foil was placed in front of the ionization chamber to measure the intensity of a beam (with a defined

height of 1 mm and a width of 20 mm) as a function of monochromator tilting angle. The properties of the selected metal foils, the specific absorption edges, and the corresponding ionization energies are presented in Table 4.2.

Table 4.2 Properties of the reference materials for the x-ray beam energy calibration.

Material	**Symbol**	**Z**	**Density**[a] **(gcm^{-3})**	**Thickness**[b] **(µm)**	**Edge**	**Energy**[c] **(keV)**
Gold	Au	79	19.3	5	Au L_3	11.9
Selenium	Se	34	4.8	325 (mesh)	Se K	12.7
Zirconium	Zr	40	6.5	20	Zr K	18.0
Niobium	Nb	41	8.6	25	Nb K	19.0
Molybdenum	Mo	42	10.3	15	Mo K	20.0
Palladium	Pd	46	12.0	10	Pd K	24.4
Silver	Ag	47	10.4	25	Ag K	25.5

Sources: [a]wolframalpha.com, [b]EXAFS Materials Basic Foil Set Manual, [c]X-ray Data Booklet

A possible angle increment of $\Delta\theta = 0.0014°$ could be set in accordance with the manufacturer's information sheet. A data set consisted of 200 data points with each point representing the mean of 200 independent ionization chamber output current measurements. All LabVIEW programs for the operation of the monochromator system and the data acquisition were written, tested, and approved for use at the beamline by B. Bewer[1]. Since then, all software packages and user interfaces have been accessible for the users at the BMIT workstation.

The collected spectral-beam intensities across the element-specific absorption edges are plotted in Figure 4.11. The edge steps are sufficiently large enough to differentiate the element-specific absorption edge from experimental artefacts associated with malfunctions such as an immediate steep increase of the output signal as a result of a diffracted x-ray beam hitting an ionization chamber electrode. The origin of the most dominant faulty-like feature in the spectra, noticeable as a pre-edge broad peak-like feature in the gold L_3, molybdenum K, and silver K spectrum, remains unknown and could not be reproduced for the gold L_3 and molybdenum K edge at different beamtime sessions. Anyhow, these artefacts remain the only observed anomaly and were neglected as they did not influence the following analytical processes.

[1]Dr. Brian Bewer, BioXAS Science Associate, Canadian Light Source, Saskatoon/Saskatchewan, Canada, 2016. Contact Information: Phone: +1-306-6573851, E-mail: brian.bewer@lightsource.ca

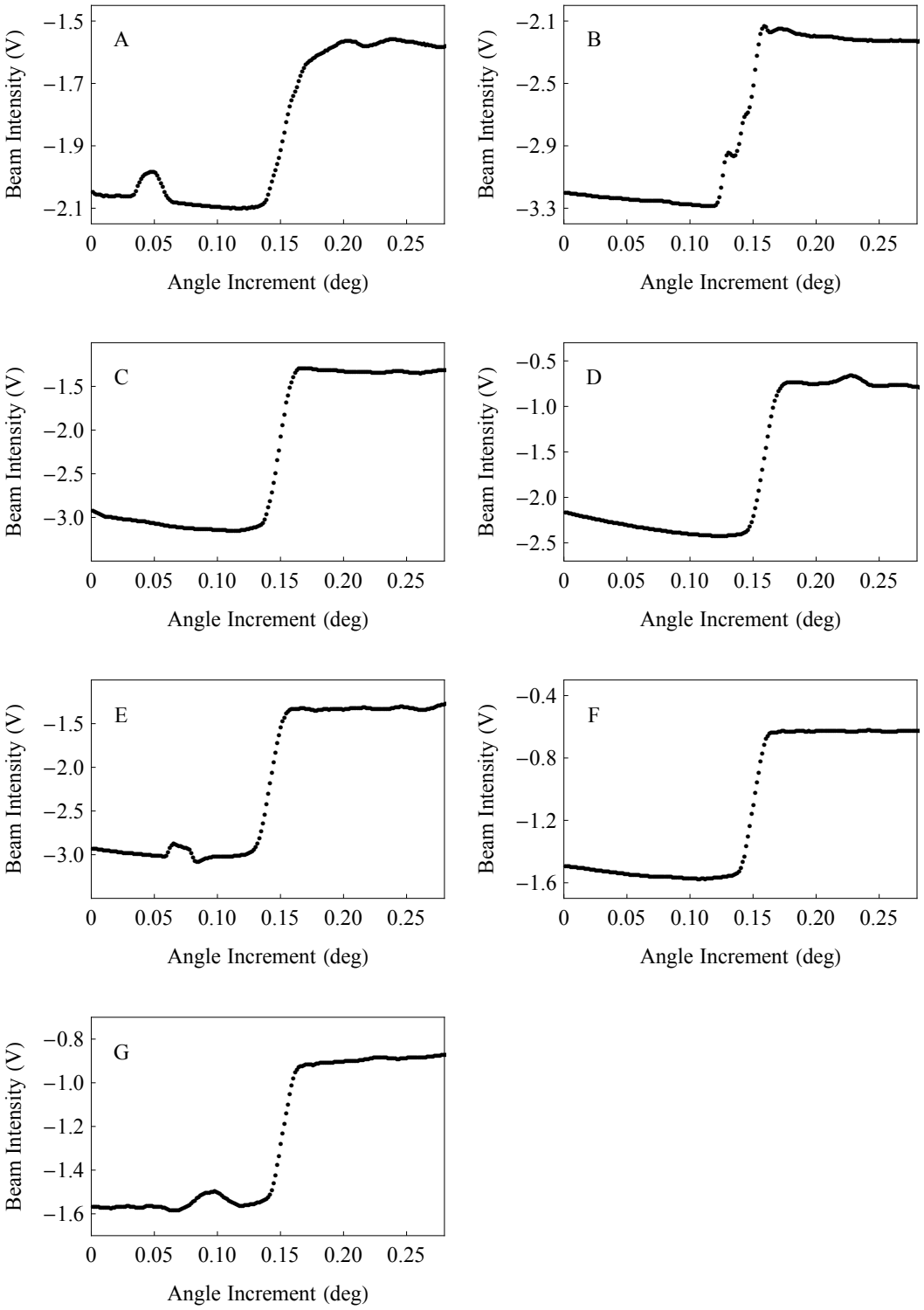

Figure 4.11 Inverted spectral beam intensities across the following edges: (A) gold L_3, (B) selenium K, (C) zirconium K, (D) niobium K, (E) molybdenum K, (F) palladium K, and (G) silver K.

The detail in the spectra exceeded initial expectations in a way that the observed features even resembled characteristic near-edge structures usually seen in x-ray absorption near-edge structure (XANES) spectra. Figure 4.12 compares the gold L_3 XANES spectrum as measured at the Hard X-ray MicroAnalysis (HXMA) beamline and the background-subtracted spectral intensity curve as collected at BMIT-BM. The spectral intensity curve does not only resemble the general shape of the gold L_3-edge, but also contains several post-edge peak-like features as seen in the corresponding XANES spectrum.

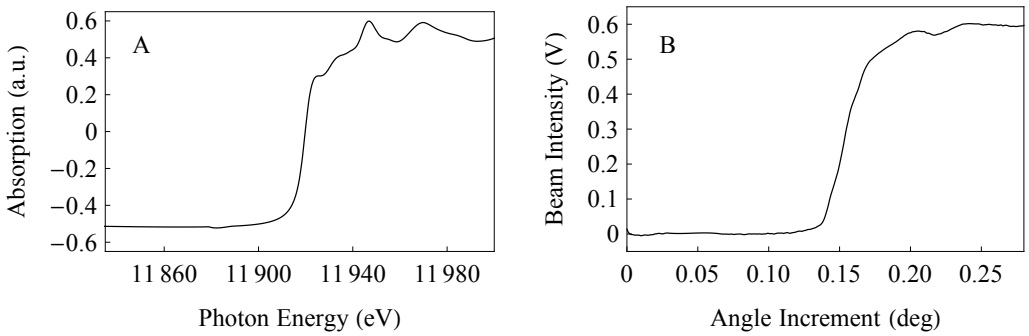

Figure 4.12 Comparison of gold L_3 edge spectra. (A) XANES spectrum of the gold L_3 edge. (B) Intensity spectrum at the gold L_3 edge.

If necessary, an interpolation procedure was applied to remove pre-edge peak-like features from the spectra. A linear fit restricted to the pre-edge region provided the curve baseline which was used to subtract the background signal from the actual signal. Since simplified theory predicts an arctangent-shaped edge with the inflection point at the ionization energy for the gold L shells (Richtmyer et al. 1934), the following trigonometric arc-tangent function appeared to be an appropriate model to describe the shape of the collected signal around the gold L_3 edge:

$$A(\theta) = (A_0 / \pi) \times \arctan(\alpha_A \theta - \beta_A) + B$$

In the above equation, the variable A_0 (V) describes the measured signal height across the absorption edge, B (V) is the vertical offset, and β_A/α_A (deg) is the angle increment shift. For the gold L_3 edge, Mathematica's non-linear fitting algorithm produced converging fits even without the use of initial parameter values. For consistency reasons, the same model was applied to describe the shape of the remaining spectral intensity curves. Table 4.3 summarizes all fit results including the square of the fit correlation coefficient R^2. The direct comparison between the collected spectra and the fit curves confirms that the arc-tangent function is an agreeable choice to model the recorded data sets (see Fig. 4.13 and Fig. 4.14).

The intersection point of the second derivative A"(θ) of the obtained fit curve with the x-axis was consequently an adequate approximation for the inflection point of the collected spectral curve. In this manner, the zero-crossing of the second derivative was used for the calibration of the monochromator tilting angle to the electron binding energy of the corresponding absorption edge (see Fig. 4.13 and Fig. 4.14).

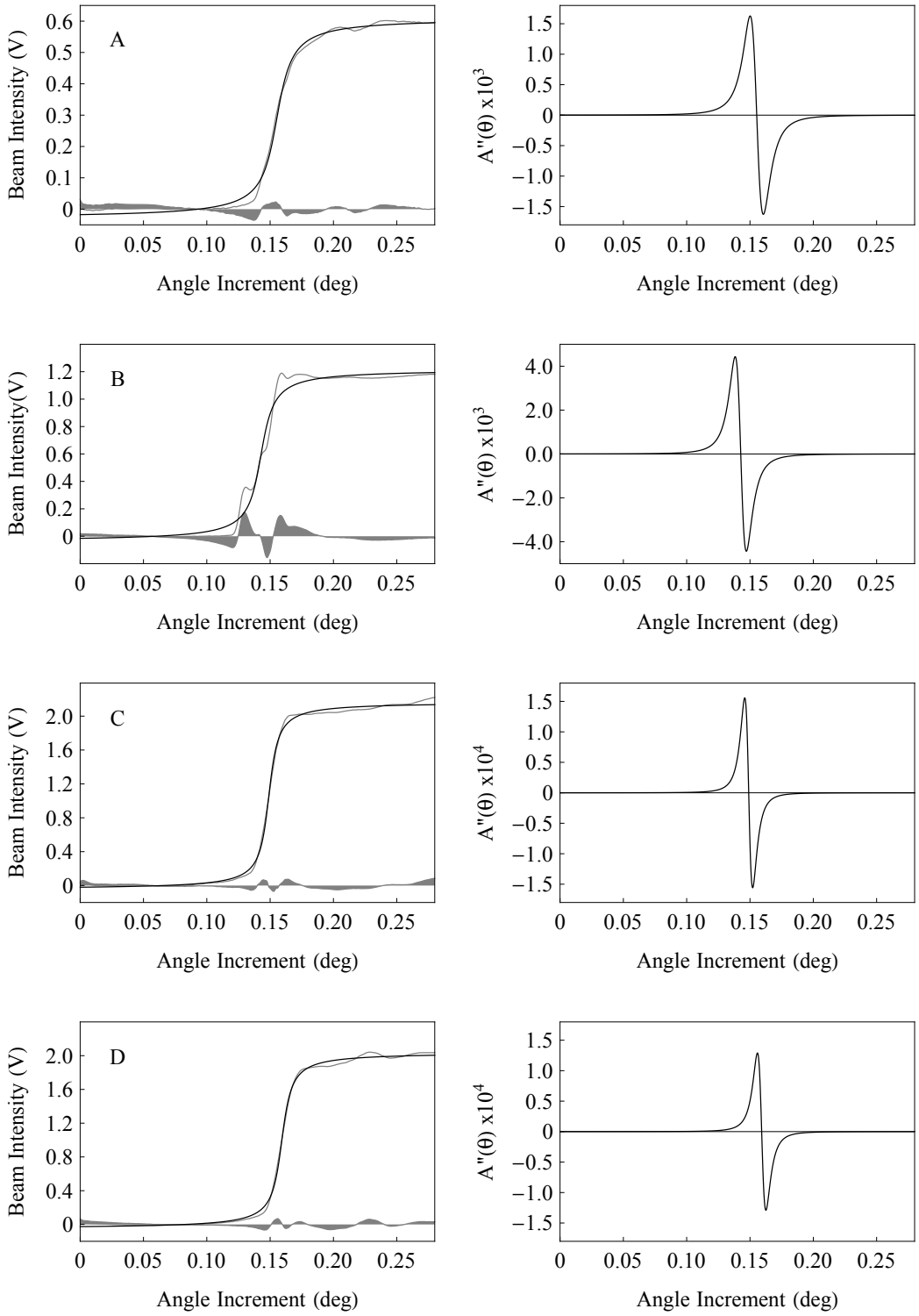

Figure 4.13 Energy calibration procedure (I). Left side: Background-subtracted intensity signal (grey line), arc-tangent fit curve (black line) and the calculated difference between the two curves (grey area). Right side: second derivative of the computed arc-tangent fit curve. Absorption edges: (A) gold L_3, (B) selenium K, (C) zirconium K, and (D) niobium K.

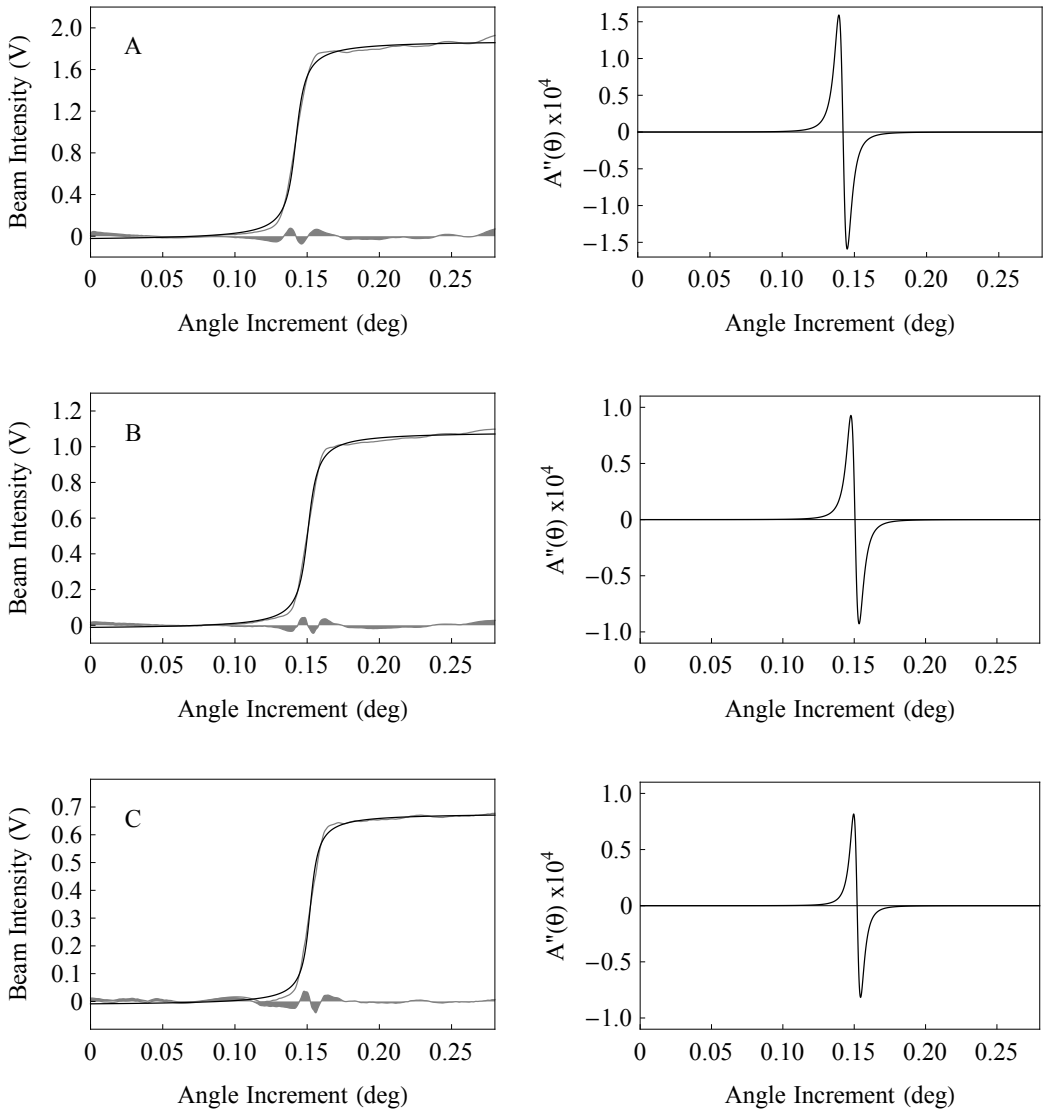

Figure 4.14 Energy calibration procedure (II). Absorption edges: (A) molybdenum K, (B) palladium K, and (C) silver K.

Once the monochromator angle was properly set to hit the first absorption edge, the energy of the diffracted x-ray beam could be moved directly from an absorption edge to another. The linear relationship between the actual tilting angle of the monochromator apparatus and the Bragg angle even enabled to adjust the monochromator set-up to any desired photon energy in between the tested absorption edges. Future studies can be designed around the system's ability to provide well-defined photon energy within the tested energy region from 11.9 to 25.5 keV.

Two features narrowed the available energy region for the monochromatic x-ray beam. At the lower end, the contribution of low-energy photons was reduced due to beam-hardening effects. The intensity of the diffracted beam diminished rapidly with decreasing photon energy below 10 keV. Removing all aluminum filters from the synchrotron beam would increase the contribution of low-energy photons in both, the incident and diffracted beams. The translational stage

responsible for the vertical position of the ionization chamber limited the photon energy at the high-energy region. Instead of passing directly through the ionization chamber, x-ray beams with energies above 30 keV would miss the chamber, and instead, pass beneath the beam monitor because of the narrow Bragg angles. For the irradiation system, the lowest possible chamber position set by the translational stage – initially optimized for KES imaging – defined the maximum beam energy which was expected to be around 30 keV.

Table 4.3 Fit results for the monochromator calibration procedure.

Edge	Energy (keV)	A_0 (V)	B (V)	β_A/α_A (deg)	R^2
Au L_3	11.9	0.637 ± 0.001	0.290 ± 0.001	0.153 ± 0.006	0.999
Se K	12.7	1.253 ± 0.004	0.590 ± 0.004	0.138 ± 0.011	0.997
Zr K	18.0	2.207 ± 0.002	1.059 ± 0.002	0.151 ± 0.007	0.999
Nb K	19.0	2.085 ± 0.002	0.993 ± 0.002	0.156 ± 0.007	0.999
Mo K	20.0	1.922 ± 0.002	0.918 ± 0.003	0.140 ± 0.007	0.999
Pd K	24.4	1.108 ± 0.001	0.531 ± 0.001	0.149 ± 0.006	0.999
Ag K	25.5	0.691 ± 0.001	0.332 ± 0.001	0.151 ± 0.006	0.999

4.2.3. Energy Bandwidth and Energy Error

Recent synchrotron-based studies systematically evaluated the role of potential photonactivation agents such as iodinated contrast compounds (Corde et al. 2004) or platinated chemotherapeutic drugs (Biston et al. 2004) around the element-specific K-edges, because the particle composition and energy distribution of any emitted secondary radiation depend on both the therapeutic x-ray energy and the corresponding electron binding energy. To conduct similar studies at BMIT-BM, the irradiation system must generate x-ray beams characterized by narrow energy bandwidths.
The equational description of the energy bandwidth $\Delta E_{ph}(\theta)$ and energy error $\Delta E_{ph}(\theta)/E_{ph}(\theta)$ can be derived from the Bragg equation as expressed in Equation 4.1. The derivative of the photon energy with respect to the Bragg angle is given as follows:

$$\frac{dE_{ph}(\theta)}{d\theta} = -\frac{hc}{2d}(\sin\theta)^{-2}\cos\theta$$

$$\Rightarrow \frac{dE_{ph}(\theta)}{d\theta} = -E_{ph}(\theta)\cot\theta$$

Considering small changes in the Bragg angle, the replacement of the derivative by the differential leads to the following adequate approximation:

$$\frac{\Delta E_{ph}(\theta)}{\Delta\theta} \approx \frac{dE_{ph}(\theta)}{d\theta} = -E_{ph}(\theta)\cot\theta$$

This approximation makes it now possible to calculate the energy bandwidth:

$$\Delta E_{ph}(\theta) = \left|E_{ph}(\theta)\,\Delta\theta\,\cot\theta\right|$$

The energy error at a given photon energy is calculated using the following equation:

$$\frac{\Delta E_{ph}(\theta)}{E_{ph}(\theta)} = |\Delta\theta \cot\theta|$$

Bragg reflection generally describes an idealized condition, meaning that only a sharp energy is selectively reflected. Under experimental conditions, the angular divergence $\Delta\theta$ of the x-ray beam broadens the energy distribution around the photon energy $E_{ph}(\theta)$. The shape of the distribution is described by the Rocking curve with the FWHM (full width at half maximum) used to define the energy bandwidth $\Delta E_{ph}(\theta)$. For a bent Laue monochromator, the energy bandwidth of a specific diffraction plane consists of two separate contributions: the divergence of the incident x-ray beam and the intrinsic angular width of the Laue diffraction due to a change of the Bragg angle over the crystal's thickness (Ren et al. 1999). In general, cylindrically bent Laue monochromators have wide Rocking curves with a flat top.
Instead of measuring the Rocking curves of the selected (3,1,1)-diffraction plane at different photon energies, the collected intensity curves were further analyzed to examine the final energy bandwidth $\Delta E_F(\theta)$. To calculate the square of the final bandwidth $\Delta E_F(\theta)$, the terms of the selected (3,1,1)-diffraction plane bandwidth and the natural line width of a scanned absorption edge, both in quadrature, must be summed up. While the natural line widths of the specific edges are generally known (Krause & Oliver 1979), the diffraction term could not be determined in this work. For this reason, the angular width $\Delta\theta_F$, here defined as the steps to move the monochromator from 10% to 90% of the maximum intensity signal (Fig. 4.15), was determined from an intensity curve and used to calculate the energy bandwidth $\Delta E_F(\theta)$ and the energy error $\Delta E_F(\theta)/E_{ph}(\theta)$ for the selected (3,1,1)-diffraction at the scanned absorption edges.

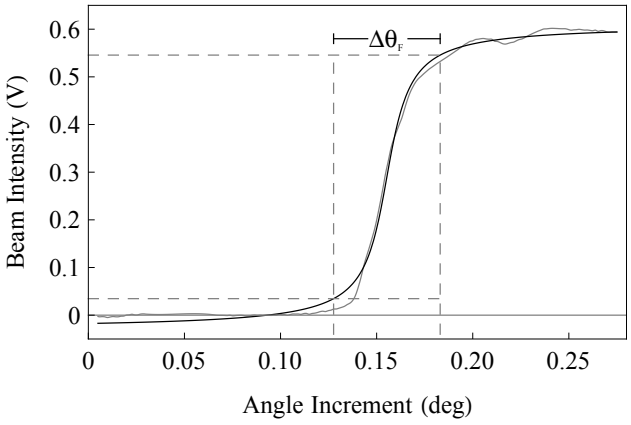

Figure 4.15 Determination of the angular width $\Delta\theta_F$ (depicted by the dashed lines) from the arc-tangent function (black line) computed to model the shape of the Au L_3 intensity spectrum (grey line).

The following approach circumvented the experienced difficulties for the computational algorithm to determine the boundaries of the angular width from the arc-tangent fit curve $A(\theta)$. First, Mathematica's inverse algorithm was applied to calculate the maximum and minimum of the inverse function $A(\theta)^{-1}$. Once the total height of the collected intensity signal was known, the values associated with the variable at 10% and 90% of the maximum signal height were determined to find the corresponding angles θ_{10} and θ_{90}. The obtained angular widths are visualized in Figure 4.16.

To approximate the error $\Delta(\Delta\theta_F)$ of the angular width, the difference between the widths for the curves $A(\theta,\alpha_A)$ and $A(\theta,\alpha_A + \Delta\alpha_A)$, with $\Delta\alpha_A$ being the computed error of the fit parameter α_A primarily responsible for the angular width, needed to be computed. For each spectrum, both widths are plotted in Figure 4.17. The error of the energy bandwidth was subsequently calculated in accordance with the Gaussian error distribution. The results are summarized in the Table 4.4.

Table 4.4 Final energy bandwidth and energy error of the selected (3,1,1)-diffraction plane at distinct absorption edges.

Edge	**Energy (keV)**	$\Delta\theta_F$ **(deg)**	$\Delta E_F(\theta)$ **(eV)**	$\Delta E_F(\theta)/E_{ph}(\theta)$ **($\times 10^{-3}$)**
Au L_3	11.9	0.055 ± 0.002	34.5 ± 1.1	2.89 ± 0.09
Se K	12.7	0.047 ± 0.003	33.2 ± 2.7	2.62 ± 0.18
Zr K	18.0	0.033 ± 0.001	48.6 ± 1.3	2.70 ± 0.07
Nb K	19.0	0.036 ± 0.001	47.9 ± 1.5	3.05 ± 0.08
Mo K	20.0	0.031 ± 0.001	55.8 ± 1.6	2.79 ± 0.08
Pd K	24.4	0.031 ± 0.001	82.8 ± 1.9	3.40 ± 0.08
Ag K	25.5	0.026 ± 0.001	79.1 ± 2.6	3.00 ± 0.10

The final energy bandwidth increased from (34.5 ± 1.1) eV at 11.9 keV to a maximum value of (82.8 ± 1.9) eV as measured at 24.4 keV. The increase of the energy bandwidth as a function of the photon energy can be explained by the line width of the K-shell and the fact that this line width generally broadens with increasing atomic number. For example, the FWHM of the selenium K edge is 2.33 eV, while the silver K edge line width is 6.75 eV (Krause & Oliver 1979). The observation of detailed features in the collected Au L_3 intensity spectrum already indicated that the actual energy bandwidth of the (3,1,1)-diffraction plane was smaller than the obtained final bandwidth at 11.9 keV. However, the results were used to set the monochromator tilting angle with respect to the specific absorption edge. In contrast to $\Delta E_{ph}(\theta)$, the final energy bandwidth provides useful information needed by monochromatic irradiation studies around specific absorption edges. In those experiments, $\Delta E_F(\theta)$ is a suitable parameter to adjust the monochromator tilting angle so that the diffracted x-ray beam consists only of photons with either sufficient or insufficient energies to liberate electrons from the targeted shell.

The energy error for the (3,1,1)-diffraction plane appears to be nearly energy-independent in the tested energy region from 11.9 keV to 25 keV. The calculated order of magnitude (10^{-3}) agrees well with the verified energy errors for single crystal monochromators in Laue geometry.

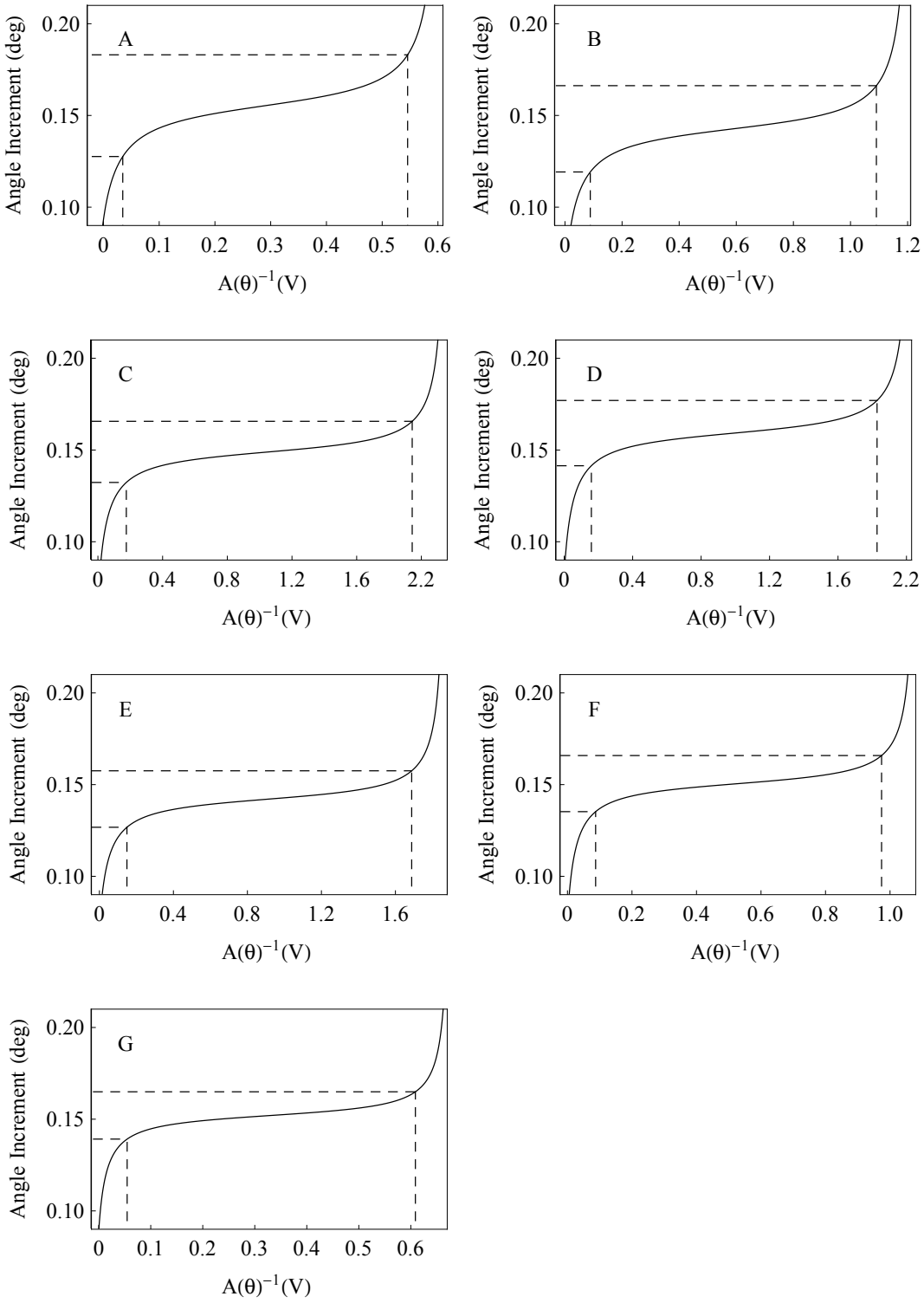

Figure 4.16 Determination of the energy bandwidth. The inverse function $A(\theta)^{-1}$ (black line) and the corresponding angular width $\Delta\theta_F$ (depicted by the dashed lines) are visualized. Absorption edges: (A) gold L_3, (B) selenium K, (C) zirconium K, (D) niobium K, (E) molybdenum K, (F) palladium K, and (G) silver K.

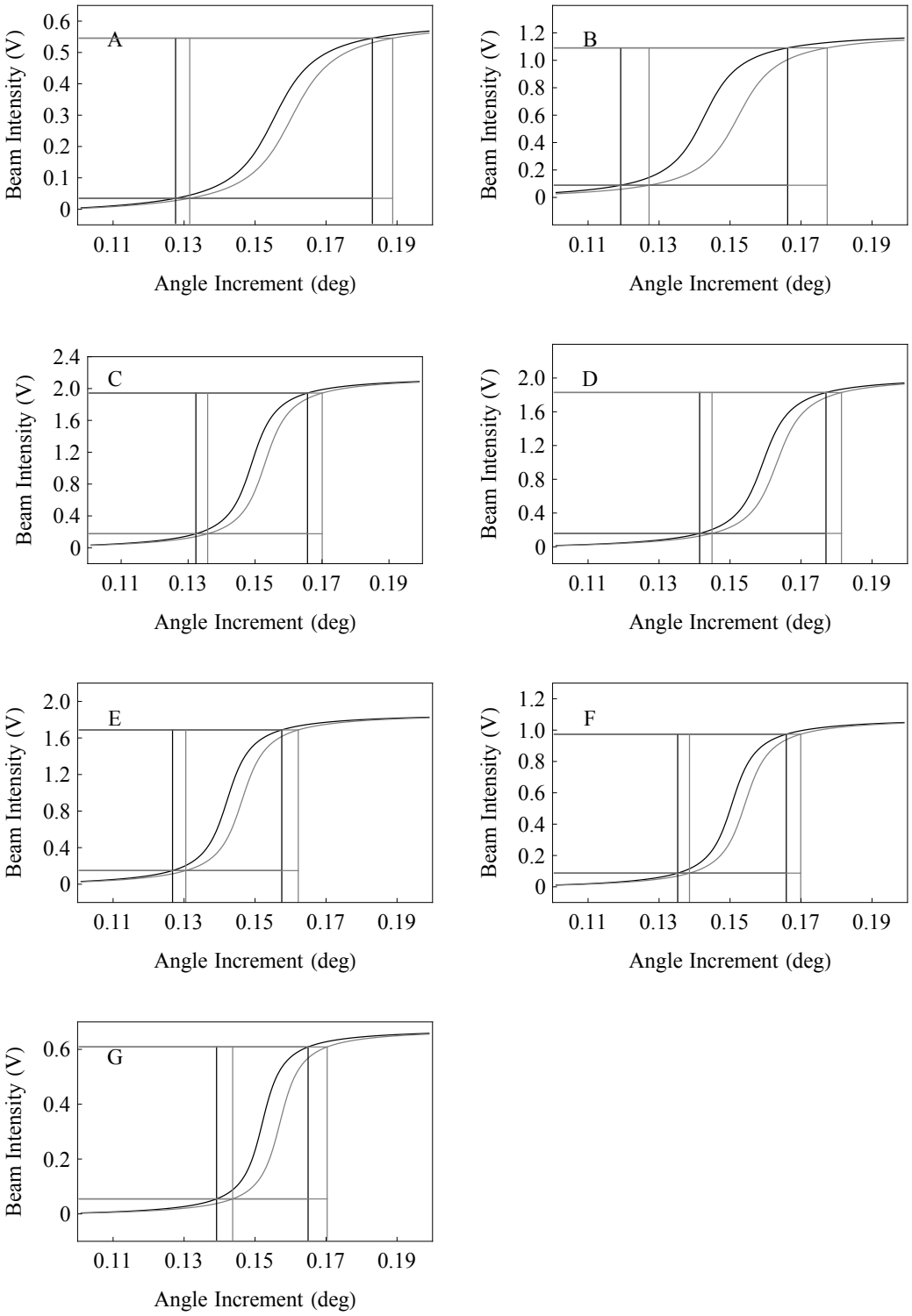

Figure 4.17 Angular widths for the curves $A(\theta,\alpha_A)$ (black line) and $A(\theta,\alpha_A + \Delta\alpha_A)$ (grey line). Absorption edges: (A) gold L_3, (B) selenium K, (C) zirconium K, (D) niobium K, (E) molybdenum K, (F) palladium K, and (G) silver K.

4.2.4. Surface Dose Calculations

For external beam radiation therapy, the absorbed dose is defined as the amount of energy deposited into the unit mass of the irradiated material:

$$\text{Absorbed Dose} = \frac{\text{Deposited Energy}}{\text{Object Mass}}$$

Taking into account the monochromatic character of the x-ray beam, the amount of deposited energy can be calculated by the number of photons N which are absorbed in the mass of the material M multiplied by the energy of the photons E_{ph}:

$$D(E_{ph}) = \frac{N \times E_{ph}}{M} \tag{4.2}$$

The mass M is readily calculated by multiplying the intersected area A with the thickness of the material L times the density of the irradiated tissue ρ_t. The number of photons along the beam path in the irradiated object is described by Beer's law. However, the number of photons N_a depositing energy into the targeted volume differs from the number of absorbed photons. If the number of initial photons is N_0 and a voxel of mass with thickness dx is embedded at a certain length x beneath the surface, the following expression describes the number of photon interactions associated with an energy transfer towards the defined volume:

$$dN_a = N_0 \exp\left(-\mu_T^t \rho_t x\right)\left(1 - \exp\left(-\mu_{EA}^t \rho_t dx\right)\right)$$

with $\mu_T^t = (\mu/\rho)_T^t$ being the total mass attenuation coefficient and $\mu_{EA}^t = (\mu/\rho)_{EA}^t$ being the mass energy absorption coefficient of the tissue material. For the x-ray path length within a volume starting at the surface ($x = 0$) to a certain thickness L, the total number of absorbed photons depositing energy into the targeted mass is calculating using the following equation (Bewer 2010):

$$N_a = \int_0^L dN_a = N_0 \left(\frac{\mu_{EA}^t}{\mu_T^t}\right)\left(1 - \exp\left(-\mu_T^t \rho_t L\right)\right)$$

By inserting this expression for the number of absorbed photons into Equation 4.2, the absorbed dose can be readily calculated in accordance with the equation:

$$D(E_{ph}) = \frac{N_0 E_{ph}}{A \rho_t L}\left(\frac{\mu_{EA}^t}{\mu_T^t}\right)\left(1 - \exp\left(-\mu_T^t \rho_t L\right)\right) \tag{4.3}$$

For a monochromatic x-ray beam with the initial number of photons N_0, the deposited dose depends on the photon energy and the properties of the irradiated target in terms of irradiated area, density, and thickness.

Regardless of whether the irradiation is conducted at the bending magnet beamline BMIT-BM or insertion device beamline BMIT-ID, the biological sample is showered with ionizing radiation in the form of photons with energies below 100 keV. In this energy region, the largest dose is delivered to the surface of the irradiated object, as the number of photons decreases exponentially

when the beam traverses the targeted object. The so-called surface dose D_S can be mathematically derived as the zero-thickness limit of the absorbed dose.
If the exponential part in Equation 4.3 is approximated by the first two terms of its Taylor series:

$$\exp\left(-\mu_T^t \rho_t L\right) \approx 1 - \mu_T^t \rho_t L$$

The equation of the surface dose can be simplified to the following practical expression:

$$D_S(E_{ph}) = \lim_{L \to 0} D(E_{ph}) \approx \lim_{L \to 0} \frac{N_0 E_{ph}}{A \rho_t L} \left(\frac{\mu_{EA}^t}{\mu_T^t}\right) \left(1 - \left(1 - \mu_T^t \rho_t L\right)\right)$$

$$\Longrightarrow D_S(E_{ph}) = \frac{N_0 E_{ph} \mu_{EA}^t}{A}$$

The surface dose rate $\dot{D}_S$ can be calculated after measuring the currently available photon flux $\dot{N} = N/t$ for the diffracted x-ray beam.
If a photon beam with flux $\dot{N}$ passes through the ionization chamber, the number of electrons dn_e liberated per time interval in a volume with thickness dx between the chamber electrodes can be derived by taking the number of photon interactions per unit mass (photon flux per unit area times the total mass attenuation coefficient of air) multiplied by the volume mass and the average number of electrons generated per interaction process

$$dn_e = \frac{\dot{N}}{A_a} \mu_T^a \times A_a \rho_a dx \times \frac{E_{ab}}{W}$$

$$\text{with } E_{ab} = E_{ph} \times \left[\mu_{EA}^a / \mu_T^a\right]$$

where A_a is the cross section of the photon beam traversing the ionization chamber, μ_T^a is the total mass attenuation coefficient of air, μ_{EA}^a is the mass energy absorption coefficient of air, ρ_a is the air density, E_{ab} is the average transferred energy per photon interaction, and $W = 34.4\ eV$ is the average photon energy required to generate an electron-ion pair in air (Barendsen1982). The beam attenuation along the detector length is taken into account by replacing the flux $\dot{N}$ with the exponentially decaying photon rate:

$$\dot{N}(x) = \dot{N}_0 \exp\left(-\mu_T^a \rho_a x\right)$$

The electron current I_{ion} collected at the detector output is the sum of all charges that hit the electrode along the entire electrode length L_{ion}, so the formula for the photon flux $\dot{N}_0$ is related to the collected ionization chamber current (wit q_e representing the elementary charge):

$$I_{ion}(E_{ph}) = \int q_e dn_e = \int_0^{L_{ion}} q_e \dot{N}_0 \exp\left(-\mu_T^a \rho_a x\right) \rho_a \frac{E_{ph}}{W} \mu_{EA}^a dx$$

$$\Rightarrow I_{ion}(E_{ph}) = q_e \dot{N}_0 \frac{E_{ph}}{W} \frac{\mu_{EA}^a}{\mu_T^a \rho_a} \left(1 - \exp\left(-\mu_T^a \rho_a L_{ion}\right)\right)$$

Applying a Taylor approximation for the exponential term further simplifies the derived formula for the electron output current as shown in Equation 4.4 below.

$$I_{ion}(E_{ph}) = q_e \dot{N}_0 \frac{E_{ph}}{W} \mu^a_{EA} \rho_a L_{ion} \tag{4.4}$$

This results in a practical equation for the surface dose rate which depends on the collected ionization chamber output current:

$$\dot{D}_S(E_{ph}) = \frac{I_{ion}}{q_e} \frac{W}{A\rho_a L_{ion}} \frac{\mu^t_{EA}}{\mu^a_{EA}}$$

The attenuation of keV x-ray beams in air and the culture dish bottom motivates the introduction of the additional attenuation factor:

$$\kappa(E_{ph}) = \exp(-\mu_A L_A) \times \exp(-\mu_D L_D(E_{ph}))$$

Here, μ_A and μ_D represent the linear attenuation coefficient of air and polystyrene, L_A is the distance between the ionization chamber and the sample and $L_D(E_{ph})$ is the energy-dependent path length across the culture dish bottom (Fig. 4.18A). The spectral transmission of a monochromatic x-ray beam passing through a Falcon 353001 culture dish with a bottom thickness of d_{dish} = 1.22 mm was calculated using the polystyrene density of $\rho_{pol} = 1.05 \times 10^{-3}$ gcm^{-3} (Fig. 4.18B).

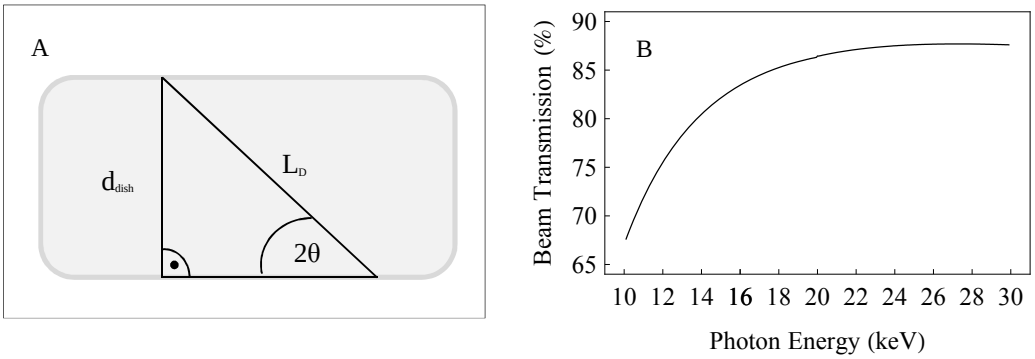

Figure 4.18 Attenuation of diffracted x-ray beams in the bottom of a 35 mm cell culture dish. (A) Schematic diagram for the calculation of the actual beam path length across the culture vessel bottom. (B) Spectral transmission of a monochromatic x-ray beam passing through polystyrene with an energy-dependent path length of $L_D(E_{ph})$.

The actual surface dose D_S^{mod} delivered to the biological sample was therefore calculated using the modified formula:

$$D_S^{mod}(E_{ph}) = \kappa(E_{ph}) \times D_S(E_{ph}) \tag{4.5}$$

The total mass attenuation coefficients and mass energy absorption coefficients of air, polystyrene, and the soft tissue equivalent ICRU-44 are listed in the National Institute of Standards and Technology (NIST) X-ray Database (Hubbell & Seltzer 2009). In this work, the following values were used to calculate the surface dose and the x-ray beam attenuation in air and in the vessel bottom (Tab. 4.5).

Table 4.5 Total mass attenuation coefficient and mass energy absorption coefficient of selected materials for 11.9 and 20.0 keV.

Material	Energy (keV)	μ_T (cm^2/g)	μ_{EA} (cm^2/g)
Air	11.9	3.0130	2.6861
	20.0	0.7538	0.5144
Polystyrene	11.9	1.3436	1.0635
	20.0	0.4227	0.1929
Tissue Equivalent (ICRU-44)	11.9	2.8179	2.4884
	20.0	0.7193	0.4657

Considering the actual path-length of the beam passing through the dish bottom and an electron current in the CLS storage ring of 250 mA, the maximum dose rate for the irradiation of an MCF-7 cell culture using a 11.9 keV (20.0 keV) x-ray beam was 0.46 Gy/s (0.81 Gy/s), according to Equation 4.5. Moving the POE-1 aluminum filter out of the synchrotron beam increased the surface dose rate by 38% (11%) at a given photon energy of 11.9 keV (20.0 keV). For a single culture dish treated with 20.0 keV x-rays, the irradiation phase was less than 2 min for delivering a surface dose of 2 Gy (and less than 10 min for 10 Gy) to human cell lines.

High surface dose rates essentially elevate the sample throughout, allowing the irradiation of multiple sample groups during allocated beamtime sessions. As the electron current in the CLS storage ring decreases gradually with time, so does the surface dose rate. The highest dose rates delivered by the irradiation system are available immediately after the injection of electrons into the CLS storage ring. To minimize the cellular exposure to the experimental conditions in POE-2, high-dose samples should be treated preferably during these periods within precious beamtime sessions.

4.2.5. Ionization Chamber Response

A properly calibrated radiation monitor is essential to generate reproducible results that can be placed in a wider context. The International Atomic Energy Agency (IAEA) recommends that each individual instrument used in radiation monitoring should be calibrated before its first use and then again periodically, usually every 12-14 months (IAEA 2000). For *in vitro* irradiation studies at BMIT, calibration of the ionization chamber according to high IAEA standards appears exaggerated. Instead, a more practicable approach was applied to set up irradiation experiments during limited beamtime sessions. In this experiment, the ionization chamber response to keV x-rays was compared to the response of a calibrated photo diode in order to verify the functionality of the ionization chamber as a suitable radiation monitor.

The employed silicon-based diode (International Radiation Detectors, Type: AXUV 100GX) had an active area of 10×10 mm^2 and was previously calibrated at a wavelength shifter beamline BAMline located at the electron storage ring BESSY II (Görner et al. 2001). The measured diode responsivity as a function of the photon energy is plotted in Figure 4.19A.

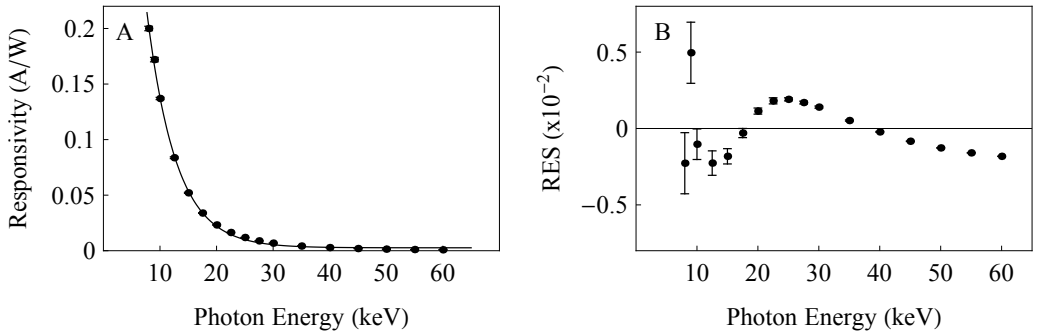

Figure 4.19 Photo diode responsivity. (A) Measured responsivity as a function of the photon energy and the computed exponentially decaying fit curve (black line). (B) Residuals and responsivity errors.

The following exponentially decaying function was used to describe the energy-dependent diode's responsivity R_{pd} in order to obtain approximated values in between the measured data points:

$$R_{pd}(E_{ph}) = R_0 \times \exp(-\alpha_R E_{ph} + \beta_R) + R_B$$

The fit curve with the computed coefficients R_0 = (0.076 ± 0.003) A/W, α_R = (0.194 ± 0.004) 1/keV, β_R = (2.5194 ± 0.0002), and R_B = (0.0026 ± 0.0008) A/W is plotted on top of the measured responsivity in Figure 4.19A. Although the pattern in the residual plot (RES = $R_{pd,observed} - R_{pd,expected}$) suggests that the model has room for improvement (Fig. 4.19B), the applied exponentially decaying curve was a sufficient approximation to estimate the diode's responsivity across the tested photon energy region.

To verify the ionization chamber response, the photo diode position had to be properly aligned to the center axis of the ionization chamber. First, the horizontal position of the photo diode holder was set to the center of the ionization chamber. A laser band optical level was used to align the vertical height of the diode to the ionization chamber windows. These alignment steps had to be performed before the ionization chamber platform was attached to the POE-2 railing system. To avoid an offset in the beam flux measurements, a black box with small Kapton windows on the front and rear sides shielded the diode from exposure to incident light emitted by indirect sources in the experiment hall. The applied spot size of the diffracted x-ray beam had to fit into the dimension of the active area and the hole in the diode holder (diameter of 7 mm). Therefore, the presented results reflect the response of the diode and ionization chamber to x-ray beams with a reduced width of 3.5 mm and a height of 1.1 mm at the diode position. The beam flux $\dot{N}_{pd}$ measured by the photo diode was calculated according to

$$I_{pd}(E_{ph}) = R_{pd} \times \dot{N}_{pd} \times E_{ph}$$

with $I_{pd}(E_{ph})$ being the collected diode output current. The determined beam flux $\dot{N}_{pd}$ was then compared to the beam flux $\dot{N}_{ion}$ as monitored by the ionization chamber using Equation 4.4. The collected flux values were further normalized to the electron current in the CLS storage ring to eliminate any disparities caused the by the gradual loss of electrons with time. All software

packages for the data acquisition were written and implemented at BMIT-BM by Mr. Bolibruch[2]. The normalized beam flux as determined by the photo diode and ionization chamber, along with the diode responsivity for 11.9, 20.0 and 25.5 keV x-ray beams are listed in Table 4.6.

Table 4.6 Comparison between the normalized flux as measured by the photo diode and ionization chamber.

Energy (keV)	**Responsivity R_{pd} (A/W)**	**Norm. Diode Flux $\dot{N}_{pd}$ (#/(mAs))**	**Norm. Chamber Flux $\dot{N}_{ion}$ (#/(mAs))**
11.9	0.096 ± 0.007	$(1.64 \pm 0.08) \times 10^7$	$(2.70 \pm 0.07) \times 10^7$
20.0	0.023 ± 0.001	$(1.30 \pm 0.05) \times 10^8$	$(1.29 \pm 0.04) \times 10^8$
25.5	0.011 ± 0.001	$(1.27 \pm 0.04) \times 10^8$	$(1.25 \pm 0.04) \times 10^8$

As shown in Figure 4.20, the highest normalized fluence ($\Psi = N/(A \times t)$) was measured for the 20.0 keV x-ray beam, while the lower values for 11.9 and 25.5 keV x-ray beams mirror the energy spectrum of the synchrotron beam with a general reduced contribution of low-energy photons. Overall, the fluence as measured by the ionization chamber was comparable to the fluence obtained by the photo diode for 20.0 and 25.5 keV x-ray beams. Assuming that the diode's response to monochromatic keV x-rays was accurately calibrated, the detected discrepancy at 11.9 keV may indicate a certain limitation of the linearity for ionization chamber responsivity in the lower photon region. To resolve this issue, further dosimetry studies need to clarify the actual responsivity of the ionization chamber in the low keV x-ray energy region.
Regardless of the detected discrepancy between the responsivity of the ionization chamber and the calibrated diode, the irradiation system created highly accurate dosimetry results at photon energies of 20 keV and beyond. Below this threshold, the calculated value for the surface dose might be larger than the actual radiation dose delivered to the sample.

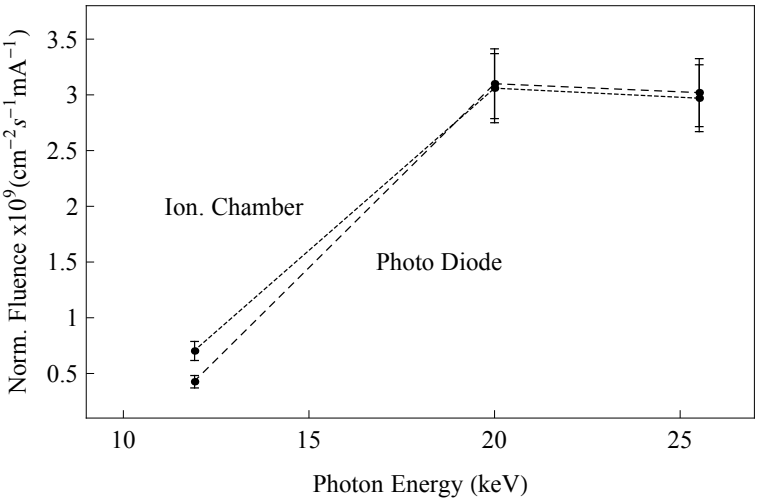

Figure 4.20 Normalized photon fluence rates measured by the ionization chamber (dotted line) and photo diode (dashed line).

[2]Nicholas Bolibruch, Research Associate, Canadian Light Source, Saskatoon/Saskatchewan, Canada, 2010-2013.

4.2.6. Flux Profiles of 11.9 keV and 20.0 keV X-ray Beams

Homogenous irradiations of cell culture across the entire sample area require x-ray beams with high flux uniformity along the horizontal direction of the beam cross section. The flux uniformity along the vertical beam direction can be neglected as deviating effects are averaged out during horizontal irradiation scans.

In this preliminary experiment, the uniformity of the beam flux along the horizontal direction was evaluated using a lead plate with a 2.5 mm wide window. The plate was placed in front of the ionization chamber and moved along the horizontal beam width to measure the beam intensity for each beam segment. One of the segments in at the beam center (segment #8) was used as reference point. All other intensity values were normalized to this segment.

The collected beam profiles of the 11.9 and 20.0 keV x-ray beams are presented in Figure 4.21. Along the horizontal direction, the uniformity increased slightly starting from the end associated with a low segment number. Although the flux remained nearly constant across the entire beam cross section, a steep decrease could be observed for the segments at each end of the x-ray beam. This effect can be explained by the inability to clearly identify the horizontal beam ends during the measurements.

Overall, the irradiation system achieved a beam uniformity which was better than 8% for both photon energies. High uniformity of the x-ray beams minimizes the spread of the delivered dose for a single sample and is therefore an important factor for consistent and well-defined studies.

A certain decrease in beam flux at both beam ends, as determined by the rather unconventional approach, is not necessarily a disadvantage for cell culture irradiations. In properly prepared samples, the biological cells are homogenously seeded over the entire bottom area of the culture vessel. The number of cells which might experience a treatment with a reduced beam flux is negligible, while the risk of accidental exposure of the container walls with intense x-ray beam is reduced.

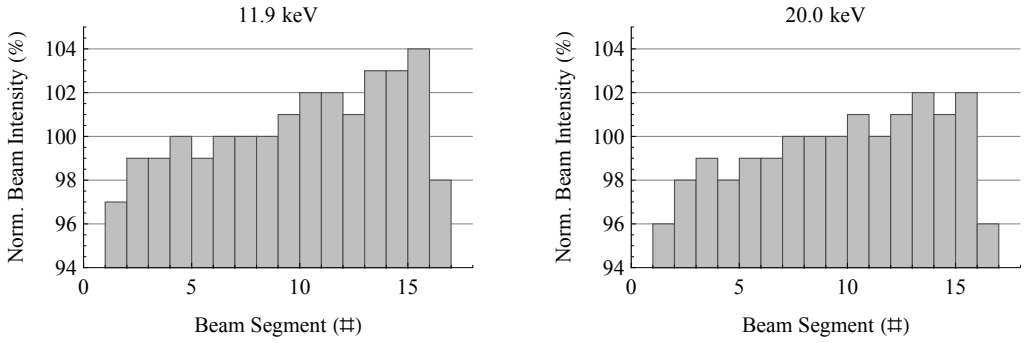

Figure 4.21 Flux profile of the diffracted x-ray beam with a monochromatic photon energy of 11.9 keV (left) and 20.0 keV (right). The relative standard deviation is less than 1% (corresponding error bars are not plotted).

4.3. MCF-7 Dose-Response Curve for 11.9 keV X-rays

This "proof of principle" validates the capabilities of the proposed irradiation system to generate reliable irradiation results that reflect the cellular response to monochromatic keV x-rays. The collected MCF-7 dose-response curve is intended to illustrate how non-perturbing experimental procedures lead to highly accurate and reproducible irradiation results.

The MCF-7 cells were incubated as monolayer cultures in Dulbecco's modified Eagle Medium (DMEM, Invitrogen), supplemented with 10% fetal bovine serum (FBS, Gibco) and antibiotics (100 units penicillin/mL and 100 µg streptomycin/mL, Gibco) at 37°C in a humid incubator continuously gassed with 5% CO_2. At a confluence level of 80%, the cells were enzymatically dispersed, diluted, centrifuged, and resuspended in fresh medium. For the irradiation process, 10^4 cells were seeded in a Falcon 353001 culture dish to a total volume of 2 mL and incubated for 24h. A portable incubator (K-Systems, G95) provided the cell type-specific culture conditions for the MCF-7 cell line during the sample transportation to and from the CSL as well as for the sample storage at the BMIT facility.

To set up the irradiation system, the monochromator tilting angle was calibrated to the inflection point of the collected gold L_3-edge spectrum. The height and width of the calibrated x-ray beam was verified by illuminating photosensitive paper taped to the sample holder. The preamplifier sensitivity was set to 5 nA/V for the calibration procedure and set to 200 nA/V to accommodate the broad beam width during irradiations. The desired scan velocity of the sample holder was calculated in accordance with the surface dose measurements as given in Equation 4.5. The actual path length of the monochromatic 11.9 keV beam through the dish bottom was 2.02 mm (the beam transmission was 75.2%). The attenuation of the beam traversing from the ionization chamber to the sample (about 5 cm) was less than 2%. For the irradiation process, a single culture dish was placed onto the sample holder and moved horizontally through the diffracted beam. The beam spot size was controlled through the BMIT-BM computer interface. All irradiations were performed in single scan mode under the laboratory conditions present in experimental hutch POE-2.

The irradiated samples were immediately returned to the CSL incubator to avoid the occurrence of cellular alterations caused by stressors other than the ionizing radiation itself. According to the modified MTT assay protocol, the post-irradiation incubation phase of three MCF-7 doubling times (87h) was a valuable compromise to detect radiation-induced effects until overpopulation starts distorting the assessments of particularly low-dose samples. The cellular viability rate $VR(D_s)$ as a function of the delivered surface dose D_s was calculated as the mean of the background-subtracted absorbance normalized to the control group. All reported cellular viability rates are depicted as percentage of the control group with each data point representing the mean and standard deviation of four independently treated samples.

As shown in Figure 4.22, the assessed viability rate generally decreased as the dose increased. Irradiation of MCF-7 cells with a dose of 2 Gy reduced the viability rate to about 50%. Beyond this clinically relevant dose level, the cellular viability decreased even further to about 20% as measured for the highest applied dose level of 10 Gy. This observation was confirmed by optical microscopy investigations. The estimated number of living cells within the samples agreed with the measured viability rates and the notion that the detected plateau did not flatten around the zero point. Unfortunately, optical investigations do not distinguish between intact cells and cells which may undergo radiation-induced alterations (e.g. inhibited proliferation). However, all remaining cells in the irradiated samples did not exhibit any histology changes as far as they were detectable using optical microscopy.

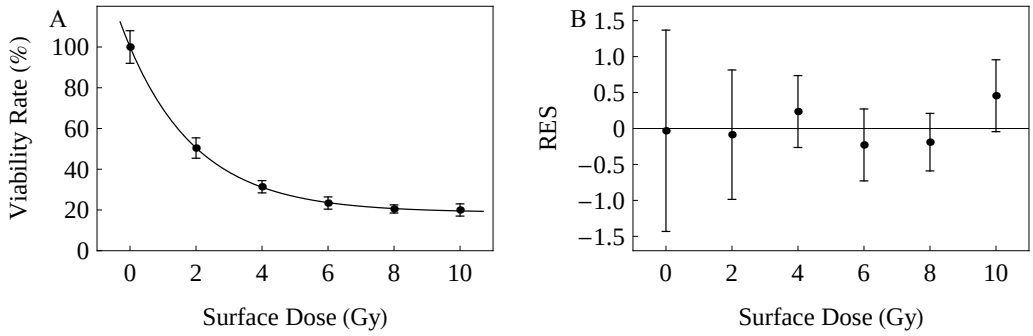

Figure 4.22 Dose-response curve for the MCF-7 cell line exposed to monochromatic 11.9 keV x-rays. (A) Cellular viability as a function of the delivered surface dose and best fit curve (black line). (B) Residual plot and standard errors.

The average relative standard deviation of less than 10% reflects the high reproducibility of the obtained results. The relationship between the cellular viability and the applied dose was further modelled using a normalized first-order exponential decay function:

$$VR(D_s) = \exp(-\alpha_v D_s) + \beta_v$$

Here, α_v (Gy^{-1}) is the rate constant and β_v (%) describes the plateau-like pattern at the upper end of the dose range. The fit results are summarized in Table 4.7. The best fit curve is plotted on top the data points in Figure 4.22A. The small distances of each data point from the fit curve support the appropriateness of the phenomenological model to describe the cellular behavior. The random distribution of both positive and negative residuals ($RES = VR_{observed} - VR_{expected}$) confirms that the irradiation data does not differ systematically from the fit curve (Fig. 4.22B). Due to the random spread of data points above and below the fit line, the obtained residuals can be considered as the primary experimental errors for the collected data set. Further studies may compare the rate constant and constraining plateau with the results obtained for different cell lines or alternated irradiation modalities (e.g. photon energy).

Table 4.7 Fit results for the MCF-7 dose-response curve at 11.9 keV.

Parameter	Estimate	Standard Error	P-Value
α_v	0.471	0.006	3×10^{-7}
β_v	0.188	0.002	3×10^{-10}

Colony formation is the most frequently used method to quantify cell reproduction death after treatments with ionizing radiation (Franken et al. 2006). The collected survival curves are well described by the linear-quadratic formula (LQ-formalism), which assumes that lethal radiation damage is created either as a consequence of a single event (“track”) killing (Type A, represented by the linear term in the formalism) or as a consequence of multiple event killing (Type B, quadratic term) (Pouget & Mather 2001). The exponentially decaying pattern of the collected dose-response curve now indicates that the primary cellular damaging effects induced by 11.9 keV x-rays are similar to the lethal damage described by the linear term in the LQ-formalism,

which is the strongly dominating part, even at higher dose levels, for radiations of high linear energy transfer (high-LET) particles (Barendsen 1982).

Overall, the scientifically satisfying results demonstrate the suitability of the system for reliable and reproducible monochromatic irradiations with highly-controllable experimental parameters. The continuous proliferation of cells within a single dish over the entire course of the experiment – beginning from the preparation, throughout the sample transportation, the irradiation treatment and post-incubation phase to the final analysis – not only elevated the study's reproducibility, but also simplified the sample handling protocol and eliminates unnecessary stress factors through labor-intensive, time-consuming, and error-prone sample preparations or post-irradiation procedures. The ability to move the sample horizontally rather than vertically, together with the use of the portable incubator, facilitated the establishment of non-perturbing cell culture standards in synchrotron-based irradiation studies. As a result, the high accuracy and relative experimental error was considerably smaller than the relative error of 10% as determined for the modified MTT assay.

Horizontal irradiations with monochromatic x-rays offer the possibility to perform clonogenic and viability irradiation assessments under identical experimental conditions. Complementary studies at BMIT-BM using both techniques consequently benefit from a comparability and credibility which, up to this point, remain unachieved by any synchrotron facility. The implementation of an environmental chamber would be one of the most essential improvements to the irradiation system. The development of a sample chamber for controlled atmospheric conditions (i.e. temperature, humidity level, gas composition) would allow cell cultures to be maintained under well-defined environmental conditions during long x-ray exposure times. A second beam slit system in front of the ionization chamber could automatically adjust the beam spot size to the dimensions of the culture vessel. The slit system should be implemented on an improved ionization chamber platform whose tilting angle is computer-controlled from the user station outside POE-2.

The design of the irradiation system comes with abundant space around the sample holder. The integration of additional equipment beneath and, in particular, on top of the sample opens up new pathways for the use of sophisticated live-cell imaging technology in monochromatic keV x-ray studies. Bright-field or phase contrast imaging is widely used to investigate morphological changes during apoptotic, necrotic, or mitotic processes after irradiation (Suzuki et al. 2012). Recently developed imaging systems are even capable of acquiring bright-field, dark-field, and phase contrast images simultaneously in real-time (Liu et al. 2014). While these kinetic observations require extensive amounts of experimental time, rapid visualization techniques based on fluorescence microscopy can even provide insight into the mobility of damaged DNA, the assembly of DNA repair complexes, and other early radiation-induced processes at the sub-cellular level (Karanam et al. 2013). A live-cell imaging system for the study of early and fast cellular response to DNA damage after high LET ion radiation was used to show that strand-break repair protein XRCC1 was recruited to the ion hit position within 20s in the cells and reached a maximum at about 200s (Guo et al. 2016). Functional assessments gain substantial information about the cellular behavior as a direct response to ionizing radiation. A plethora of these functional assays uses fluorescence probe molecules to visualize cellular events such as DNA fragmentation, damage or repair (Fairbairn et al. 1995), DSBs and apoptotic signaling cascades (Gorczyca et al. 1993), or the production of ROS (Gomes et al. 2005). The implementation of fluorescence imaging at BMIT-BM would broaden the prospect for radiobiological insights.

Regardless of the realized live-cell imaging method in future synchrotron-based keV x-ray irradiation applications, the absence of any electron backscattering material within the vicinity of the diffracted x-ray beam path should remain unchanged.

5. The Role of Gold Nanoparticles in Monochromatic X-ray Studies

The work documented in the proceeding chapter of this dissertation was primarily motivated by the pioneer J. Hainfeld who used gold nanoparticles to enhance radiation therapy in mice (Hainfeld et al. 2004). Since then, several research groups have presented improved radiotherapeutic outcomes for different treatment modalities with gold nanoparticles as enhancing agents. For example, gold nanoparticles in conjunction with ionizing radiation retarded tumor growth compared to radiation-only controls *in vivo* (Chang et al. 2008), improved the radiotherapeutic outcomes for a radioresistant mouse squamous cell carcinoma *in vivo* (Hainfeld et al. 2010), and prolonged the long-term survival of brain-tumor bearing mice *in vivo* (Hainfeld et al. 2013). Other research groups proposed that gold nanoparticles increase the apoptosis of MCF-7 adenocarcinoma both *in vivo* and *in vitro* (Roa et al. 2012). Another combined *in vitro* study reported improved radiosensitization efficiency on rats bearing glioma *in vivo* at monochromatic 88 keV x-rays and on F98 glioma cells *in vitro* at monochromatic 50 keV x-rays (Bobyk et al. 2013). Several *in vitro* studies indicate enhanced radiosensitization of various cell lines to ionizing radiation as a direct result of the internalization of gold nanoparticles (Hu et al. 2015; Geng et al. 2011; Polf et al. 2011; Jain et al. 2011; Rahman et al. 2011; Liu et al. 2010; Chithrani et al. 2010; Hébert et al. 2010; Roa et al. 2009; Zhang et al. 2008; Kong et al. 2008). Fundamental studies have presented nanoparticle-mediated radiation effects on cellular constituents such as DNA molecules (McMahon et al. 2011; Brun et al. 2009; Zheng et al. 2009) or proteins (Brun et al. 2009).

The observation of improved radiotherapeutic outcomes has not been limited to the kilovoltage x-ray energy region characterized by the dominating photoelectric effect. Increased radiosensitization *in vitro* has been detected at photon energies of 662 keV (Cs-137), 1.2 MeV (Co-60), and 6 MV beams generated with a linear accelerator (Kong et al. 2008; Roa et al. 2009; Chithrani et al. 2010). Improved therapeutic outcomes have even been observed for electron beams as primary ionizing radiation (Rahman et al. 2009; Chang et al. 2008; Zheng et al. 2008). These findings question the proposed mechanism for the radiotherapeutic effectiveness of gold nanoparticles based on the increased photoelectric absorption in the targeted tissue. Instead, some authors have apparently identified cellular and sub-cellular events (e.g. cell cycle modifications, increased generation of ROS, etc.) as the primary underlying mechanisms for the improved effectiveness of therapeutic radiation by gold nanoparticles.

In this context, a rather dissatisfying situation addresses the need for meaningful studies that might help to reveal the true role of gold nanoparticles in radiation therapy. This chapter evaluates the role of gold nanoparticles on the MCF-7 cell line at the peak absorption coefficient ratio of gold and soft tissue (around 20.0 keV). The primary goal is to establish this photon energy as an anchor point for further systematic investigations into gold nanoparticles and their influence in radiotherapeutic applications. A deeper knowledge of the underlying mechanisms could help to modify the properties of gold nanoparticles or even design novel radiotherapeutic agents in order to improve radiation therapy.

5.1. Glucose-Functionalized Gold Nanoparticles

Mammalian cells are unable to produce free glucose and must uptake the metabolic-relevant molecule via glucose transportation through the cell membrane. It has been proposed that glucose-capped gold nanoparticles can be internalized via the glucose transportation mechanism, and previously generated results indicate that glucose-functionalized gold nanoparticles are partially internalized by MCF-7 cells via GLUT1-mediated transportation (Jing Yang et al. 2007; Zhang et al. 2008; Hu et al. 2015). When compared to their healthy counterparts, rapidly proliferating cancer cells are characterized by increased glycolysis (Baggetto 1992). Once administered into the patient's body, glucose-functionalized gold nanoparticles should be selectively internalized with presumably higher uptake rates associated to energy-craving cancerous cells rather than healthy tissue.

5.1.1. Preparation Route

The Biology, Information Science, and Nanotechnology Applications Research Laboratory ("BINARY") research group, located at the University of Alberta (UofA) Department of Electrical and Computer Engineering, fabricates monodisperse gold nanoparticles of different sizes and coatings. In accordance with the classical method introduced by Turkevich in the early 1950s (Turkevich et al. 1951), gold colloids are synthesized using chloroauric acid ($HAuCl_4$) as a precursor. All chemicals for the synthesis are purchased from Sigma-Aldrich Co., St. Louis, MO, USA. As recently performed, the following protocol fabricates "naked" and highly monodisperse gold nanoparticles with an average diameter of approximately 11 nm, as measured by dynamic light scattering (Kong et al. 2008; Roa et al. 2011).

For the study presented in this dissertation, deionized water was purified by the Milli-Q Biocel system (ZMQ50F01, Millipore, USA). The initial solution was prepared by adding 3.2 mL of 25 mmol/L $HAuCl_4$ to a 125 mL clean Erlenmeyer flask containing 60 mL of deionized water. The solution was moderately stirred while being placed in an ice bath. Adding 2 mL of 30 mmol/L sodium borohydride ($NaBH_4$) initiated the nanoparticle nucleation phase. The solution was stirred for about 5 min. The freshly prepared gold nanoparticles were further functionalized by adding 4 mL of 20 mmol/L 1-thio-β-D-glucose to the gold colloid. The solution was subsequently stirred for 5 min. By covalently binding to the gold nanoparticle surface, the thiol-group connects the sugar molecule to the nanoparticle. After the preparation, remaining reducing agents or glucose molecules were removed from the gold colloids using filters. The total number of gold atoms can be roughly estimated from the amount of applied precursor ($n_{Au} = 4.8 \times 10^{19}$ atom) resulting in a maximum concentration of gold atoms in the final colloidal solution of about $c_{atom} = 7.0 \times 10^{17}$ atom/mL.

Inductively coupled plasma mass spectroscopy (ICP-MS) is a suitable method to verify the total concentration of gold atoms in fabricated colloids. The UofS Department of Geological Science ICP-MS laboratory performs metal analysis with a detection limit below the single part per trillion (ppt) level and an ICP-typical working range larger than nine orders of magnitude (Scheffer et al. 2008). According to the ICP-MS laboratory, the relative measurement error is less than 5% for detection of heavy elements such as gold. As measured by the ICP-MS laboratory, the concentration of gold in the glucose-free colloid was $c_{Au} = 7.3 \times 10^{-5}$ g/mL. The concentration of gold in the functionalized gold colloid was $c_{Au} = 7.8 \times 10^{-5}$ g/mL. These results are in agreement with the fabricated gold concentration of $c_{Au} = 8.6 \times 10^{-5}$ g/mL as previously reported for phospholipid-coated gold nanoparticle solutions (Hao et al. 2012).

According to the mass of a single gold atom ($M_{Au} = 3.27 \times 10^{-22}$ g), the concentration of gold atoms was $c_{atom} = 2.2 \times 10^{17}$ atom/mL for the glucose-free colloid and $c_{atom} = 2.4 \times 10^{17}$ atom/mL for the functionalized gold nanoparticle solution. The concentration of gold atoms at the beginning of the preparation route was about three times larger than the concentration of gold atoms in the final nanoparticle solutions. Several reasons might be responsible for the reduced concentration of gold atoms as determined by ICP-MS: a certain amount of gold atoms were not converted into nanoparticles during the synthesis; instead, gold atoms ended up in the sediment at the bottom of the reaction flask. Nucleation at the surface of the flasks collected a certain amount of gold atoms at the flasks or a certain amount of gold nanoparticles were filter out at the membranes. Nonetheless, the applied preparation route is capable of fabricating reproducible volumes of functionalized colloidal solutions with well-defined characteristics.

5.1.2. Cellular Uptake Procedure

The internalization of gold nanoparticles depends on the physiological context of living cells. Cell cultures can be understood as biological systems consisting of hundreds or thousands of single entities with identical phenotypic characteristics. In contrast to cell suspensions containing free-floating cells, adherent cells grow in single monolayers on suitable substrate surfaces under an artificial environment specified by the culture medium. Adherent cells remain in direct contact with the culture medium which can be aspirated leaving intact cells at the culture vessel bottom. In this way, attached cells can be easily exposed to gold nanoparticles by adding pre-defined volumes of colloidal solution to the culture medium. During the uptake process, the exposed cell cultures are usually incubated under the typical cell type-specific culture conditions. The nanoparticle exposure immediately ends by replacing the gold-enriched medium with fresh culture medium while the cells remain in the culture vessel. The interaction of gold nanoparticles with constituents of the medium can lead to the formation of stable protein corona on the nanoparticle surface (Lynch et al. 2007). It is generally assumed that nanoparticles are homogeneously dispersed within the culture medium. Because sedimentation of nanoparticles in the culture medium would increase the particle concentration at the bottom of the culture vessels, high diffusion and sedimentation rates might lead to increased nanoparticle uptake kinetics and rates (Cho et al. 2011). For the nanoparticle uptake process, the culture conditions (e.g. culture composition, relationship between the culture volume with the size and shape of the culture vessel) are as important as the already investigated intrinsic properties (e.g. particle size, shape, surface charge and composition (Chithrani et al. 2006; Hühn et al. 2013; Lund et al. 2011)) and deserve full attention and careful consideration.

All uptakes procedures mentioned in this dissertation were carried out using either 96-well plates or Falcon 353001 35 mm cell culture dishes. MCF-7 cells were seeded in the wells or dishes and incubated for 24h to allow the cells to properly attach to the bottom surface. Using 96-well plates, the attached MCF-7 cells were maintained in 200 µL culture medium per well. Prior to its use, the gold nanoparticle mixture was pre-heated to 37°C using a water-bath. For the nanoparticle uptake procedure, the current culture medium was replaced by gold colloid added to a reduced volume of culture medium (the total volume of the mixture was 200 µL). Using similar gold nanoparticle samples, the peak uptake concentration in SK-OV-3 cells had been observed after 48h (Geng et al. 2011). However, studies with glucose-capped gold nanoparticles had shown that the uptake steeply increased for DU-145 cells until it reached a maximum after 4h (Roa et al. 2009). Because any occurring sedimentation of nanoparticles in the culture medium during the uptake period is expected to increase as the nanoparticle exposure time increases (Kato et al. 2010), short uptake periods should be accompanied by a negligible amount of probable sedimentation fractions. The

selected time period for the nanoparticle uptake was therefore set to 3h during which the MCF-7 cells were incubated under the cell type-specific culture conditions. After the nanoparticle treatment, the mixture was carefully aspirated from the wells leaving "gold-enriched" cells inside the culture vessel. These cells were immediately washed with 100 µL phosphate-buffered saline (PBS) and finally allowed to proliferate undisturbed in 200 µL of fresh pre-warmed culture medium.
MCF-7 cells maintained in 35 mm cell culture dishes were treated with a pre-warmed mixture of gold nanoparticle solution dissolved in culture medium (the total volume of the mixture is 2 mL). After 3h, the attached cells were washed with 1 mL PBS and finally maintained in 2 mL pre-warmed culture medium. Every control group relied on a sham procedure based on incubating MCF-7 cell cultures in either 200 µL (96-well plate) or 2 mL (35 mm culture dish) culture medium devoid of colloidal solution.

5.1.3. Intracellular Localization and Size Distribution

Transmission electron microscopy (TEM) studies are suitable methods to reveal the intracellular distribution of internalized gold nanoparticles. As observed with high frequency, internalized gold nanoparticles are mainly contained within cytoplasmic vesicles, suggesting that the cellular uptake and trafficking inside the cells occurs predominantly by endocytosis (Liu et al. 2008; Chithrani et al. 2010; Albanese & Chan 2011; Jain et al. 2011). The detection of glucose-capped gold nanoparticles primarily internalized within cytoplasmic vesicles suggests that uptake occurs via an endocytic pathway (Zhang et al. 2008; Roa et al. 2009). However, a plethora of physical and chemical properties tend to influence the uptake mechanism and intracellular fate. For example, spherical gold nanoparticles have also been observed in sub-cellular compartments such as endoplasmic reticulum or the Golgi apparatus of B16F10 cells (Chang et al. 2008). The particle diameter appears to be one of the key factors for the intracellular destination of gold nanoparticles in cells. Gold nanoparticles with an average diameter of just a few nanometers have higher penetration capabilities and possess a much higher tendency to accumulate in intracellular constituents such as the nucleus (Oh et al. 2011; Huang et al. 2012). For the internalization of gold nanoparticles, the surface properties (i.e. coating, surface charge, etc.) are evidently key parameters that influence uptake mechanisms and rates. Overall, each nanoparticle hybrid system is unique and therefore causes unpredictable interactions to occur at the nano-bio interface.
Located at the Cross Cancer Institute, the UofA Department of Oncology Cell Imaging Facility is equipped with a 200kV JOEL 2100 microscope and house a laboratory for the preparation of biological TEM specimen. Even though TEM is a powerful technique for deciphering the cell architecture and for visualizing sub-cellular biological compartments, the preparation of suitable specimens involves highly complex and critical steps (e.g. fixing, contrast enhancing, resin infiltration and plastic embedding, thin sectioning). For this reason, the specimen preparation was closely supervised by Mrs. Priscilla Gao[3] who also assisted the microscope operation and image acquisition. Over the last decades, the following preparation method had been successfully established for the investigation of the intracellular fate of gold nanoparticles within biological cells at the UofA Medical/Dentistry E.M. Unit (Chen 1989).
First, MCF-7 cells were plated on ACLAR® UltRX 2000 Film placed at the bottom of a culture dish. The attached cells were exposed to gold nanoparticles according to the uptake procedure as described above (Section 5.1.2.). After the nanoparticle uptake, the cells were immediately fixed

[3]Mrs. Pricilla Gao, UofA, Department of Oncology, Cross Cancer Institute, Edmonton, Alberta, Canada, 2016 Contact Information: Phone: 1-780-432-8458, E-mail: pgao@ualberat.ca

in 2% (v/v) paraformaldehyde in 0.1 M phosphate buffer to halt any cellular activity without altering the integrity of the intracellular structures. After fixing, any internalized gold nanoparticles and their positions within the hosting compartments were ultimately preserved. The treated cells were rinsed with a buffer solution and post-fixed in 1% osmium tetroxide (OsO_4) in buffer. By embedding heavy elements directly into lipid parts, osmium tetroxide also acts as a contrast enhancer for cellular membranes. The cells were rinsed with the buffer one more time, incubated in freshly prepared 1% carbohydrazide solution, and rinsed three times with distilled water. Again, the cells were incubated in the 1% OsO_4 buffer and subsequently rinsed with distilled water. After that, the fixed cells were dehydrated through a graded series of ethanol solutions with concentrations ranging from 30% to 100%. Dehydration using an organic solvent eliminates the water from the cells and prepares the sample to be embedded in a resin which is not miscible with water. A series of solutions containing 33%, 50%, and 66% of Spurr's (EMS, #14300) in ethanol was applied to embed the specimen. Then, the infiltrated cells were transferred into a beam capsule filled with 100% Spurr`s and polymerized overnight. For the next step, ultrathin sections less than 50 nm thick were cut with an ultramicrotome. All sections were placed onto specimen grids and post-stained with 4% uranyl acetate and 1% lead acetate for increased contrast before finally washed with distilled water. Both acetates interact with the osmium tetroxide and enhance the contrasting effect for a wide range of cellular structures such as ribosomes, lipid membranes, and other compartments of the cellular cytoplasm. Finally, TEM images of the stained specimen were acquired using the JOEL 2100 operated in bright-field mode at 80 kV.

Because any specimen preparation can lead to artefactual products in the object, it is genuinely recommended to study several control groups before analyzing the intracellular distribution of gold nanoparticles. The use of osmium tetroxide, for instance, creates lipid membranes which are highly electron dense. A thorough understanding of the images is essential to clearly identify and distinguish cellular structures such as cell nuclei or mitochondria (Fig. 5.1A). These sub-cellular structures clearly stand out due to the high electron diffraction contrast. A common mistake in the localization of intracellular gold nanoparticles with their high electron density is demonstrated in the second control image (Fig. 5.1B). Contrast-enhanced ribosomes with an average diameter of 20-30 nm – observable as black spots in mitochondria – can be falsely identified as gold nanoparticles. For the detection of intracellular gold nanoparticles with an expected diameter in the scale region, it was of utmost importance to rule out any ambiguity error.

As shown, spherical gold nanoparticles were successfully identified among cellular compartments across all specimens (Fig. 5.1C-H). At different image resolutions, the internalized gold nanoparticles were distinguishable from cellular structures due to their high contrast and their distinctive accumulation pattern. The internalization of nanoparticles was particularly evident within cytoplasmic vesicles. Internalization within cellular components such as nuclei or the cellular cytoplasm could not be confirmed, but small amounts of nanoparticles were found at the cell membrane. A closer look at the TEM images reveals that the glucose-capped gold nanoparticles tended to cluster (Fig. 5.1F-G). This heterogeneous accumulation was observed with high frequency across all investigated specimens. A potential translocation of gold-containing vesicles towards specific cellular sub-structures such as mitochondria or the cell nuclei could not be confirmed in this work.

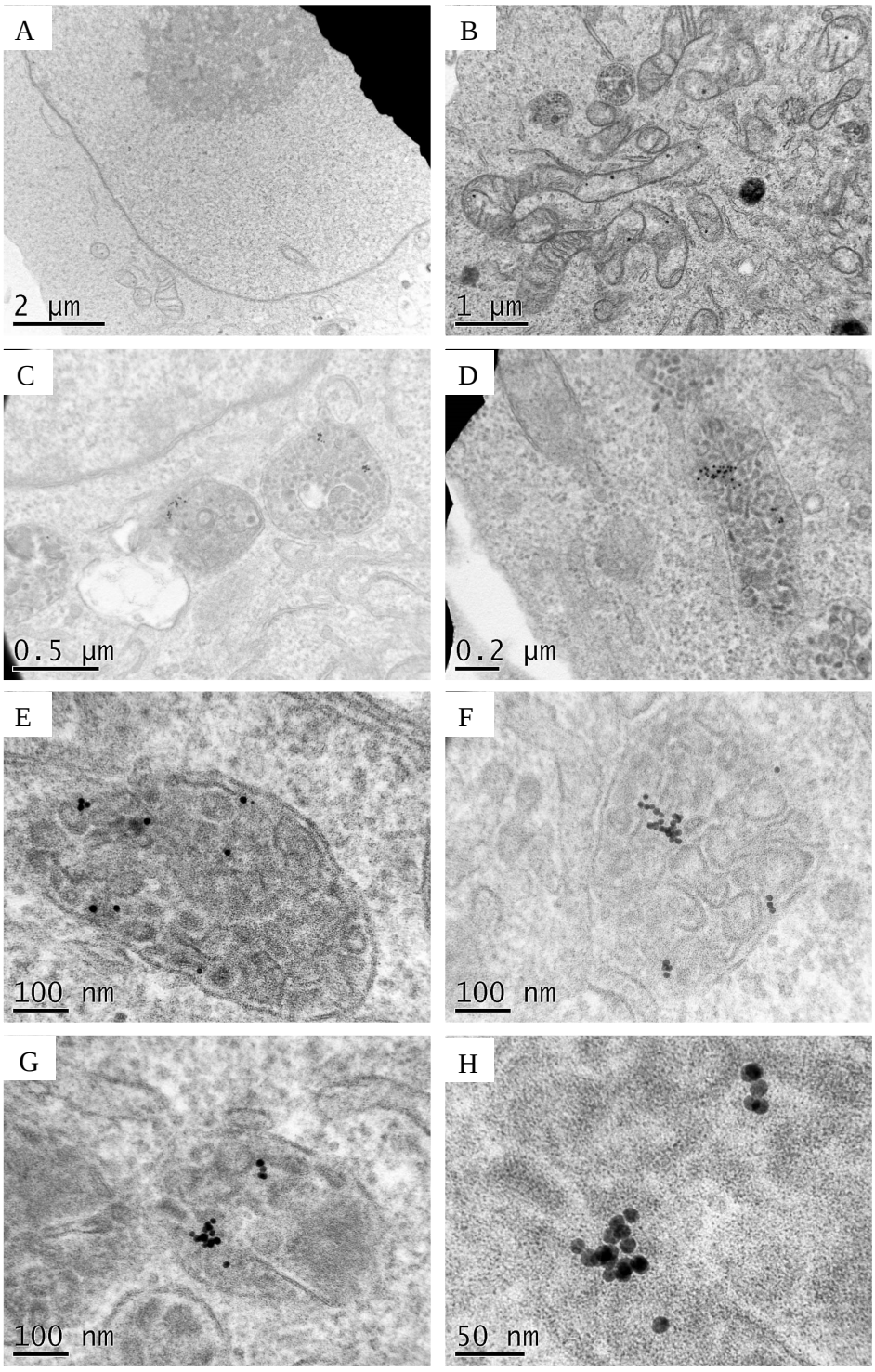

Figure 5.1 Intracellular distribution of gold nanoparticles within MCF-7 cells. (A) The first control image displays part of the cell nucleus including the nucleolus and a few mitochondria. (B) Black spots inside mitochondria visualize ribosomes. (C-H) Gold nanoparticles internalized within cytoplasmic vesicles are visualized at different magnification levels.

Once added to the culture medium, gold nanoparticles might be subject to multiple processes (e.g. formation of a biochemical corona) and may already form clusters before they actually approach the cells (Monopoli et al. 2011). The observation of nanoparticle clusters supports the occurrence of pre-internalization interactions among the particles (Fig. 5.1F-G). However, the observed small distance between the clustered gold nanoparticles indicates the presence of a rather thin nanoparticle surface coating made of low-density components (Fig. 5.1H). This result conflicts with the formation of thick protein coronas or nanoparticle clusters appearing before the actual uptake process. Instead, the organization of gold nanoparticles in clusters within cytoplasmic vesicles might be the result of a post-uptake nanoparticle arrangement within the cells (Fig. 5.1C-D). Subsequent studies might reveal deeper insights into the intracellular distribution of gold nanoparticles.

The preferred accumulation within cytoplasmic vesicles supports the hypothesis that the cellular uptake of gold nanoparticles mainly occurred via an endocytic pathway. The lack of gold nanoparticles within the cytoplasmic solution confirms this assumption. In contrast to the active endocytosis machinery, a passive internalization mechanism based on a diffusion process through the outer cell membrane should result in observations of a certain amount of free-floating gold nanoparticles. It should be mentioned, however, that free-floating nanoparticles within the cytoplasmic solution could be subject to an unwanted removal from the specimen during the preparation process with its numerous fixing and washing steps.

For gold nanoparticles with a diameter of 13 nm, phagocytosis has been identified as the active cellular mechanism for the internalization (Mironava et al. 2010). In this specific endocytosis process, gold nanoparticles that are bound to the surface receptors are engulfed by the cell membrane to form internal vacuoles (i.e. phagosomes). Uptake kinetics via phagocytosis may strongly depend upon the nanoparticle ability to diffuse through the culture medium and to bind to surface receptors. For this reason, the nanoparticle surface biochemistry is expected to play a significant role in the active internalization mechanism. Instead of receptor-mediated endocytosis, nanoparticles floating in the culture medium can also be internalized via pinocytosis. This “cell drinking” mechanism takes extracellular fluids by forming an invagination followed by the formation of small vesicles. When pinocytosis is the primary uptake mechanism, the uptake rate might be raised by increasing the concentration of gold nanoparticles in the direct vicinity of the attached cells. At this point, further experiments are required to identify the primary uptake mechanism, as this TEM examination has not been designed for providing detailed information about the occurring endocytosis machinery.

The acquired TEM images with magnifications of 50,000 and 100,000 (scale bars representing a length of 100 nm and 50 nm) were further analyzed to determine the size distribution of the internalized gold nanoparticles. For this characterization, the particle diameter was measured in units of pixels using the GNU Image Manipulation Program (GIMP) measure tool capable of determining the distance between two pixels in the given TEM image. The particle diameter was determined by measuring the distance between the two furthest pixels associated with a single nanoparticle on the horizontal level (i.e. the angle between the two pixels was zero). After that, the distance was compared to the maximum pixel distance for the imprinted scale bar which acted as reference. The established size distribution of the internalized gold nanoparticles was visualized in the form of a particle diameter frequency histogram (Fig. 5.2).

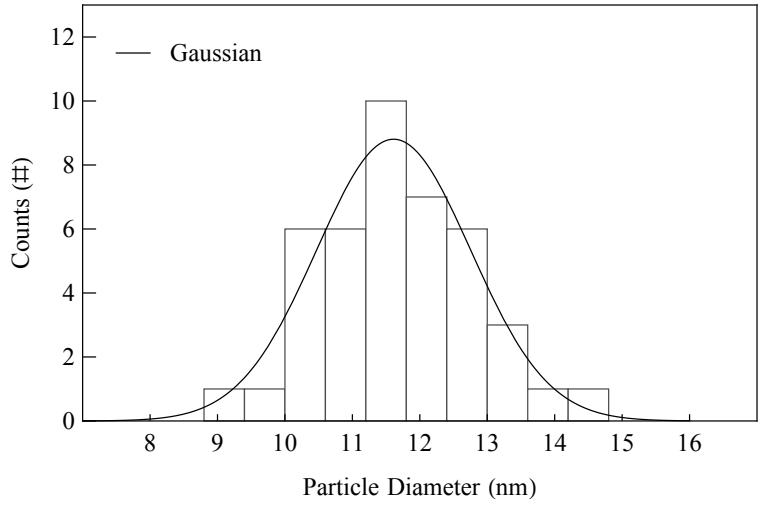

Figure 5.2 Particle diameter histogram of thio-glucose gold nanoparticles internalized within cytoplasmic vesicles. The computed Gaussian distribution (black line) models the shape of the histogram.

The particle diameter distribution was modelled by the following probability density function P(x) of the standard Gaussian distribution using Mathematica's non-linear fitting algorithm:

$$P(x) = \left(\frac{A_d}{\sigma\sqrt{2\pi}}\right) \times \exp\left(-\frac{(x-\mu)^2}{(2\sigma)^2}\right)$$

In this equation, the mean μ (nm) represents the center of the symmetrically shaved curve, σ (nm) is the standard deviation, and A_d (#) is the amplitude coefficient. For a direct comparison with the measured particle size frequency histogram, the computed Gaussian distribution is plotted on top of the histogram (Fig. 5.2). All obtained fit results (Tab. 5.1) are in agreement with the expected nanoparticle diameter in accordance with the applied preparation method capable of forming glucose-capped gold nanoparticles with an average diameter of about 11 nm as determined via TEM and Dynamic Light Scattering (Kong et al. 2008; Roa et al. 2011).

Table 5.1 Fit results for the size distribution of internalized gold nanoparticles.

Parameter	Estimate	Standard Error	P-Value
A_d	25.2	1.7	5×10^{-8}
σ	1.14	0.09	2×10^{-7}
μ	11.61	0.09	5×10^{-17}

To estimate the concentration of functionalized gold nanoparticles in the fabricated gold colloid, it was first necessary to calculate the number of atoms in a gold nanoparticle with a given particle diameter at first. Assuming perfectly spherical gold nanoparticles with a density identical to the bulk density of gold ($\rho_{Au} = 19.3\ gcm^{-3}$), the total mass of the gold nanoparticle M_{np} with a diameter of $\mu = 11.6$ nm was derived by considering the nanoparticle volume V_{np} in accordance with:

$$M_{np} = V_{np} \times \rho_{Au} = 1/6\ \pi\ \mu^3 \times \rho_{Au} = 1.57 \times 10^{-17}\ g$$

After that, the average number of gold atoms per nanoparticle N_{np} was estimated by dividing the mass of a single gold atom ($M_{Au} = 3.27 \times 10^{-22}$ g) from the total mass of a nanoparticle with a diameter of $\mu = 11.6$ nm (Liu et al. 2007):

$$N_{np} = M_{np} / M_{Au} = 4.8 \times 10^{4} \text{ atom/np}$$

The concentration of gold nanoparticles in the synthesized colloid was finally calculated:

$$c_{np} = c_{atom} / N_{np} = 5.0 \times 10^{12} \text{ np/mL}$$

Using Avogadro's constant with $N_A = 6.022 \times 10^{23}$ mol^{-1}, the nanoparticle concentration can be expressed as $c_{np} = 8.3$ nmol/L. This result agrees with the nanoparticle concentrations as presented by the collaborating partners of the BINARY research group. A similar cell exposure to "15 nmol/L" had been recently applied (Roa et al. 2011), while several authors mentioned cell exposures to "15 nmol" of gold nanoparticles (Zhang et al. 2008; Kong et al. 2008; Roa et al. 2009). Also, the most recent ICP-MS results gained by Hao et al. reconfirm the calculated gold nanoparticle concentration as presented in this dissertation (Hao et al. 2012).

5.2. Toxicological Assessment

Over the past decade, the biological character of gold nanoparticles has been evaluated extensively both *in vivo* and *in vitro* (Alkilany & Murphy 2010; Lewinski et al. 2008). Existing literature presents conflicting data which can be partly attributed to the extensive yet unsystematic approaches. Various cell lines had been used and the nanoparticle properties such as size, shape, and surface properties differ unsystematically not only among studies, but sometimes even during single assessments. Because of the chemical inactivity, nanoparticles made of gold are generally expected to exhibit a biologically inert character. Even if stable nanoparticles may create certain levels of stress, it is not precluded that the occurrence of interactions at the nano-bio interface remains undetected and do not trigger observable response mechanisms. In this way, each gold nanoparticle sample has to be tested for its biocompatibility within the scope of the intended experiments.

Mass spectroscopy measurements can determine the total number of gold nanoparticles within a given sample, but this disruptive method lacks the ability to differentiate between nanoparticles that have been successfully internalized and those that have merely attached to the outer cell membrane. Quantifying the average number of internalized gold nanoparticles for a single entity can only produce vague results and, in the worst case, may not even reflect the actual situation within the cells. On the other hand, the volume of a well-characterized gold colloid added to the culture medium provides the required information to reproduce the experimental conditions across multiple assessments. For this reason, the volume of colloidal solution was used as a representative of the concentration of gold nanoparticles applied to the targeted MCF-7 population.

In the following toxicological study, the cellular response of MCF-7 cells to being exposed to functionalized gold nanoparticles was quantified by MTT assessments. Toxicological studies based on MTT conversion are commonly performed in 96-well plates. The first assessment intentionally mimicked these conditions and tested MCF-7 cells seeded in 96-well plate with a concentration of 10^3 cell/well to a total volume of 200 µL. The cells were allowed to attach to the bottom of the well while being incubated. On the next day, the cells were exposed to a

consecutive series of gold concentrations in accordance with the nanoparticle uptake procedure. Despite increasing the volume of gold colloid added to the culture medium, the total volume of the mixture in each well was kept constant (200 µL). Several control groups were treated with identical volumes of PBS instead of gold colloid to exclude that the applied volumes of culture medium within the wells alone influence the cellular viability. After the exposure, the mixtures were aspirated from each well, the cells were carefully washed with 100 µL PBS and finally maintained in 200 µL fresh culture medium. The cellular viability was assessed after three MCF-7 doubling times (87h) during which the cells proliferated undisturbed under the cell line-type specific culture conditions. At the study's end-point, final analysis was conducted in accordance with the manufacturer's standard MTT protocol (see Section 3.2.). The results are shown in Figure 5.3A and Figure 5.3B with each displayed data point representing the mean and standard deviation of five independent measurements.

The second toxicological assessment was a clone of the first assessment with one major exception: instead of 96-well plates, Falcon 353001 cell culture dishes were used as culture vessels. MCF-7 cells with a concentration of 10^4 cell/dish to a total volume of 2 mL were seeded and subsequently incubated. On the next day, the cells were exposed to a series of mixtures consisting of either gold colloid or a buffered thio-glucose solution BTS in culture medium. The culture dishes were incubated for 3h in accordance with the procedure above. Next, the mixture was removed; the remaining cells were washed with 1 mL of PBS and finally maintained in fresh culture medium for 87h. In this assessment, the cellular viability of each cell population was quantified in accordance with the modified MTT protocol (see Section 3.2.1.). The results are shown in Figure 5.3C and 5.3D with each displayed data point represents the mean and standard deviation of four independent measurements.

The results imply that the treatment of MCF-7 cells with gold nanoparticles did not influence the cellular viability (Fig. 5.3A). The viability rates remain unchanged over a wide range of gold nanoparticle concentrations in the culture medium (the maximum ratio of gold colloid to culture medium was 1:4). This observation confirms the biologically inert character of glucose-capped gold nanoparticles for the tested MCF-7 cell line. The integrity of toxicological viability studies is questioned by the assumption that the internalized gold nanoparticles may influence the conversion of MTT salt into formazan crystals. Nonetheless, the relative standard deviation of about 20% was comparable to the error usually achieved in standard MTT procedures. For this reason, the obtained results confirm the assumption that the internalized gold nanoparticle did not interact with the reactant or the reduced products. Figure 5.3.B shows that reduced concentrations of the culture medium did not affect the integrity of the viability assessment based on the reduction of MTT into formazan. Neither did the presence of PBS increase the relative error of the standard method.

Assessing the cellular viability of nanoparticle-treated MCF-7 cells maintained in culture dishes rather than small wells produced very similar results (Fig. 5.3C). The viability rates are almost constant for colloid-media ratios up to 1:5. The plotted data set also visualizes the increased precision of the absorption measurements. The relative standard deviation of four independent measurements is about 10%. An increased concentration of sugar-molecules in the culture medium presumably supports the metabolic activity with potential influence on the cellular conversion of MTT into formazan (Vistica et al. 1991). To verify this statement, culture medium enriched with thio-glucose diluted in a phosphate-buffered solution (BTS) was used in the final experiment. Here, the concentration of glucose in BTS was comparable to the concentration of glucose in the functionalized gold colloid. However, adding high concentrations of thio-glucose to the culture medium did not mediate any cellular functions responsible for the conversion of MTT into formazan crystals (Fig. 5.3D).

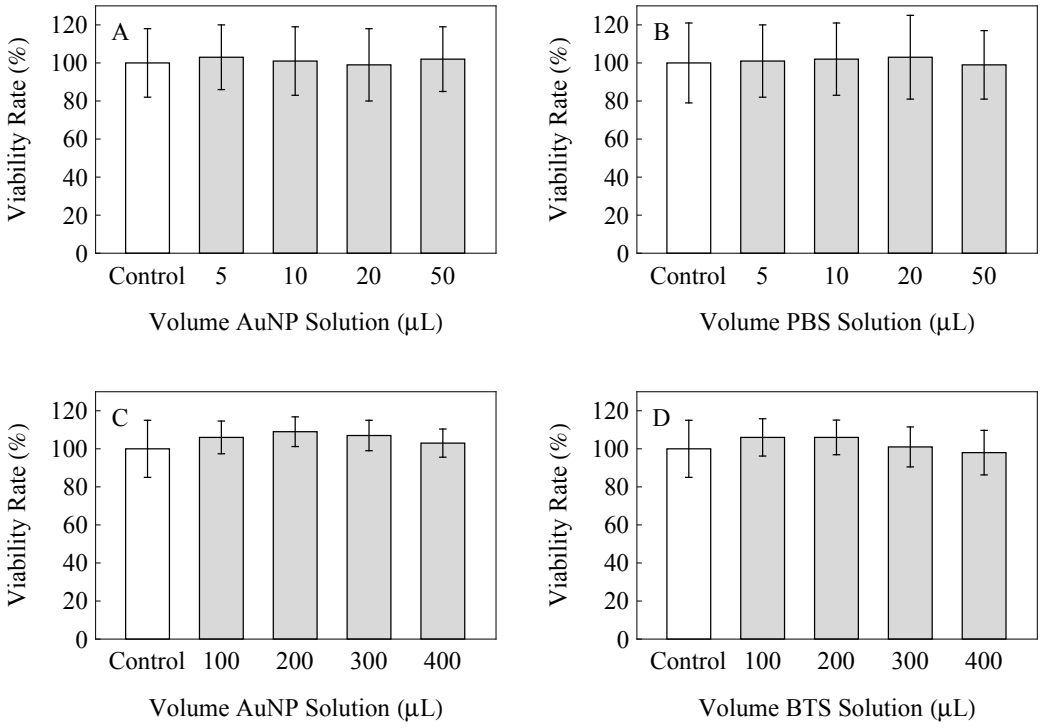

Figure 5.3 Toxicological assessments. Standard assessments: Cellular viability of MCF-7 cells exposed to (A) glucose-caped gold nanoparticles or (B) PBS in medium. Modified assessments: Cellular viability of MCF-7 cells exposed to (C) glucose-capped gold nanoparticles or (D) buffered thio-glucose solution (BTS) in medium.

Reduced cell culture volumes did not affect the integrity of the toxicological assessments based on the conversion of MTT by viable MCF-7 cells. Neither did the presence of increased amounts of glucose in the culture medium stimulate the cellular reduction of MTT. Although the presented toxicological study is not entirely completed yet, the gained information supports the statement that the available functionalized gold colloid was highly biocompatible. Also, internalized glucose-capped gold nanoparticles diluted in the culture medium did not interfere with the cellular reduction of MTT into formazan.

5.3. Nanoparticle-Mediated Cellular Response to Deviating Conditions

Although the toxicological assessment indicates that the internalization of glucose-capped gold nanoparticles did not affect the cells, the presence of gold nanoparticles must be considered as an additional parameter to the number of experimental variables that define the final irradiation experiments. Complex *in vitro* irradiation studies are accompanied by experimental steps which can create stress-related or even disrupting effects on the living tissue. For example, during the sample transportation from the biology laboratory to the irradiation facility, the environmental conditions vary strongly and may induce certain stress[4]. It is of the utmost importance to clearly

[4]The University of Saskatchewan Life Science Building is located at the south end of the campus while the Canadian Light Source is located about 25 walking minutes further north. In Saskatoon, the local temperature can drop below -25°C from November until March.

identify and control all experimental parameters and to eliminate factors that may potentially influence the cellular behavior with distressing consequences on the final outcomes.

The following simulation evaluates the impact of internalized gold nanoparticles during a plain sample transportation. The sample transportation was deliberately executed without the use of proper cell culture equipment which otherwise provides optimal cell type-specific culture conditions. Here, the environmental culture conditions available in the laboratory fume hood (i.e. RT, air) were used as a test atmosphere to observe any cellular mechanisms triggered by the gold nanoparticles in a possibly inadequate experimental procedure. For this test, a first group of MCF-7 samples was prepared (10^4 cell/dish in 35 mm culture dishes) and treated with 200 µL gold nanoparticles in accordance with the nanoparticle uptake procedure described above. The second group of the MCF-7 samples (sham control) was treated with culture medium devoid of the nanoparticle solution.

At this point, the experiment was split into two parts. In the first session, both types of MCF-7 samples (with or without gold nanoparticles) were stored either in the incubator (characterized by environmental conditions of 37°C and 5% CO_2 in humidified air) or in the laboratory fume hood (RT, air) for 2h. In the second session, MCF-7 samples with and without gold nanoparticles were stored either in the incubator or in the fume hood for an extended period of 5h. All samples stored in the fume hood were covered with aluminum foil to protect them from incident light. After the exposure to the deviated environmental conditions, every sample group was then placed in the incubator and allowed to proliferate undisturbed for three MCF-7 doubling times (87h). After the post-exposure incubation phase, the cells were harvested using 500 µL Trypsin and 1.5 mL of culture medium and, after centrifugation and resuspension, homogenously reseeded in five wells of a 96-well plate. The plate was incubated for another 24h to allow cells to attach to the well bottoms. The viability rate of each sample was finally assessed in accordance with the standard MTT protocol. Each experiment was performed in quadruplets.

Figure 5.4 illustrates the cellular viability rates of the MCF-7 samples (with and without gold nanoparticles), which were exposed to the different environmental culture conditions for 2h. The incubated MCF-7 cells treated with gold nanoparticles showed a slightly reduced cellular viability rate of 93% as compared to the particle-free control group. Compared to the toxicological assessment discussed in the section above, this observation indicates that the presence of gold nanoparticles did not influence the cellular behavior during trypsinization, cell centrifugation, or other involved cell transfer steps. In contrast, particle-free MCF-7 cells suffered when exposed to the environmental conditions available in the fume hood as illustrated by the reduced cellular viability rate of 79% compared to the incubated particle-free control group. Although the treated cells were allowed to recover for three doubling times, the exposure of MCF-7 populations to the environmental conditions in the fume hood for 2h must be recognized as a strong cellular stressor with consequences on the cellular viability. The response of MCF-7 cells maintained at a temperature below the cell type-specific 37°C might range from a simple inhibition of cell proliferation (cells “go to sleep”) to severe lethal effects which may be responsible for triggering a programmed cell death. Slight changes in the pH of the culture medium were observed after the exposure to the laboratory conditions. However, the minor shift to a more acidic pH value (pink phenol red has a minor orange color tone) could be neglected when compared to the pH change caused by the production of waste products within one or two MCF-7 doubling times under standard incubator conditions. At this point, the underlying mechanisms responsible for the reduced cellular viability was not further investigated. The gold-enriched MCF-7 cell populations that were subsequently exposed to the unfavorable environmental conditions exhibited an even further reduced cellular viability rate of 68%. Nonetheless, the difference to the viability rate of

the particle-free MCF-7 sample maintained outside the incubator remained statistically non-relevant.

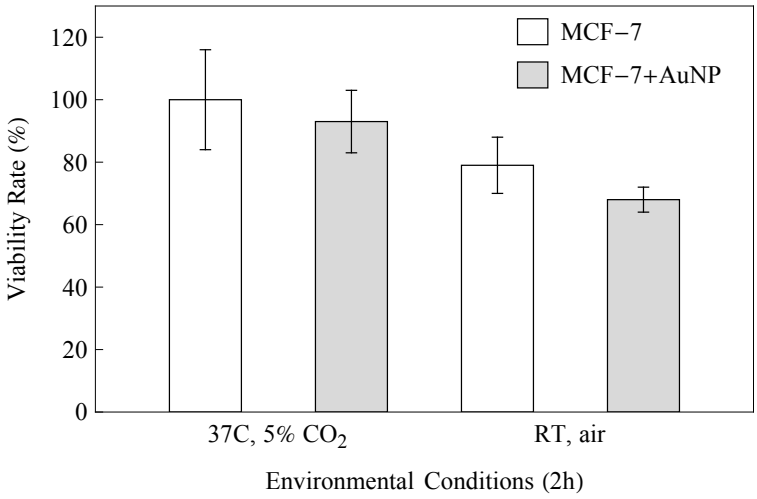

Figure 5.4 Cellular response to deviated environmental culture conditions (2h). The cellular viability of particle-free (white bars) and particle-containing (grey bars) MCF-7 populations are shown as a function of the environmental conditions.

The same trend was observed in the second assessment in which all samples were exposed to the different environmental conditions for 5h (Fig. 5.5). As done before, all samples were allowed to recover from any potential stress factors during the applied post-treatment incubation phase of 87h. As long as the samples were properly maintained under the cell type-specific culture conditions, the internalization of glucose-capped gold nanoparticles did not cause any viability-reducing effects. The measured viability rate of 105% of the particle-containing MCF-7 cells reconfirms the previous observation that the internalized gold nanoparticles did not influence the cellular behavior regardless of whether the adherent cells undergo potentially stress-related steps such as a change of culture vessel. In contrast, the exposure of particle-free MCF-7 to the environmental conditions in the fume hood led to a reduced cellular viability of 73%. After 5h in the fume hood, MCF-7 cell populations treated with gold nanoparticles exhibited a significantly reduced cellular viability of 54%. Compared to the particle-free MCF-7 sample stored under identical yet deviating environmental culture conditions, the viability reduction is statistically relevant this time.

As demonstrated in this study, the exposure of living cells to standard laboratory conditions can generate misleading experimental results which then fail to reflect the true results obtained from the treatment to ionizing radiation alone. The reduction of cellular viability for particle-containing MCF-7 cells maintained under the alternating environmental conditions (68% after 2h and 54% after 5h) must not be neglected. It is highly recommended to verify each sample handling procedure and its appropriateness for *in vitro* irradiation studies. Cell cultures are sensitive to changes of their microenvironment such as fluctuations in temperature, pH value, nutrient, and waste concentrations. As illustrated, slight differences in the environmental culture conditions can become a serious stressor with impact on the cellular viability of the tested population. Now, the occurrence of internalized gold nanoparticles even mediates the cellular response to deviating environmental conditions.

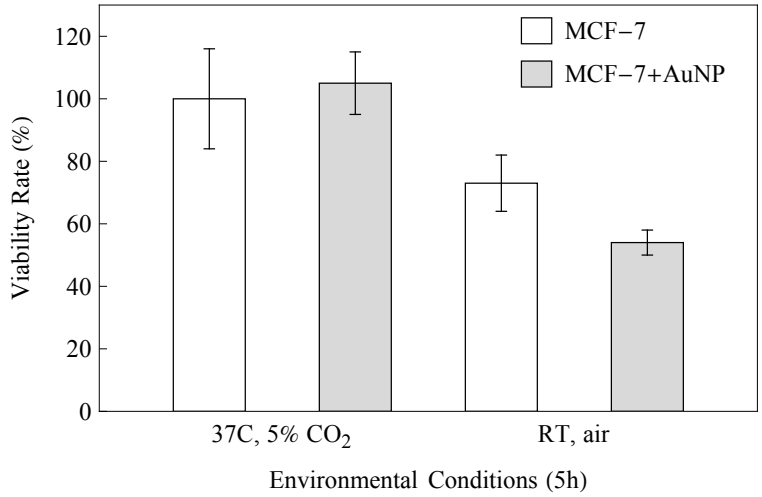

Figure 5.5 Cellular response to deviated environmental culture conditions (5h). The cellular viability of particle-free (white bars) and particle-containing (grey bars) MCF-7 cell populations are shown as a function of the environmental conditions.

The observed effect could be the origin of misleading interpretations and final assumptions about the potential improvement effectiveness induced by the tested enhancement agent. To circumvent these obstacles, meaningful studies must guarantee the absence of any nanoparticle-mediated cellular response to deviations from the optimal cell type-specific culture conditions. The same measures must be taken in advance to avert possible misleading results induced by any clearly identified or undiscovered stress factor. To obtain irradiation results reflective of the radiation-induced biological effects only, it is a necessity to minimize the number of stress factors – known and unknown – which, at the end, is equal to minimizing the number of experimental parameters of the applied irradiation procedure.

5.4. Irradiation Study Using 20.0 keV X-rays

Because the photon attenuation coefficient ratio of gold and soft tissue peaks at around 20 keV, this x-ray energy is accepted an anchor point for every kind of systematic X-ray investigations about the role of gold nanoparticles in radiation therapy. Now, to evaluate the role of gold nanoparticles in radiobiological studies in a scientifically adequate way, a well-documented and verified experimental procedure is a prerequisite.

The following procedure had been applied in the validation study for the irradiation system using 11.9 keV x-rays (Section 4.3.). The novel synchrotron-based irradiation system (Section 4.2.) enabled the treatment of living cell cultures while proliferating undisturbed and uninterrupted under the cell line-specific conditions. The modified MTT protocol was applied to quantify the cellular viability of entire cell populations maintained in dishes also used as irradiation vessels (Section 3.2.1.). A valid transportation strategy had to be designed to provide optimal environmental conditions during the sample transfer to and from the biology laboratory and the sample storage while at the radiation facility site.

5.4.1. Experimental Procedure

The portable incubator G95 by K-Systems generates suitable environmental conditions within the incubator chamber for the transport and storage of human cell lines (K-Systems 2013). In this

study, the incubator was equipped with up to five heating blocks, each of them manufactured to hold two Falcon 353001 culture dishes. The heating blocks were stored in the laboratory incubator. The portable incubator chamber was purged with pre-mixed gases through a quick-snap valve at the rear side. Two gas cylinders, either located at the CSL or connected to the BMIT gas line, provided a pre-mixed gas of 5% CO_2 in air as required for the proper handling of human cell lines. The atmospheric humidity level in the incubator chamber was artificially raised using autoclaved water. The water was preheated to 37°C and poured into two culture dishes. The dishes were placed on top of the heating block stack inside the incubator chamber. During operations, evaporated water created the desired humidity within the chamber. High gas flow rates during the purging procedure can lead to osmotic changes of the culture media causing heavy impairment of cellular viability and irreversible loss of cellular function.

To evaluate the suitable gas output pressure, standard MCF-7 populations with a cell concentration of 10^4 cell/dish in 35 mm culture dishes were used as test samples. For every sample group, four culture dishes were loaded into the warming blocks which were immediately stacked inside the portable incubator chamber. The chamber was closed and purged with the pre-mixed gas using various output pressures. After the purging procedure, the chamber was completely sealed. After one hour the dishes were transferred to the laboratory incubator where the cells proliferated for 87h. The resulting viability rates as a function of the output pressure were finally assessed in accordance with the modified MTT protocol. Once the operational pressure range was determined, samples of MCF-7 cell populations were transported to the radiation facility site. At the BMIT gas line, the incubator chamber was opened for 2 min, closed, and subsequently purged. This procedure was repeated four times every 15 min. The portable incubator was then purged, properly sealed, and returned to the CSL where all MCF-7 samples were incubated for 87h. The cellular viability was quantified in accordance with the modified MTT protocol. The obtained viability results are compared to two control groups. The first control group remained in the laboratory incubator under the cell type-specific culture conditions throughout the experiment. The second group was stored in the fume hood for one hour and acted as a positive control. The obtained results are displayed in Figure 5.6 with each bar representing the mean and standard deviation of four independent measurements.

Purging the incubator chamber with an output pressure of 1 bar (bar 2 in Fig. 5.6) resulted in a viability rate of nearly 98% compared to the incubated control group. However, the relative standard deviation of 7% is larger than the relative standard deviation of 3% as calculated for the control group, though. Deeper investigations revealed that the viability rate for this sample group gradually decreases with the stack position inside the chamber with the highest viability rate measured for the block at the bottom. The smallest viability rate was measured for the cell population placed in the top warming block. This observation led to the assumption that osmotic changes of the culture media gradual decrease the cellular viability; however, a decrease of the temperature in the portable incubator had to be considered as well. Both gas containers (at the CSL and BMIT) are stored at room temperature. It is obvious that purging decreases the temperature in the portable incubator chamber until the temperature sensor re-activates the built-in heating element. Before the conditions inside the chamber return to the defined temperature of 37°C, the cells may experience a certain stress caused by the inappropriate culture environment. Nevertheless, a reduced output pressure to 0.5 bar successfully eliminated the gradual decrease of cellular viability. Even though the viability rate increases to non-relevant 104% (bar 3) when compared to the incubated control group, the relative standard deviation of 3% is almost equal to the standard deviation of the control group. Furthermore, the viability rates are randomly distributed around the overall mean and do not provide any information about the stacking position inside the chamber. Apparently, reducing the output pressure to 0.5 bar allowed the

incubator to maintain the pre-defined temperature level. As a consequence, the regulator output pressure and the gas panel pressure at the BMIT gas line were set to 0.5 bar. The viability rate of MCF-7 cells transferred to and stored at the radiation facility (labelled "BMIT") is identical (bar 4) to the viability rate of the incubated control group. The relative standard deviation is about 5% and the viability rate for each individual cell population is randomly distributed around the mean value (not shown). To visualize the significance of the established transportation procedure, the viability rate of nanoparticle-free MCF-7 cells stored in the fume hood ("Hood") is also plotted. The cells exhibited an essential reduction of viability rate to 89% within one hour when compared to the incubated control group. This result is in agreement with the observations made in the previous section (Section 5.3.) and demonstrates the importance of a sample-oriented transfer strategy. Overall, the developed infrastructure provides optimal environmental culture conditions for the transportation and storage of MCF-7 cell cultures outside the laboratory incubator.

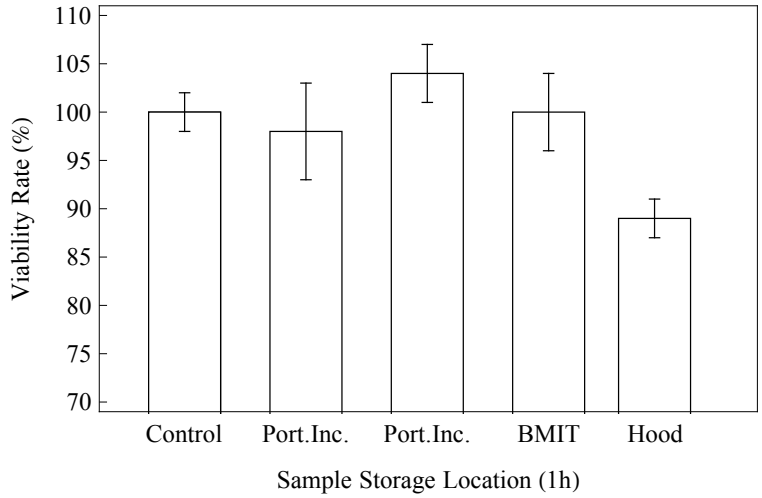

Figure 5.6 Verification of the sample transportation strategy. The cellular viability is shown as a function of the storage location. The influence of the regulator output pressure on the cellular viability is illustrated by bar 2 (labelled: Port.Inc; pressure: 1 bar) and bar 3 (labelled: Port.Inc; pressure: 0.5 bar). Bar 5 represents the positive control group (labelled: Hood).

The established transportation strategy closed the gap in an experimental procedure for the treatment of cell cultures at synchrotron beamlines. The entire MCF-7 sample cycle, beginning from the sample preparation until the final analysis, is illustrated in Figure 5.7. At the beginning, the samples are prepared using 35 mm cell culture dishes under the conditions in the fume hood at the CSL. (Fig. 5.7A). The properly attached MCF-7 cells can subsequently be treated with gold nanoparticles (Section 5.1.3.). Next, the samples can be transferred to the radiation facility under the cell-type specific conditions provided by the sample transportation system (Fig. 5.7C). At the BMIT facility site, the cell cultures remain in the portable incubator chamber until they are placed onto the sample holder of the irradiation system as described in Section 4.2.1. (Fig. 5.7D). The irradiated culture dishes are temporarily stored to the portable incubator and, once the batch of samples is finished, immediately returned to the biology laboratory (Fig. 5.7E). Here, the cells are allowed to proliferate undisturbed for a pre-defined post-treatment phase in the laboratory incubator (Fig. 5.7F). After that, the viable cells in the irradiation vessel convert the yellow MTT salt into purple formazan crystals which are subsequently dissolved in DMSO as described in full

detail in Section 3.2.1 (Fig. 5.7F). At the end, the absorbance of a given sample is spectrophotometrically quantified as described in Section 3.2.1. (Fig. 5.7G).
The proposed irradiation procedure eschews cell transfers between different culture vessels. A single 35 mm culture dish serves as sample container throughout the entire synchrotron-based irradiation experiment. In addition, the biological cells are uninterruptedly maintained under their cell type-specific culture conditions during the entire course of the experiment. The nanoparticle uptake procedure remained the only “disturbance” experienced by the cells – besides the treatment with keV x-rays. The number of experimental parameters is consequently reduced to an absolute minimum. The probability that unidentified and uncontrolled variables influence the cellular behavior should be negligible when compared to previously executed irradiation procedures at synchrotron beamlines. Due to the thoroughly developed experimental protocol, any disturbances in the sample handling procedure can be immediately identified. Deviations from the optimized procedure can be detected at once giving the user the ability to initiate correctional step even during experimental sessions.

The overall high quality of the MCF-7 11.9 keV dose-response curve (see Section 4.3.) already demonstrated the suitability of the protocol which is capable of producing results within less than a week including the sample preparation, nanoparticle uptake, monochromatic irradiation, and final assessment.

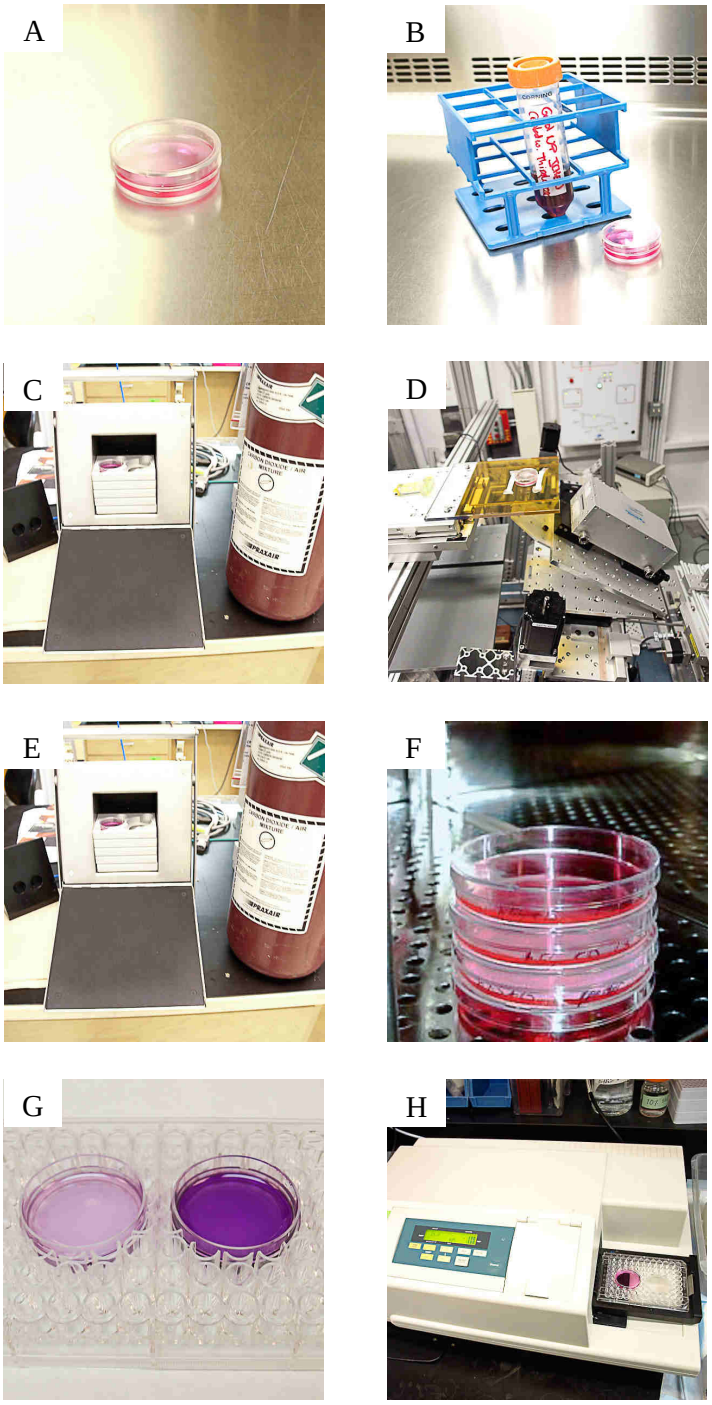

Figure 5.7 Irradiation procedure for MCF-7 cell cultures maintained in 35 mm cell culture dishes. (A) The procedure begins with the sample preparation under the conditions in the fume hood. (B) The attached cells can be treated with gold nanoparticles. (C) The samples are maintained under cell type-specific environmental conditions during the transport and storage at the radiation facility. (D) The culture dishes are scanned horizontally through the monochromatic keV x-ray beam at BMIT-BM and (E) returned to the laboratory. (F) The irradiated cells are stored in the laboratory incubator. (G) The viable cells convert MTT salt into purple formazan crystals subsequently dissolved in DMSO. (H) The procedure ends when the amount of dissolved formazan is spectrophotometrically quantified.

5.4.2. MCF-7 Dose-Response Curve for 20.0 keV X-rays

The following study relied on the verified procedure which was already applied to collect the first 11.9 keV dose-response curve for the breast cancer cell line MCF-7 (see Section 4.3.). The resulting cellular viability as a function of the delivered surface dose is illustrated in Figure 5.8A. In contrast to the 11.9 keV x-ray dose-response curve, each data point represents the mean and standard deviation of either two or three independent measurements due to contamination issues in the laboratory. As a consequence, the relative standard deviation varies strongly among the collected data points. However, the shape of the 20.0 keV dose-response curve is similar to the shape of the 11.9 keV curve. As already observed for the 11.9 keV dose-response curve, the assessed viability decreases as the dose increases in the clinically relevant dose region (≤ 2 Gy). The irradiation of MCF-7 cells with 2 Gy of 20.0 keV x-rays reduces the viability rate to 60%. In contrast to the 11.9 keV x-ray dose-response curve, the effectiveness of 20.0 keV x-rays became less dose-dependent beyond 2 Gy while the measured plateau is significantly elevated. With increasing radiation energy, the ratio of photons interacting with soft tissue via Compton scattering increases and becomes dominant at around 30 keV. The elevated curve plateau for 20.0 keV x-rays compared to 11.9 keV x-rays might be explained the increasing contribution of scattering effects compared to photoelectric absorption. It should also be noted that the transmission of 11.9 keV x-rays in the culture dish bottom (75.2%) is significantly smaller than for 20.0 keV x-rays (86.5%) as discussed in Section 4.2.4. The low plateau at 11.9 keV may indicates that the attenuation of photons in the dish bottom may create certain effects (e.g. emission of low-energy electrons) that add up to the surface dose induced by the therapeutic radiation. Culture dishes with bottoms made of thin layers of Mylar or Kapton would reduce the attenuation of photons drastically. Further studies at various energies may resolve whether the raised plateau can be related to the interaction of therapeutic photons within the living cells or the material placed in front of the targeted tissue.

Again, optical microscopy examinations did not detect any histology modifications for the continuously proliferating cells even after the treatment with 10 Gy. The absence of any stress-indicators at the cell surface supports the hypothesis that a relative large fraction of MCF-7 cells can be characterized as radioresistant. While more than half of the tested MCF-7 population were radioresistant to 20.0 keV x-rays, the same MCF-7 population showed a rather radiosensitive character for the exposure to 11.9 keV X-rays (see Section 4.3.).

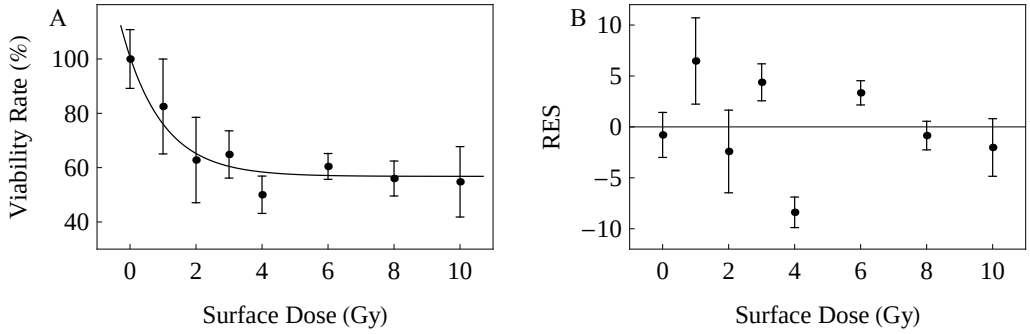

Figure 5.8 Dose-response curve for the MCF-7 cell line exposed to monochromatic 20.0 keV x-rays. (A) Cellular viability as a function of the delivered surface dose rate and best fit curve (black line). (B) Residual plot and standard errors.

In accordance with the fit process described above (see Section 4.3.), the relationship between the viability rate $VR(D_s)$ and the surface dose D_s was sufficiently described by the following normalized first-order exponential decay function:

$$VR(D_s) = \exp(-\alpha_v D_s) + \beta_v$$

Again, α_v (Gy^{-1}) is the rate constant and β_v (%) describes the plateau-like behavior at the upper end of the dose range. Table 5.2 summarized the obtained parameters for the best fit. The mediocre quality of the collected data set is mirrored in the large P-value for the rate constant, but the random distribution of both positive and negative residuals ($RES = VR_{observed} - VR_{expected}$) suggests that the survival data does not differ systematically from the phenomenological model (Fig. 5.8B).

Table 5.2 Fit results for the MCF-7 dose-response curve at 20.0 keV.

Parameter	Estimate	Standard Error	P-Value
α_v	0.82	0.36	6×10^{-2}
β_v	0.57	0.02	2×10^{-6}

Because of the exponentially decaying shape of the MCF-7 dose-response curves for both photon energies, the largest viability changes occur in the low dose region. After a characteristic surface dose of about 4 Gy (11.9 keV) or 2 Gy (20.0 keV), the cellular response to the ionizing radiation was nearly constant with respect to the delivered dose as illustrated by the broad plateau in the corresponding survival curves.

According to the physical rationale, the emission of Auger electrons and the following deposition of additional energy in the vicinity of the internalized gold nanoparticles is the primary mechanism responsible for an enhanced radiotherapeutic effectiveness of keV x-rays. However, the verified exponentially decaying pattern in the dose-response curves implies that the ratio of radiosensitive cells in the irradiated population decreases drastically with increasing dose levels. In the dose region characterized by a plateau-like viability, the majority of cells associated with a certain radiosensitivity have already lost their integrity to proliferate while only those cells which showed a highly radioresistant behavior continued growing after the treatment. Secondary radiation should be less effective in generating damaging effects in the latter group which is characterized by invulnerability to ionizing radiation. On the other hand, an increased local dose and the appearance of additional damaging effects should create a significantly elevated level of stress for cells which tend to respond radically to ionizing radiation. As a consequence, the impact of the gold nanoparticles on the cellular integrity to proliferate after irradiation might depend on the level of applied radiation dose with any nanoparticle-induced effects only being detectable in the low dose region. Based on these implications and the circumstance that fractionated clinically dose levels are usually set below a dose level of 2 Gy, the following gold nanoparticle study focused on the lower dose region around the determined dose threshold for 20.0 keV x-rays.

5.4.3. The Ineffectiveness of Gold Nanoparticles at 1 Gy

In the first irradiation experiment, MCF-7 cells treated with and without gold nanoparticles were exposed to 1 Gy of monochromatic 20.0 keV x-rays. The nanoparticle uptake was performed in accordance with the established protocol (see Section 5.1.2.). In this assessment, a consecutive

series of colloid volumes ranging from 0.2 mL to 1 mL was applied to the prepared MCF-7 cultures. The established irradiation procedure, as described in Section 5.4.1., provided the important cell type-specific culture conditions during the experiment. The results for the first assessment are displayed in Figure 5.9 with each data point representing the mean and standard deviation of four independent measurements. The average relative standard deviation of less than 10% reflects the overall high quality of the collected data set. The small error bars display not only the overall high precision achieved by the modified MTT assay, but also indicate the importance of an experienced sample handling (i.e. preparation, transportation, and assessment) for the production of credible data sets.

In this assessment, particle-free MCF-7 cells exposed to 1 Gy of 20.0 keV x-rays exhibited a decreased viability rate in accordance with the dose-response curve presented above (Section 5.4.2). The cellular viability rate of about 64% (bar 2) was lower than the rate of about 83% as measured for the dose-response curve, but just slightly lower than the 75% as calculated from the fit curve. The large difference between the measured rates could be attributed to the mediocre quality of the dose-response data set. Varying cell cycle stages among different experimental sessions could be another explanation for the observed divergence, too. Depending on the irradiation experiment, the prepared MCF-7 samples had to be incubated until the irradiation system was operational and the synchrotron conditions (e.g. high electron current in the storage ring, sufficient time until the next injection of electrons into the storage ring) enabled the consecutive treatment of an entire batch of samples. For those reasons, the pre-treatment incubation phase ranged from less than one hour to about 8h. The prepared cells could have reached different stages of the cell cycle with may have influenced their susceptibility to 20.0 keV x-rays.

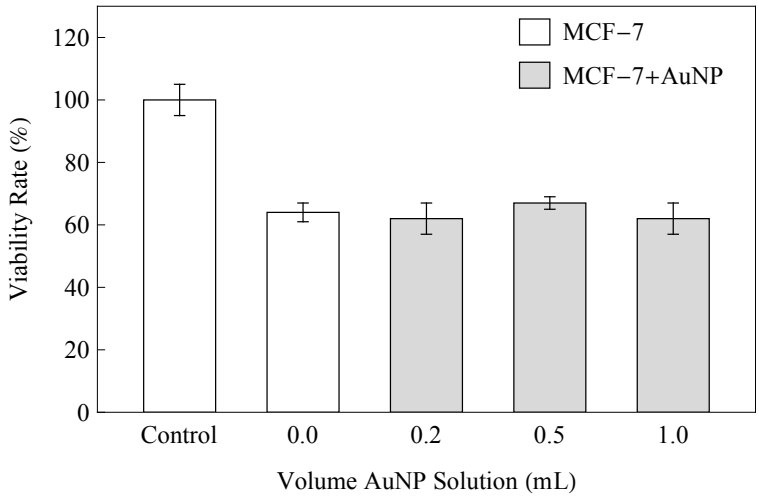

Figure 5.9 Cellular viability of MCF-7 cells treated without (white) and with (grey) gold nanoparticles after the exposure to 1 Gy of 20.0 keV x-rays.

For MCF-7 samples treated with volumes of colloidal gold of 0.2 mL, 0.5 mL, and 1.0 mL, the respective measured viability rates of 62%, 67%, and 62% were homogenously distributed around the viability rate of the irradiated nanoparticle-free MCF-7 sample. The treatment of MCF-7 cells with high concentrations of gold nanoparticles before the irradiation with 1 Gy of 20.0 keV consequently did not lead to a further reduction of cellular viability. Proof must be presented showing that high volumes of colloidal gold in the culture mixture increases the concentrations of

internalized gold nanoparticles within the targeted MCF-7 cells. Further studies might evaluate the relationship between the nanoparticle concentration in the culture medium and the cellular uptake rate. If nanoparticles are preferably internalized via pinocytosis, the uptake rate is proportional to the concentration of gold nanoparticles in the vicinity of the cells. In this case, large volumes of colloidal gold in the culture mixture should increase the nanoparticle concentrations in the cellular vesicles. Although the radiosensitization of MCF-7 cells varied strongly around a surface of a dose of 1 Gy as illustrated by the 20.0 keV dose-response curve, the first radiotherapeutic assessment suggests that even large concentrations of internalized gold nanoparticles did not mediate the radiosensitization of the MCF-7 cell line to 1 Gy of 20.0 keV x-rays.

As a result, the identical viability rates for all MCF-7 samples illustrated the lack of any nanoparticle-mediated influences for 20.0 keV x-rays. Instead, the recorded data set emphasizes the overall credibility of the applied irradiation procedure which was characterized by a minimized number of experimental parameters. In this manner, the obtained results can also be understood as an indicator for the overall suitability of the established procedure.

5.4.4. The Ineffectiveness of Gold Nanoparticles at 2 Gy and 4 Gy

In the final irradiation session, MCF-7 cells treated with gold nanoparticles were exposed to a dose level of either 2 Gy or 4 Gy. All irradiations were performed in accordance with the established irradiation procedure. This time, the post-treatment incubation phase lasted 80h, instead of 87h. The reduced post-treatment proliferation phase was expected to influence the number of self-replicating cells within the irradiated samples. For that reason, any comparisons of the results obtained in both assessments must be handled carefully as they may differ systematically due to the larger post-irradiation proliferation phase. However, direct comparisons of the results obtained in the final assessments are still valid. In this experiment, the control group was divided into a particle-free and a particle-containing sample. Both samples were sham controls, meaning that they were treated identically to the irradiated samples with the exception of the direct exposure to the x-rays. In this manner, every control group was placed onto the sample holder with the x-ray beam completely blocked. The applied “exposure” time of 5 min was equivalent to the actual exposure time for the treatment of MCF-7 cell cultures with 2-4 Gy of 20.0 keV x-rays.

As shown in Figure 5.10, the measured viability rate of 101% for the non-irradiated particle-containing group (bar 2) is almost identical to the viability rate of the non-irradiated particle-free control group (bar 1). The relative standard deviation of slightly less than 10% is in overall agreement with the results obtained for the modified assay protocol. So, the nanoparticle-containing MCF-7 cells did not suffer from any stress factor when compared to the particle-free control group. This result supports the absence of any external stress factors during the transport or storage at the BMIT facility. Exposure of particle-free and particle-containing MCF-7 cells to 2 Gy of monochromatic 20.0 keV x-rays led to reduced viability rates of 74% and 73%. After the treatment with 4 Gy of 20.0 keV x-rays, particle-free and particle-containing MCF-7 cells exhibited viability rates of 69% and 70%. As observed at the 20.0 keV dose-response curve, the treatment of particle-free MCF-7 cells with x-ray doses beyond 2 Gy did not necessarily decrease in cellular viability any further. The relatively high viability rates compared to the values obtained from the dose-response curve (distributed around a value of 60%) can be explained by the reduced post-irradiation incubation phase and the inhibited progression of radiation-induced lethal effects in direct comparison to the undisturbed proliferation of cells in the control groups. Thus,

the obtained viability rates agree well with the results obtained for the 20.0 keV MCF-7 dose-response curve.
Considering both irradiation sessions, the administration of gold nanoparticles did not mediate the response of MCF-7 cells to 20.0 keV x-rays. Even at irradiation dose levels beyond typical fractionated clinical levels, the internalization of gold nanoparticles did not enhance the radiobiological effectiveness of 20.0 keV x-rays *in vitro*. These results are contrary to the observations made in previously reported *in vivo* and *in vitro* studies.

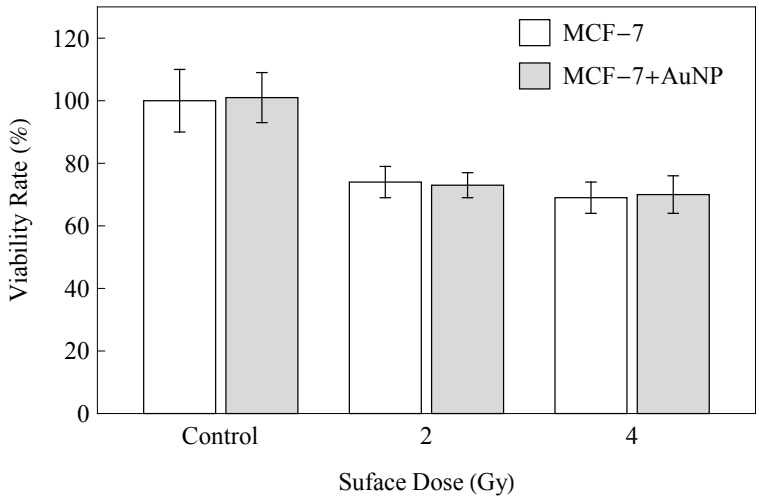

Figure 5.10 Cellular viability of MCF-7 cells treated without (white) and with (grey) gold nanoparticles after the exposure to 2 Gy and 4 Gy of monochromatic 20.0 keV x-rays.

The lack of any observed radiotherapeutic enhancement for photons with energies at the peak attenuation coefficient ratio of gold and soft tissue could be the result of an insufficient uptake or an unfavorable distribution of gold nanoparticles within the targeted cells. The characteristic sub-cellular confinement within cytoplasmic vesicles and the particular absence of gold nanoparticles in the vicinity of cellular components of vital importance explain why the viability rates for the irradiated gold-enriched samples were mostly identical to viability rates of the particle-free counterparts. The average range of Auger electrons in soft tissue is just a few nanometers, resulting in a steep fall-off of absorbed dose from the center of the internalized nanoparticles, especially in the lower kilovoltage photon energy regime (Leung et al. 2011). In this case, any additional damaging effects induced by the emission of Auger electrons should primary occur within cytoplasmic vesicles. The question arises whether low-energy electrons are capable of causing severely damaging effects inside these compartments. Further studies might investigate the nature and the progression of confined damaging effects and why they do not cause severely lethal effects on the targeted cells which, at the end, remain their integrity in terms of metabolic activity and reproduction despite the occurrence of such disturbing events.

Any additional damaging effects induced by gold nanoparticles in radiation therapy might need to progress for a certain amount of time until they cause detectable events on the cellular level. Such events might be observable not days but weeks after the irradiation. In contrast to clonogenic assays, viability assessments such as the standard MTT assay have characteristic end-points usually 24h or 48h after the intended treatment. In this work, all samples were assessed after 87h (or 80h). The selected time frame might be too short for the evaluation of potentially progressing

damaging effects induced by gold nanoparticles. However, the collected dose-response curves illustrate how the established method is capable of quantifying radiation-induced effects by 11.9 keV and 20.0 keV x-rays on the MCF-7 cell line. While an inadequate concentration of gold atoms near cellular compartments of vital importance seemed to be a plausible explanation for the lack of enhanced radiotherapeutic effectiveness, the frequent accumulation of gold nanoparticles within cytoplasmic vesicles already mediates cellular behavior at deviating environmental culture conditions (Section 5.3.). The influence of gold nanoparticles on cellular behavior differs strongly depending upon the experimental conditions in form of the cellular stressor such as deviating environmental culture conditions or ionizing radiation. Reliable gold nanoparticle irradiation studies must discuss the possibility of such a nanoparticle-mediated behavior and its consequences on the final irradiation results.

The obtained “negative” results about the enhanced radiotherapeutic effectiveness of 20.0 keV x-rays by gold nanoparticles conflict with the encouraging results documented in the existing scientific literature. Every nanoparticle hybrid system is unique and may induce different interactions at the nano-bio interface. Numerous gold nanoparticle studies have reported the accumulation of internalized gold nanoparticles within cytoplasmic vesicles as a result of an endocytic cellular uptake mechanism. These studies should have been able to observe the nanoparticle-mediating cellular response to deviating culture conditions. Every gold nanoparticle irradiation study on living cells must consider this effect and is directly confronted with its negative implications unless the biology laboratory is right next to the radiation facility. If this condition is not given, any recorded “positive” outcome might be interpreted as enhanced radiation effectiveness by gold nanoparticles by mistake. Any misinterpreted enhancement can be the result of independent mechanisms affecting the cellular integrity at different levels and times. A sub-additive or even supra-additive combination of multiple effects would complicate the interpretation of an obtained outcome considerably.
Radiobiological *in vitro* studies are highly complex and require scientifically accurate methods in order to evaluate the role of potential enhancement agents such as gold nanoparticles. Experiments based on non-validated procedures generate doubtful results and can be easily discredited. At the end, questions remain whether any observed effects can be related to a radiotherapeutic enhancement. In its place, unknown nanoparticle-cell interactions could be the origin of the detected alterations in the cellular behavior.
To avoid negative repercussions for this research field, the validation and establishment of experimental standards at the upmost level should be the first step before executing extensive studies on living tissue.

6. Conclusion and Outlook

Gold nanoparticles are promising adjuvants for improving the effectiveness of ionizing radiation on living tissue *in vivo* and *in vitro*. To promote this technology into clinical therapeutic applications, a profound understanding about the underlying mechanisms is imperative and can only be achieved through systematic examinations. Synchrotron light facilities – with their unique capacity to generate intense, monochromatic and tunable x-rays – fulfil the experimental qualifications to investigate the role of the nanosized protagonists in radiation therapy. However, research projects at the interface of synchrotron science and cell biology are directly confronted with compromising irradiation conditions and questionable experimental procedures. Extensive work is required to establish systematic studies that meet the needs defined by each discipline involved in this research field. Before this work introduced a new method for the treatment of living cells with monochromatic keV x-rays at synchrotron beamlines, the standard synchrotron-based *in vitro* irradiation experiment had been divided into consecutive experimental parts. For each part, the most common approaches as well as their strengths and weaknesses were evaluated in relation to the experimental conditions for cell cultures. If identified as problematic, the questionable part was either modified or completely redesigned to meet to the upmost standards. The commonly used strategy for the treatment of living cells with keV x-rays at synchrotron beamlines involved a vertical scanning process and several pre- and post-irradiation protocol steps causing questionable consequences on cellular integrity. This work proposed a novel approach for synchrotron-based cell culture irradiation based on the use of a bent silicon wafer in Laue geometry as a monochromatizing device. Implemented at the bending magnet beamline BMIT-BM, the constructed irradiation system enabled horizontal irradiations of standard culture dishes with purely monochromatic x-rays from about 10 keV to 30 keV. In addition, the high x-ray beam intensity allowed to deliver large dose levels of up to 10 Gy within tolerated exposure times. Living cells maintained in common culture vessels were taken from the laboratory incubator, exposed to x-rays through a horizontal rather than vertical scanning process, and returned to the incubator without disturbing and interrupting the cellular growth. In allowing the cells to continuously proliferate under optimal conditions, the genuine approach circumvented the limitations of previous *in vitro* irradiations at synchrotron beamlines. The horizontal set-up even opens up a pathway for promising bright-field, phase-contrast, or even fluorescence imaging applications at synchrotron beamlines. Combined live-cell imaging and rapid functional assessments could create novel opportunities to study radiation-induced events at synchrotron beamlines.

Deviating culture conditions before and after the irradiation process can be the origin for cellular stress factors which then significantly alternate the cellular behavior. A portable incubator provided the required cell type-specific culture conditions for the sample transportation and storage outside the cell laboratory. By generating a culture environment identical to the environment available in the laboratory incubator, the portable device closed an important gap which has been generally neglected in the literature. The universal transportation strategy is not limited to the use of culture dishes but embraces the use of flasks and tubes as culture vessel as well.

To validate the applied experimental procedure and to assess the cellular response to therapeutic radiation, the conversion of the yellow MTT salt into formazan crystals by viable cells was preferred to the time-consuming and work-intensive colony formation. The standard MTT protocol was modified to quantify the amount of formazan directly solubilized in the irradiation vessel. The direct dish read-out produced data sets with an accuracy and precision that can be

hardly achieved with the standard method. The linear relationship between the initial cell number and the measured absorbance over a broad cell number range offered multiple options for key parameters such as the initial number of seeded cells or the duration of the post-irradiation proliferation. The developed measurement process made otherwise necessary cell transfers obsolete and is generally not restricted to the use of culture dishes. As shown, toxicological assessments benefit from an increased level of quality for the collected data sets. The suitability of the modified MTT assay for the quantification of the cellular response to keV x-rays was documented for the breast cancer cell line MCF-7. In contrast to clonogenic assessments, the rapid analytical method generated meaningful irradiation results after only three MCF-7 doubling times. The measured 11.9 keV dose-response curve was phenomenologically well-described by a first order exponential decay indicating that the cellular damage induced by 11.9 keV x-rays is comparable to the lethal effects caused by high linear energy transfer (LET) particles. Despite the appearance of critical experimental inconveniences, the 20.0 keV dose-response curve reconfirmed the general observations made at 11.9 keV.

The established experimental protocol – characterized by horizontal sample irradiations, a sample transportation strategy, and a direct sample read-out process – guaranteed the uninterrupted and undisturbed proliferation of cells under their cell type-specific culture conditions throughout the entire experiment from the sample preparation to the final assessment. Putting all pieces together, the presented irradiation procedure was defined by a minimized set of highly controllable experimental parameters with the ionizing radiation being the only cellular stressor. Synchrotron-based irradiations, conducted under these conditions, maintain the integrity of the living sample to the upmost. By successfully circumventing the limitations at the interface of synchrotron science and cell biology, the irradiation procedure avoids the production of misleading irradiation results and the successive generation false conclusions. Following irradiation studies on living cells are expected to benefit from the established high level of credibility and acceptance.

In the final chapter of this dissertation, the role of gold nanoparticles was evaluated at the peak photon attenuation coefficient ratio of gold and soft tissue (20.0 keV). The prepared gold nanoparticles with an average diameter of about 11.6 nm had been functionalized with thio-glucose. According to mass spectroscopy measurements, the concentration of nanoparticles in the available colloid solution was comparable to the concentrations applied in previously conducted enhancement studies. Transmission electron microscopy provided valuable information about the intracellular distribution of the nanoparticles at the time of the treatment. As successfully illustrated, MCF-7 cells internalize glucose-capped nanoparticles via an endocytic pathway. The nanoparticles were mainly internalized within cytoplasmic vesicles where they frequently assembled in form of clusters. The toxicological study confirmed the predicted nanoparticle biocompatibility for the MCF-7 cell line. Despite their biological inert character, internalized gold nanoparticles were capable of affecting the cellular behavior tremendously. The cellular response to deviating cell culture conditions (i.e. standard laboratory conditions) was significantly mediated. Further research activities may reveal the nature of the observed interaction of gold nanoparticles and the hosting cells. Novel therapeutic technologies may even exploit the nanoparticle-mediating cellular behavior under deviating culture conditions. The nanoparticle-induced effect was successfully eliminated by implementing a sample transportation and storage strategy which allowed the living cells to proliferate under their cell line-specific culture environments. As demonstrated, the employed portable incubator provided the necessary environmental conditions to guarantee the absence of an otherwise systematic error in the recorded irradiation data sets. The final *in vitro* study revealed that the internalized gold nanoparticles did not enhance the radiotherapeutic effectiveness of 20.0 keV x-rays. The observed lack of enhancement at the anchor point for the x-ray energy is in direct conflict with the

encouraging results documented in the scientific literature. These circumstances raise serious questions about the appropriateness of the methods applied in recently conducted studies. The new perspective on the role of gold nanoparticles, including the nanoparticle-mediated cellular response to deviating culture environments, hopefully strengthens awareness of cellular integrity as a key parameter in irradiation studies. Studies that do not sufficiently care for the biological cells have a high chance of suffering from misleading results and false conclusions about the effectives of gold nanoparticles *in vitro*.

Following research activities may focus attention on the intracellular fate of gold nanoparticles and intensify the investigations into the role of gold nanoparticles in radiation therapy as a function of the intracellular distribution of the heavy element. The accumulation of high concentrations of gold in the vicinity of cellular compartments of vital importance such as the cell nuclei or mitochondria should be awarded with high priority. Live-cell imaging or functional assessments based on fluorescence microscopy could support these investigations by identifying events on the cellular or even sub-cellular level.

References

Adam, J.F. et al., 2003. Synchrotron radiation therapy of malignant brain glioma loaded with an iodinated contrast agent: First trial on rats bearing F98 gliomas. *International Journal of Radiation Oncology Biology Physics*, 57(5), pp.1413–1426.

Albanese, A. & Chan, W.C.W., 2011. Effect of gold nanoparticle aggregation on cell uptake and toxicity. *ACS Nano*, 5(7), pp.5478–5489.

Alkilany, A.M. & Murphy, C.J., 2010. Toxicity and cellular uptake of gold nanoparticles: what we have learned so far? *Journal of Nanoparticle Research*, 12(7), pp.2313–2333.

Arvizo, R., Bhattacharya, R. & Mukherjee, P., 2010. Gold nanoparticles: opportunities and challenges in nanomedicine. *Expert Opinion on Drug Delivery*, 7(6), pp.753–763.

Baggetto, L., 1992. Deviant energetic metabolism of glycolytic cancer cells. *Biochimie*, 74(11), pp.959–974.

Bancroft, G.M., 2004. The Canadian Light Source - History and scientific prospects. *Canadian Journal of Chemistry*, 82(6), pp.1028–1042.

Barendsen, G.W.W., 1982. Dose fractionation, dose rate and iso-effect relationships for normal tissue responses. *International Journal of Radiation Oncology Biology Physics*, 8(11), pp.1981–1997.

Berridge, M.V. & Tan, A.S., 1993. Characterization of the Cellular Reduction of 3-(4,5-dimethylthiazol-2-yl)-2,5-diphenyltetrazolium bromide (MTT): Subcellular Localization, Substrate Dependence, and Involvement of Mitochondrial Electron Transport in MTT Reduction. *Archives of Biochemistry and Biophysics*, 303(2), pp.474–482.

Bewer, B., 2010. Dose Calculations. In *Development of an X-ray prism for a combined diffraction enhanced imaging and fluorescence imaging system*. Dissertation. University of Saskatchewan, pp. 22–26.

Biston, M.-C. et al., 2004. Cure of Fisher rats bearing radioresistant F98 glioma treated with cis-platinum and irradiated with monochromatic synchrotron X-rays. *Cancer Research*, 64(7), pp.2317–2323.

Bobyk, L. et al., 2013. Photoactivation of gold nanoparticles for glioma treatment. *Nanomedicine: Nanotechnology, Biology, and Medicine*, 9(7), pp.1089–1097.

Bragg, W.H. & Bragg, W.L., 1913. The Reflection of X-rays by Crystals. *Proceedings of the Royal Society A: Mathematical, Physical and Engineering Sciences*, 88, pp.428–438.

Brenner, D.J., 2008. The linear-quadratic model is an appropriate methodology for determining isoeffective doses at large doses per fraction. *Seminars in Radiation Oncology*, 18(4), pp.234–239.

Brun, E., Duchambon, P., et al., 2009. Gold nanoparticles enhance the X-ray-induced degradation of human centrin 2 protein. *Radiation Physics and Chemistry*, 78(3), pp.177–183.

Brun, E., Sanche, L. & Sicard-Roselli, C., 2009. Parameters governing gold nanoparticle X-ray radiosensitization of DNA in solution. *Colloids and Surfaces B: Biointerfaces*, 72(1), pp.128–134.

Buch, K. et al., 2012. Determination of cell survival after irradiation via clonogenic assay versus

multiple MTT Assay - A comparative study. *Radiation Oncology*, 7(1), p.1.

Butterworth, K.T. et al., 2010. Evaluation of cytotoxicity and radiation enhancement using 1.9 nm gold particles: potential application for cancer therapy. *Nanotechnology*, 21(29), p.295101.

Carmichael, J. et al., 1987. Evaluation of a Tetrazolium-based Semiautomated Colorimetric Assay: Assessment of Radiosensitivity. *Cancer Research*, 47(4), pp.943–946.

Chang, M.-Y. et al., 2008. Increased apoptotic potential and dose-enhancing effect of gold nanoparticles in combination with single-dose clinical electron beams on tumor-bearing mice. *Cancer Science*, 99(7), pp.1479–1484.

Chapman, J.D. et al., 1973. Chemical Radioprotection and Radiosensitization of Mammalian Cells Growing in Vitro. *Radiation Research*, 56(2), p.291.

Chen, M.H., 1989. Fixation, Dehydration, and Embedding. In *Basic Microtechnique for Biological Transmission Electron Microscopy*. University of Alberta, Medicine/Dentistry E.M. Unit, pp. 21–37.

Chithrani, B.D., Ghazani, A.A. & Chan, W.C.W., 2006. Determining the size and shape dependence of gold nanoparticle uptake into mammalian cells. *Nano Letters*, 6(4), pp.662–668.

Chithrani, D.B. et al., 2010. Gold Nanoparticles as Radiation Sensitizers in Cancer Therapy. *Radiation Research*, 173(6), pp.719–728.

Cho, E.C., Zhang, Q. & Xia, Y., 2011. The effect of sedimentation and diffusion on cellular uptake of gold nanoparticles. *Nature Nanotechnology*, 6(6), pp.385–391.

Choi, G.-H. et al., 2012. Photon activated therapy (PAT) using monochromatic Synchrotron x-rays and iron oxide nanoparticles in a mouse tumor model: feasibility study of PAT for the treatment of superficial malignancy. *Radiation Oncology*, 7(1), p.184.

CLS, 2016. What is a Synchrotron? Available at: http://www.lightsource.ca/education/whatis.php [Accessed February 1, 2016].

Corde, S. et al., 2002. Lack of cell death enhancement after irradiation with monochromatic synchrotron X rays at the K-shell edge of platinum incorporated in living SQ20B human cells as cis-diamminedichloroplatinum (II). *Radiation Research*, 158(6), pp.763–770.

Corde, S. et al., 2004. Synchrotron radiation-based experimental determination of the optimal energy for cell radiotoxicity enhancement following photoelectric effect on stable iodinated compounds. *British Journal of Cancer*, 91(3), pp.544–551.

Cutler, J. et al., 2007. The Canadian Light Source: The newest synchrotron in the Americas. *Nuclear Instruments and Methods in Physics Research Section A: Accelerators, Spectrometers, Detectors and Associated Equipment*, 582(1), pp.11–13.

Delaney, G. et al., 2005. The role of radiotherapy in cancer treatment. *Cancer*, 104(6), pp.1129–1137.

Denizot, F. & Lang, R., 1986. Rapid colorimetric assay for cell growth and survival. Modifications to the tetrazolium dye procedure giving improved sensitivity and reliability. *Journal of Immunological Methods*, 89(2), pp.271–277.

Dorsey, J.F. et al., 2013. Gold nanoparticles in radiation research: potential applications for imaging and radiosensitization. *Translational Cancer Research*, 2(4), pp.280–291.

Dugas, J.P. et al., 2011. Dependence of Cell Survival on Iododeoxyuridine Concentration in 35-keV Photon-Activated Auger Electron Radiotherapy. *International Journal of Radiation Oncology Biology Physics*, 79(1), pp.255–261.

Fairbairn, D.W., Olive, P.L. & O'Neill, K.L., 1995. The comet assay: a comprehensive review. *Mutation Research*, 339(1), pp.37–59.

Franken, N. a P. et al., 2006. Clonogenic assay of cells in vitro. *Nature Protocols*, 1(5), pp.2315–2319.

Friedman, D.L. et al., 2010. Subsequent Neoplasms in 5-Year Survivors of Childhood Cancer: The Childhood Cancer Survivor Study. *Journal of the National Cancer Institute*, 102(14), pp.1083–1095.

Geng, F. et al., 2011. Thio-glucose bound gold nanoparticles enhance radio-cytotoxic targeting of ovarian cancer. *Nanotechnology*, 22(28), p.285101.

Gey, G.O., Coffmann, W.D. & Kubicek, M.T., 1952. Tissue culture studies of the proliferative capacity of cervical carcinoma and normal epithelium. *Cancer Research*, 12, pp.264–265.

Gieschen, H.L. et al., 2001. Long-term results of intraoperative electron beam radiotherapy for primary and recurrent retroperitoneal soft tissue sarcoma. *International Journal of Radiation Oncology Biology Physics*, 50(1), pp.127–131.

Gomes, A., Fernandes, E. & Lima, J.L.F.C., 2005. Fluorescence probes used for detection of reactive oxygen species. *Journal of Biochemical and Biophysical Methods*, 65(2–3), pp.45–80.

Gorczyca, W., Gong, J. & Darzynkiewicz, Z., 1993. Detection of DNA strand breaks in individual apoptotic cells by the in situ terminal deoxynucleotidyl transferase and nick translation assays. *Cancer Research*, 53(8), pp.1945–1951.

Görner, W. et al., 2001. BAMline: the first hard X-ray beamline at BESSY II. *Nuclear Instruments and Methods in Physics Research Section A: Accelerators, Spectrometers, Detectors and Associated Equipment*, 467–468, pp.703–706.

Gstraunthaler, G., Seppi, T. & Pfaller, W., 1999. Impact of culture conditions, culture media volumes, and glucose content on metabolic properties of renal epithelial cell cultures. *Cellular Physiology and Biochemistry*, 9(3), pp.150–172.

Guo, N. et al., 2016. Live cell imaging combined with high-energy single-ion microbeam. *Review of Scientific Instruments*, 87(3), p.34301.

Hainfeld, J.F. et al., 2013. Gold nanoparticle imaging and radiotherapy of brain tumors in mice. *Nanomedicine*, 8(10), pp.1601–1609.

Hainfeld, J.F. et al., 2010. Gold nanoparticles enhance the radiation therapy of a murine squamous cell carcinoma. *Physics in Medicine and Biology*, 55(11), pp.3045–3059.

Hainfeld, J.F. et al., 2008. Radiotherapy enhancement with gold nanoparticles. *The Journal of Pharmacy and Pharmacology*, 60(8), pp.977–985.

Hainfeld, J.F., Slatkin, D.N. & Smilowitz, H.M., 2004. The use of gold nanoparticles to enhance radiotherapy in mice. *Physics in Medicine and Biology*, 49(18), pp.N309–N315.

Hao, Y. et al., 2012. Exploring the cell uptake mechanism of phospholipid and polyethylene glycol coated gold nanoparticles. *Nanotechnology*, 23(4), p.45103.

Hébert, E.M. et al., 2010. Preferential tumour accumulation of gold nanoparticles, visualised by magnetic resonance imaging: Radiosensitisation studies in vivo and in vitro. *International Journal of Radiation Biology*, 86(8), pp.692–700.

Howell, R.W., 2008. Auger processes in the 21st century. *International journal of radiation biology*, 84(12), pp.959–975.

Hu, C. et al., 2015. Treating cancer stem cells and cancer metastasis using glucose-coated gold nanoparticles. *International Journal of Nanomedicine*, 10, p.2065.

Huang, K. et al., 2012. Size-dependent localization and penetration of ultrasmall gold nanoparticles in cancer cells, multicellular spheroids, and tumors in vivo. *ACS Nano*, 6(5), pp.4483–4493.

Hubbell, J.H. & Seltzer, S.M., 2009. X-Ray Mass Attenuation Coefficients. *Radiation Physics Division, PML, NIST*. Available at: https://www.nist.gov/pml/x-ray-mass-attenuation-coefficients [Accessed September 21, 2016].

Hühn, D. et al., 2013. Polymer-Coated Nanoparticles Interacting with Proteins and Cells: Focusing on the Sign of the Net Charge. *ACS Nano*, 7(4), pp.3253–3263.

IAEA, 2000. *Calibration of Radiation Protection Monitoring Instruments*, Available at: http://www-pub.iaea.org/MTCD/publications/PDF/P074_scr.pdf.

Iyer, R. & Lehnert, B.E., 2000. Effects of Ionizing Radiation in Targeted and Nontargeted Cells. *Archives of Biochemistry and Biophysics*, 376(1), pp.14–25.

Jabbar, S., Twentyman, P. & Watson, J., 1989. The MTT assay underestimates the growth inhibitory effects of interferons. *British Journal of Cancer*, 60(4), pp.523–528.

Jain, S. et al., 2011. Cell-Specific Radiosensitization by Gold Nanoparticles at Megavoltage Radiation Energies. *International Journal of Radiation Oncology Biology Physics*, 79(2), pp.531–539.

Jain, S., Hirst, D.G. & O'Sullivan, J.M., 2012. Gold nanoparticles as novel agents for cancer therapy. *The British Journal of Radiology*, 85(1010), pp.101–113.

Jeremic, B., Aguerri, A.R. & Filipovic, N., 2013. Radiosensitization by gold nanoparticles. *Clinical and Translational Oncology*, 15(8), pp.593–601.

Jing Yang et al., 2007. The effect of surface properties of gold nanoparticles on cellular uptake. In *2007 IEEE/NIH Life Science Systems and Applications Workshop*. IEEE, pp. 92–95.

De Jong, W.H. et al., 2008. Particle size-dependent organ distribution of gold nanoparticles after intravenous administration. *Biomaterials*, 29(12), pp.1912–1919.

Kaatsch, P. et al., 2015. Krebs gesamt. In *Krebs in Deutschland 2011/2012*. Berlin: Robert Koch Institut & Gesellschaft der epidemiologischen Krebsregister in Deutschland e.V., pp. 20–26.

Karanam, K., Loewer, A. & Lahav, G., 2013. Dynamics of the DNA damage response: insights from live-cell imaging. *Briefings in Functional Genomics*, 12(2), pp.109–117.

Kato, H. et al., 2010. Dispersion characteristics of various metal oxide secondary nanoparticles in culture medium for in vitro toxicology assessment. *Toxicology in Vitro*, 24(3), pp.1009–1018.

Kobayashi, K. et al., 1987. Monochromatic X-ray irradiation system (0.08-0.4 nm) for radiation biology studies using synchrotron radiation at the photon factory. *Journal of Radiation*

Research, 28(4), pp.243–253.

Kong, T. et al., 2008. Enhancement of Radiation Cytotoxicity in Breast-Cancer Cells by Localized Attachment of Gold Nanoparticles. *Small*, 4(9), pp.1537–1543.

Krane, K.S., 1988. Interactions of Radiation with Matter. In *Introductory Nuclear Physics*. New York: John Wiley & Sons, Inc., pp. 193–204.

Krause, M.O., 1979. Atomic radiative and radiationless yields for K and L shells. *Journal of Physical and Chemical Reference Data*, 8(2), pp.307–327.

Krause, M.O. & Oliver, J.H., 1979. Natural widths of atomic K and L levels, Kα X-ray lines and several K L L Auger lines. *Journal of Physical and Chemical Reference Data*, 8(2).

K-Systems, 2013. *Instruction Manual G95*, Birkerod / Denmark. Available at: http://www.k-systems.dk/products/incubators/g95-portable-incubator.html.

Kupcsik, L., 2011. Estimation of Cell Number Based on Metabolic Activity: The MTT Reduction Assay. In *Mammalian Cell Viability*. New York: Humana Press (Springer), pp. 13–19.

Leung, M.K.K. et al., 2011. Irradiation of gold nanoparticles by x-rays: Monte Carlo simulation of dose enhancements and the spatial properties of the secondary electrons production. *Medical Physics*, 38(2), p.624.

Lewinski, N., Colvin, V. & Drezek, R., 2008. Cytotoxicity of Nanoparticles. *Small*, 4(1), pp.26–49.

Lisowska, H. et al., 2013. The dose-response relationship for dicentric chromosomes and γ-H2AX foci in human peripheral blood lymphocytes: Influence of temperature during exposure and intra- and inter-individual variability of donors. *International Journal of Radiation Biology*, 89(3), pp.191–199.

Liu, C.-J. et al., 2008. Enhanced x-ray irradiation-induced cancer cell damage by gold nanoparticles treated by a new synthesis method of polyethylene glycol modification. *Nanotechnology*, 19(29), p.295104.

Liu, C.-J. et al., 2010. Enhancement of cell radiation sensitivity by pegylated gold nanoparticles. *Physics in Medicine and Biology*, 55(4), pp.931–945.

Liu, X. et al., 2007. Extinction coefficient of gold nanoparticles with different sizes and different capping ligands. *Colloids and Surfaces B: Biointerfaces*, 58(1), pp.3–7.

Liu, Y. et al., 2002. Mechanism of Cellular 3-(4,5-Dimethylthiazol-2-yl)-2,5-Diphenyltetrazolium Bromide (MTT) Reduction. *Journal of Neurochemistry*, 69(2), pp.581–593.

Liu, Z. et al., 2014. Real-time brightfield, darkfield, and phase contrast imaging in a light-emitting diode array microscope. *Journal of Biomedical Optics*, 19(10), p.106002.

Lund, T. et al., 2011. The influence of ligand organization on the rate of uptake of gold nanoparticles by colorectal cancer cells. *Biomaterials*, 32(36), pp.9776–9784.

Lynch, I. et al., 2007. The nanoparticle–protein complex as a biological entity; a complex fluids and surface science challenge for the 21st century. *Advances in Colloid and Interface Science*, 134–135, pp.167–174.

Maier, P. et al., 2016. Cellular Pathways in Response to Ionizing Radiation and Their Targetability for Tumor Radiosensitization. *International Journal of Molecular Sciences*, 17(1), p.102.

Manti, L. et al., 1997. Genomic Instability in Chinese Hamster Cells after Exposure to X Rays or Alpha Particles of Different Mean Linear Energy Transfer. *Radiation Research*, 147(1), p.22.

McMahon, S.J. et al., 2011. Energy Dependence of Gold Nanoparticle Radiosensitization in Plasmid DNA. *The Journal of Physical Chemistry C*, 115(41), pp.20160–20167.

McQuaid, H.N. et al., 2016. Imaging and radiation effects of gold nanoparticles in tumour cells. *Scientific Reports*, 6, p.19442.

Meger Wells, C.M. et al., 1991. Synchrotron-produced Ultrasoft X-rays: A Tool for Testing Biophysical Models of Radiation Action. *International Journal of Radiation Biology*, 59(4), pp.985–996.

Mironava, T. et al., 2010. Gold nanoparticles cellular toxicity and recovery: Effect of size, concentration and exposure time. *Nanotoxicology*, 4(1), pp.120–137.

Monopoli, M.P. et al., 2011. Physical−Chemical Aspects of Protein Corona: Relevance to in Vitro and in Vivo Biological Impacts of Nanoparticles. *Journal of the American Chemical Society*, 133(8), pp.2525–2534.

Mosmann, T., 1983. Rapid colorimetric assay for cellular growth and survival: Application to proliferation and cytotoxicity assays. *Journal of Immunological Methods*, 65(1–2), pp.55–63.

Ngwa, W. et al., 2014. Targeted radiotherapy with gold nanoparticles: current status and future perspectives. *Nanomedicine*, 9(7), pp.1063–1082.

Oh, E. et al., 2011. Cellular Uptake and Fate of PEGylated Gold Nanoparticles Is Dependent on Both Cell-Penetration Peptides and Particle Size. *ACS Nano*, 5(8), pp.6434–6448.

Polf, J.C. et al., 2011. Enhanced relative biological effectiveness of proton radiotherapy in tumor cells with internalized gold nanoparticles. *Applied Physics Letters*, 98(19), p.193702.

Pouget, J.-P. & Mather, S.J., 2001. General aspects of the cellular response to low- and high-LET radiation. *European Journal of Nuclear Medicine*, 28(4), pp.541–561.

Price, P. & McMillan, T.J., 1990. Use of the tetrazolium assay in measuring the response of human tumor cells to ionizing radiation. *Cancer Research*, 50(5), pp.1392–1396.

Prise, K.M., 1998. Studies of bystander effects in human fibroblasts using a charged particle microbeam. *International Journal of Radiation Biology*, 74(6), pp.793–798.

Puck, T.T. & Marcus, P.I., 1956. Action of x-rays on mammalian cells. *Journal of Experimental Medicine*, 103(5), pp.653–666.

Rahman, W.N. et al., 2009. Enhancement of radiation effects by gold nanoparticles for superficial radiation therapy. *Nanomedicine: Nanotechnology, Biology and Medicine*, 5(2), pp.136–142.

Rahman, W.N. et al., 2011. Influence of Gold Nanoparticles on Radiation Dose Enhancement and Cellular Migration in Microbeam-Irradiated Cells. *BioNanoScience*, 1(1–2), pp.4–13.

Rahman, W.N. et al., 2014. Optimal energy for cell radiosensitivity enhancement by gold nanoparticles using synchrotron-based monoenergetic photon beams. *International Journal of Nanomedicine*, 9(1), pp.2459–2467.

Ren, B. et al., 1999. A bent Laue–Laue monochromator for a synchrotron-based computed tomography system. *Nuclear Instruments and Methods in Physics Research Section A:*

Accelerators, Spectrometers, Detectors and Associated Equipment, 428(2–3), pp.528–550.

Richtmyer, F.K., Barnes, S.W. & Ramberg, E., 1934. The Widths of the L-Series Lines and of the Energy Levels of Au(79). *Physical Review*, 46(10), pp.843–860.

Riley, P.A., 1994. Free Radicals in Biology: Oxidative Stress and the Effects of Ionizing Radiation. *International Journal of Radiation Biology*, 65(1), pp.27–33.

Roa, W. et al., 2009. Gold nanoparticle sensitize radiotherapy of prostate cancer cells by regulation of the cell cycle. *Nanotechnology*, 20(37), p.375101.

Roa, W. et al., 2012. Pharmacokinetic and toxicological evaluation of multi-functional thiol-6-fluoro-6-deoxy-D-glucose gold nanoparticles in vivo. *Nanotechnology*, 23(37), p.375101.

Roa, W. et al., 2011. Real-time cell-impedance sensing assay as an alternative to clonogenic assay in evaluating cancer radiotherapy. *Analytical and Bioanalytical Chemistry*, 400(7), pp.2003–2011.

Scheffer, A. et al., 2008. ICP-MS as a new tool for the determination of gold nanoparticles in bioanalytical applications. *Analytical and Bioanalytical Chemistry*, 390(1), pp.249–252.

Slater, T.F., Sawyer, B. & Straeuli, U., 1963. Studies on Succinate-Tetrazolium Reductase Systems. III. Points of Coupling of Four Different Tetrazolium Salts. *Biochimica et Biophysica Acta*, 77, pp.383–393.

Slatkin, D.N. et al., 1992. Microbeam radiation therapy. *Medical Physics*, 19(6), pp.1395–1400.

Smilowitz, H.M. et al., 2006. Synergy of gene-mediated immunoprophylaxis and microbeam radiation therapy for advanced intracerebral rat 9L gliosarcomas. *Journal of Neuro-Oncology*, 78(2), pp.135–143.

Suortti, P. et al., 2000. Fixed-exit monochromator for computed tomography with synchrotron radiation at energies 18–90 keV. *Journal of Synchrotron Radiation*, 7(5), pp.340–347.

Suzuki, M. et al., 2012. Live-Cell Imaging Visualizes Frequent Mitotic Skipping During Senescence-Like Growth Arrest in Mammary Carcinoma Cells Exposed to Ionizing Radiation. *International Journal of Radiation Oncology Biology Physics*, 83(2), pp.241–250.

Tanner, R.L., Baily, N.A. & Hilbert, J.W., 1967. High-energy proton depth-dose patterns. *Radiation Research*, 32(4), pp.861–874.

Thompson, A. et al., 2009. Fluorescence Yields for K, L, and Shells. In *X-ray Data Booklet*. Berkeley: Lawrence Berkeley National Laboratory, pp. 28–29.

Turkevich, J., Stevenson, P.C. & Hillier, J., 1951. A study of the nucleation and growth processes in the synthesis of colloidal gold. *Discussions of the Faraday Society*, 11, pp.55–75.

Vistica, D.T. et al., 1991. Tetrazolium-based assays for cellular viability: a critical examination of selected parameters affecting formazan production. *Cancer Research*, 51(10), pp.2515–2520.

Wasserman, T.H. & Twentyman, P., 1988. Use of a colorimetric microtiter (mtt) assay in determining the radiosensitivity of cells from murine solid tumors. *International Journal of Radiation Oncology, Biology, Physics*, 15(3), pp.699–702.

Van De Werf, E., Verstraete, J. & Lievens, Y., 2012. The cost of radiotherapy in a decade of technology evolution. *Radiotherapy and Oncology*, 102(1), pp.148–153.

Willers, H., Dahm-Daphi, J. & Powell, S.N., 2004. Repair of radiation damage to DNA. *British Journal of Cancer*, 90(7), pp.1297–1301.

Wu, L.-J. et al., 1999. Targeted cytoplasmic irradiation with alpha particles induces mutations in mammalian cells. *Proceedings of the National Academy of Sciences*, 96(9), pp.4959–4964.

Wysokinski, T.W. et al., 2007. Beamlines of the biomedical imaging and therapy facility at the Canadian light source — Part 1. *Nuclear Instruments and Methods in Physics Research Section A: Accelerators, Spectrometers, Detectors and Associated Equipment*, 582(1), pp.73–76.

Wysokinski, T.W. et al., 2013. Beamlines of the Biomedical Imaging and Therapy Facility at the Canadian Light Source - Part 2. *Journal of Physics: Conference Series*, 425, p.72013.

Zhang, H., 2009. A Design Study of a Bent Laue Monochromator for Simultaneous K-Edge Subtraction Imaging. In *Imaging Dilute Contrast Materials in Small Animals Using Synchrotron Light*. Dissertation. University of Saskatchewan, pp. 105–133.

Zhang, X. et al., 2008. Enhanced radiation sensitivity in prostate cancer by gold-nanoparticles. *Clinical and Investigative Medicine*, 31(3), pp.E160–E167.

Zhang, X.-D. et al., 2009. Irradiation stability and cytotoxicity of gold nanoparticles for radiotherapy. *International Journal of Nanomedicine*, 4, pp.165–173.

Zheng, Y. et al., 2008. Radiosensitization of DNA by Gold Nanoparticles Irradiated with High-Energy Electrons. *Radiation Research*, 169(1), pp.19–27.

Zheng, Y. & Sanche, L., 2009. Gold Nanoparticles Enhance DNA Damage Induced by Anti-cancer Drugs and Radiation. *Radiation Research*, 172(1), pp.114–119.

Zhu, Y. et al., 2014. Spectral K-edge subtraction imaging. *Physics in Medicine and Biology*, 59(10), pp.2485–2503.

List of Figures

List of Tables

Acknowledgements

First, I want to express my appreciation for my academic advisor Prof. Dr. Hormes for the freedom to pursue and accomplish my interdisciplinary studies. My grateful thanks are extended to Prof. Dr. Linden for his interest in the topic of this dissertation. I want to thank the committee members Prof. Dr. Drees and PD Dr. Fakoussa.

I am deeply indebted to Prof. Dr. Mousseau for his support and his decisive answers to all my questions. All biologically-related parts of this thesis would not have been possible without him and the members of the UofS Cell Signalling Laboratory. I was fortunate to work with Prof. Dr. Chapman and to benefit substantially from his profound expertise in synchrotron-based x-ray imaging techniques. I am obliged to Prof. Dr. Chen who invited me to join the BINARY research group at the UofA. His group synthesized the numerous nanoparticle samples for the research that is described in this dissertation.

I want to thank Dr. Bewer and Mr. Bolibruch. Both contributed substantially to this project as mentioned earlier in this document. I am particularly grateful for the assistance at the CSL given by Mrs. Kuski and Mr. Pennington. Assistance at the BINARY group provided by Dr. Xing and Mrs. Yang was more than just highly appreciated. I am thankful to Dr. Sun and Mrs. Gao (UofA Department of Oncology) for the TEM specimen preparation and the assistance at the microscope.

All CLS members warmly adopted my person and have contributed immensely to my professional time at the University of Saskatchewan. My gratitude goes to the entire BMIT team, in particular, to Dr. Wysokinski and Dr. Belev for their expertise and encouragement. My thanks also go to the members of the UofS Western College of Veterinary Medicine who spent countless sessions with me discussing my research project. I thank Dr. Fan (UofS Department of Geological Science) for the ICP-MS measurements. I was lucky to work together with the recent members of the Synchrotron Light Group at Bonn University: Dr. Kühn, Dr. Bovenkamp, Dr. Fischer, and Mr. Blank.

Every result in this work was accomplished with the help of fellow collaborators and colleagues. I would like to thank all the people who contributed in some way to the work described in this dissertation. I am grateful for all funding sources, in particular the CLS graduate student stipend, which allowed me to pursue my multidisciplinary studies.

Last but not least, I want to express my greatest thanks to my parents Maria and Peter Niestroj and all my family members for their love, genuine care and support throughout my studies. My very special thanks are extended to my love Monique Horsch. I like to say “Thanks” to all my friends.